NOVEL ARTIFICIAL NEURAL NETWORK MODEL FOR PREDICTING FAILURE PRESSURE OF THIN-WALLED PIPES CONTAINING AXIALLY ORIENTED SURFACE CRACKING SUBJECTED TO INTERNAL PRESSURE

by

Xinfang Zhang

A thesis submitted in partial fulfillment of the requirements for the degree of

Doctor of Philosophy

in

Petroleum Engineering

Department of Civil and Environmental Engineering
University of Alberta

© Xinfang Zhang, 2024

ABSTRACT

Axial cracking is a major integrity threat for oil and natural gas transmission pipelines in Canada since its presence can lead to detrimental oil leaks or ruptures, resulting in pipeline incidents, and eventually causing severe damage to the property and the environment. Therefore, periodically monitoring the conditions of transmission pipelines during their service life becomes paramount, and predicting their failures is also essential. Different analytical models are available for predicting the burst capacity of pipelines containing axial external cracks, with the CorLAS^{TM} model being the most widely used. The accuracy of a predictive model can be objectively measured by comparing the test reported failure pressure with the one predicted by the model. However, recent studies have shown that the CorLAS^{TM} model has a slightly conservative mean of test-to-predicted failure pressure ratio and a considerably high coefficient of variation (CoV; standard deviation divided by the mean). The primary aim of this research is to develop a predictive model capable of accurately predicting the failure pressure of pipelines with axial cracks using artificial neural network (ANN) based on datasets generated from the extended finite element method (XFEM) simulations.

The first part of the study examines the accuracy of the latest version of the CorLAS^{TM} model using experimental data collected from the literature. A comprehensive reliability-based assessment of cracked pipelines is performed based on the CorLAS^{TM} model. The effects of several factors such as pipe grade, pipe dimension, crack size, and CorLAS^{TM} model error on the probability of failure (PoFs) are also investigated. The results indicate a significant influence of model error poses on the PoFs.

The second part of the study assesses the effectiveness of the XFEM coupled with the cohesive segment modelling approach implemented in the finite element software ABAQUS for

evaluating cracked pipelines. Within this modelling approach, failure is governed by two damage properties. XFEM models are calibrated and validated based on more than 100 full-scale burst tests data, from which, a correlation between the fracture toughness and XFEM damage properties (i.e., maximum principal strain and fracture energy) is established. In addition, the XFEM predictions are compared with the ones computed by CorLAS^{TM}. The comparison shows that XFEM results in more accurate predictions than CorLAS^{TM}.

The third part of the study presents the development of an ANN model for pipelines with axial cracks subjected to internal pressure only. Given that the performance of an ANN model is highly rely on the accuracy of the input data, XFEM models are validated against more than 100 full-scale burst tests before using their outputs to train the ANN model. Parametric studies are conducted in ABAQUS to examine the effects of pipe and crack sizes on the failure pressure. Based on XFEM parametric analyses, an ANN model is developed using the open-source libraries Scikit-learn and TensorFlow in PYTHON. The trained ANN model is further validated using 25 full-scale burst test data reported from the open literature. Results of ANN predictions are in good agreement with the experimental data with the mean of 1.01 and a low CoV of the test-to-predicted failure pressure ratio at 4.76%, implying that the ANN model is unbiased within the trained range and can serve as a reliable alternative for evaluating cracked pipelines.

PREFACE

This thesis is an original work by Xinfang Zhang. Five papers have been previously published or are ready for potential publication based on this dissertation.

Chapter 2 is derived from a published conference proceeding: Zhang, X., Zheng, Q., Leung, J.Y. and Adeeb, S. Reliability-based Assessment of Cracked pipelines using Monte Carlo Simulation Technique with CorLAS^{TM}. *Proceeding of the ASME 2022 Pressure Vessels & Piping Conference*, July 17-22, 2022, Las Vegas, Nevada, USA, Paper No. PVP2022-80412. I was responsible for conceptualization, methodology, numerical model development, and analysis as well as manuscript composition. Zheng Q. assisted with data collection. Leung, J.Y. and Adeeb, S. were the supervisory authors and were involved with conceptualization and manuscript review.

Chapter 3 is derived from a published conference proceeding: Zhang, X., Lin, M., Kainat, M., Yoosef-Ghodsi, N., Leung, J.Y. and Adeeb, S. Influence of Strain Hardening Model on the CorLAS^{TM} model for Cracked Pipelines. *Proceedings of the ASME 2022 International Pipeline Conference*, September 26-30, 2022, Calgary, Alberta, Canada, Paper No. IPC2022-86856. I was responsible for conceptualization, methodology, numerical model development, and analysis as well as manuscript composition. Leung, J.Y. and Adeeb, S. were the supervisory authors and were responsible for conceptualization and manuscript review. All other authors provided valuable inputs for methodology formulation and result validation.

Chapter 4 is derived from a research article submitted for publication in the Pressure Vessels & Piping Conference proceeding: Zhang, X., Yoosef-Ghodsi, N., Kainat, M., Leung, J.Y. and Adeeb, S. Comparative Study of Crack Shape on the Ductile Fracture Response of Cracked Pipelines. I was responsible for conceptualization, methodology, numerical model development, and analysis as well as manuscript composition. Leung, J.Y. and Adeeb, S. were the supervisory authors and were responsible for conceptualization and manuscript review. All other authors provided valuable inputs for methodology formulation and result validation.

Chapter 5 is derived from a research article submitted for publication in the International Journal of Pressure Vessels and Piping: Zhang, X., Yoosef-Ghodsi, N., Leung, J.Y. and Adeeb, S. Establishing a correlation between Charpy V-notch (CNV) and XFEM damage properties (under review). I was responsible for conceptualization, methodology, numerical model development, and

analysis as well as manuscript composition. Yoosef-Ghodsi, N. assisted with manuscript review. Leung, J.Y. and Adeeb, S. were the supervisory authors and were responsible for conceptualization and manuscript review.

Chapter 6 is derived from a research article submitted for publication in the International Journal of Pressure Vessels and Piping: Zhang, X., Li, Y., Yoosef-Ghodsi, N., Leung, J.Y. and Adeeb, S. An ANN model to predict failure pressure of pipelines containing axial surface cracks (under review). I was responsible for conceptualization, methodology, numerical model development, and analysis as well as manuscript composition. Li, Y. and Yoosef-Ghodsi, N. assisted with manuscript review. Leung, J.Y. and Adeeb, S. were the supervisory authors and were responsible for conceptualization and manuscript review.

Dedicated

To my dearest parents and grandparents

ACKNOWLEDGEMENTS

Like the line from one of my favorite movies: "*Life is like a box of chocolate - you never know what you are gonna get*." If anyone had told me a few years ago that I would come to Canada and pursue a PhD degree, I would not have believed them. Holding this dissertation in my hand, my PhD journey has come to an end. I would like to thank some of the people who helped me face and overcome challenges. This achievement would not have been possible without their invaluable support.

First and foremost, I would like to express my deepest gratitude to my exceptional supervisors, Dr. Samer Adeeb and Dr. Juliana Y. Leung. Their mentorship has played a pivotal role in shaping not only my academic journey but also my personal growth. I am truly grateful for their constant support, patience, and encouragement. It has been a privilege studying under their guidance during my master's and doctoral studies. Over the past six years, they have cared for me not only professionally but also personally. Their dedication to research work and emphasis on critical thinking have genuinely impressed and motivated me. Choosing the right supervisor is vital since most of us only get one chance. I consider myself incredibly fortunate to have met the best supervisors and to have had the opportunity to be a part of their research teams.

I would like to thank my supervisory committee member, Dr. Yong Li, for providing invaluable contributions and guidance throughout my academic journey. I would like to extend my gratitude to other members of my examining committee, Dr. Ashutosh Sutra Dhar and Dr. Huazhou (Andy) Li for their attendance to my final defense and their insightful comments. I would also like to thank my colleagues who provided support and knowledge to help me solve research problems. They also enthusiastically taught me Arabic, Persian, and Spanish.

I would like to extend my appreciation to the China Scholarship Council (CSC) for providing primary funding, and MITACS and C-FER Technologies for additional financial support.

Further thanks go to the industrial partners, Nader Yoosef-Ghodsi and Muntaseer Kainat from Enbridge Liquids Pipelines for their constructive comments in my research.

Last but certainly not least, I would like to express my heartful thanks to my dearest parents and all my friends. Your support and encouragement have been my guiding lights through the most difficult times. Thank you for always being there when I needed someone to talk to.

TABLE OF CONTENTS

LIST OF TABLES

LIST OF FIGURES

LIST OF ABBREVIATIONS

API	American Petroleum Institute
ANN	Artificial neural network
ASTM	American Society for Testing and Materials
ASME	American Society of Mechanical Engineers
BSI	British Standards Institute
CER	Canada Energy Regulator
CEPA	Canadian Energy Pipeline Association
CMOD	Crack mouth opening displacement
CoV	Coefficient of variation
CorLAS	Corrosion Life Assessment Software
CSA	Canadian Society Association
CTOD	Crack tip opening displacement
CT	Compact tension
CVN	Charpy V-notch
CZM	Cohesive zone model
DNN	Deep neural network
DNV	Det Norske Veritas
DOF	Degree of freedom
DIC	Digital image correlation
EAC	Environmental assisted cracking
EAM	Effective area method
EDM	Electric discharge machining
EGRA	Efficient global reliability analysis

EPFM	Elastic plastic fracture mechanics
FAD	Failure assessment diagram
FEA	Finite element analysis
FEM	Finite element method
FORM	First-order reliability method
FPR	Failure pressure ratio
ILI	In-line inspection
LEFM	Linear elastic fracture mechanics
LLS	Leakage limit state
Ln-Sec	Log-Secant
LOC	Loss of containment
LSM	Level set method
LSF	Limit state function
MAE	Mean absolute error
MAOP	Maximum allowable operating pressure
MAP	Maximum annual pressure
MAPE	Mean absolute percentage error
MAXE	Maximum nominal strain
MAXPE	Maximum principal strain
MAXPS	Maximum principal stress
MAXS	Maximum nominal stress
MCS	Monte carlo simulation
ML	Machine learning
MOP	Maximum operating pressure

MRE	Mean relative error
MSE	Mean squared error
MVFOSM	Mean value first-order second moment
NRCan	Natural Resources Canada
PAFFC	Pipe Axial Flaw Failure Criteria
PEEQ	Equivalent plastic strain
PHMSA	Pipeline and Hazardous Materials Safety Administration
PoF	Probability of failure
PRCI	Pipeline Research Council International
PUM	Partition of unity method
PZC	Plastic zone correction
QUADE	Quadratic nominal strain
QUADS	Quadratic nominal stress
RF	Random forest
RSF	Remaining strength factor
RSM	Response surface method
SCC	Stress corrosion cracking
SENT	Single edge notch tension test
SENB	Single-edge notch bending
SF	Safety factor
SLS	Serviceability limit state
SMTS	Specified minimum tensile strength
SMYS	Specified minimum yield strength
SORM	Second-order reliability method

SVM	Support vector machine
TGN	Transportadora de Gas del Norte
TSC	Tensile strain capacity
TSL	Traction-separation law
ULS	Ultimate limit state
UTS	Ultimate tensile strength
VCCT	Virtual crack closure technique
XFEM	Extended finite element method

CHAPTER 1: INTRODUCTION

1.1 Background

Pipelines are considered to be the most favored mode to transport natural gas and crude oil over long distances due to their desirable records, with the fewest reported incidents and fatalities compared to other transportation modes such as rail, train, and truck [1]. As reported by the Canada Energy Regulator (CER), pipelines are crucial infrastructure in Canada, with more than 840,000 km of lines in-service [2]. Depending on their functions, pipelines can be classified as feeder, transmission, gathering, and distribution lines (**Figure 1-1**). However, pipelines do occasionally experience failure caused by the occurrence of mechanical damage (i.e., plain dents, restrained dents, dents with gouges, and punctures), corrosion, and cracking. Among these imperfections, cracks are the most dangerous yet relatively common, accounting for roughly one-fourth of pipeline incidents in Canada [3], making them a primary concern in pipeline integrity assessment.

In general, cracks with various appearances and orientations can occur in the body of the pipe, i.e., axial cracks, circumferential cracks, and inclined cracks, as shown in **Figure 1-2**. The axial cracks align with the longitudinal axis of the pipe, circumferential cracks occur around the circumference of the pipe with the crack plane perpendicular to the longitudinal direction, and inclined cracks orient between the longitudinal and circumferential directions. Circumferential cracking is typically induced by axial and/or bending forces applied to the pipe (due to ground movement), often resulting in leaks, and is more common for small-diameter pipes. Axial cracking can lead to leaks or ruptures and is more common in large-diameter transmission pipelines (> 16 inches) [6]. Compared to circumferential cracks, axial cracks are particularly risky since they are subjected to hoop stress (the biggest stress) caused by internal pressure loading. In January 2018, an in-service rupture was inspected on a 22-inch onshore gas transmission pipeline operated by Transportadora de Gas del Norte (TGN) and further examination revealed that the failure was attributed to two deep axial surface cracks [6]. In addition, axial cracks often occur with other imperfections (e.g., external corrosion and dents) and act as a hybrid defect, making the pipe more vulnerable to failure.

In the scenario of pipelines containing axial cracks, failure pressure is a practical parameter for evaluating the remaining strength of defective pipes and is therefore an essential evaluation parameter in the integrity management program. Failure pressure (or burst pressure) is the maximum load at which a pipeline can withstand before it fails. Over the past 50 years, a number

of analytical methods have been developed for assessment of pipeline with axially-oriented cracks. For instance, Log-Secant model [7], CorLAS^{TM} [8-10], and the failure assessment diagram (FAD) method are common analytical methods for assessing cracks in pipelines. The Log-Secant model, also known as the Battelle model or NG 18 equation, is a fracture mechanics model developed at the Battle Memorial Institute in the 1970s. Crack is evaluated based on the fracture toughness in terms of linear stress intensity factor, K_C, often estimated from Charpy V-notch (CVN) impact energy using an empirical equation. FAD is a graphical approach and is suggested by several codes and standards such as API 579 [12], BS 7910 [13], R6 [14] and SINTAP [15]. Jaske and Beavers [8] developed a software-based model referred to as the CorLAS^{TM} model, it was originally proposed in 1996 but then the same authors published a modified version in a follow-up report [9-10]. Among the aforementioned models, the CorLAS^{TM} model has been shown to provide the most accurate predictions as reported in the literature [16-20]. However, recent studies found that CorLAS^{TM} is associated with a high degree of model error, which could potentially undermine the confidence in reliability-based assessment.

Machine learning (ML) techniques are powerful methods for solving complicated engineering problems [21], involves learning information from samples and analyzing non-linear relationships between the input and output variables to make predictions. Random forest (RF), support vector machine (SVM), and artificial neural network (ANN) are commonly used ML models. The prohibitively high cost of experiment results in limited tests data, hence, numerical simulations are often used to generate a large dataset for training the model. In recent years, ANN has been successfully applied in predicting the failure pressure of pipes with corrosion or dents based on the finite element method (FEM) [22-24]. Oh et al. [22] used the deep learning via ANN approach to predict the failure pressure of API X52, X65, and X80 pipes with a single hemi-spherical dent using results obtained from finite element analysis (FEA)-based parametric analysis. The model-predicted results were compared with FEA and experimental results. A good agreement between the results was observed, demonstrating the accuracy of the predictions using deep neural network (DNN). Liu et al. [23] investigated the applicability of ANN in predicting the failure pressure of API X80 pipes with corrosion based on datasets generated from FEA. Their results showed that the ANN-predicted results were more accurate than those predicted using three corrosion assessment methods, namely ASME B31G, API 579, and DNV-RP-F101. Xu et al. [24] proposed an ANN model to predict the failure pressure of an API X80 subsea pipeline with

interacting corrosion defects using FEM. The experimental data collected from the literature were used to validate their model and the ANN results were compared with codified assessment methods, ASME B31G and DNV-RP-F101. The ANN predictions corresponded well with the test data and showed a better correlation than the assessment methods.

Despite its popularity in modelling corrosion or dents, traditional FEM is not suitable for strong discontinuities such as cracks due to the mesh conformal requirement. Re-meshing is necessary in order to conform to the geometric discontinuities as the crack propagates. To ease the difficulties in solving problems with discontinuities such as crack growth, Belytschko and Black [25] proposed a new numerical technique based on the partition of unity method (PUM) [26], known as the extended finite element method (XFEM). The XFEM approach extends the traditional FEM by adding two enrichment functions (i.e., the displacement jump function and the crack-tip enrichment function), which allowing the discontinuities such as cracks to be arbitrarily aligned within the mesh instead of along the element and alleviating the need of re-meshing since the cracks are modelled mesh-independently. So far, the effectiveness of the XFEM implemented in finite element software, ABAQUS, for assessment of crack propagation in pipelines has been explored by several researchers [27-29]. For instance, the predictions of tensile strain capacity (TSC) of circumferentially-cracked pipes from the full-scale burst tests were performed using the XFEM technique for API X42 grade (Agbo [27]) and API X52 grade (Lin [28]). Okodi et al. [29] used the XFEM to predict failure pressures of axially-cracked X60 pipes based on the data retrieved from 3 full-scale burst tests. All the previous works demonstrate that XFEM results in accurate predictions. However, the application of ANN model in predicting the failure pressure of cracked pipelines based on XFEM has not been investigated yet. The ANN model developed in this work is expected to provide an alternative for assessing the failure pressure of pipelines with axial cracks subjected to internal pressure.

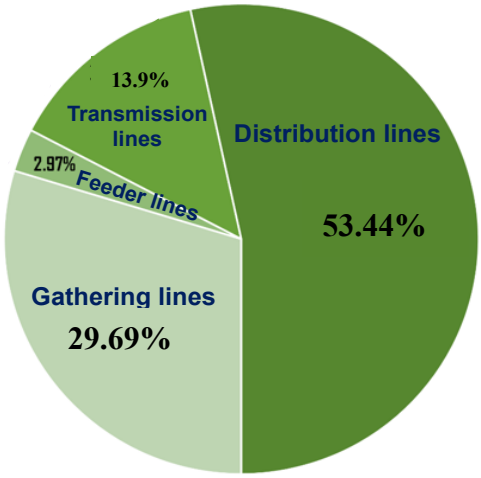

Figure 1-1: Canadian pipeline system [2]

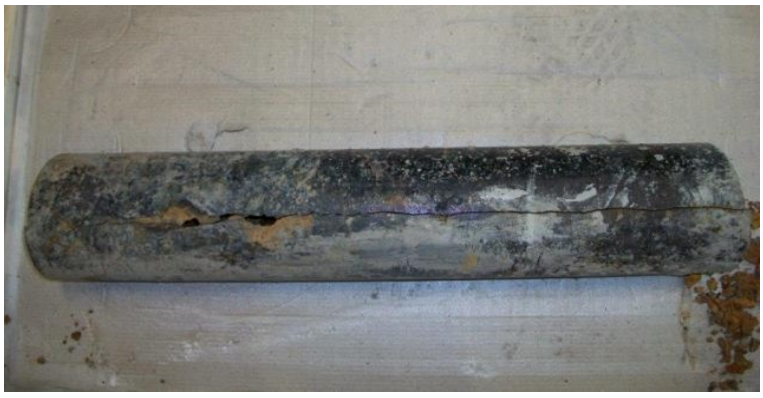

(a) Axial crack

(b) Circumferential crack

(c) Inclined crack

Figure 1-2: Cracks on pipelines [4,5]

1.2 Literature Review

1.2.1 Analytical Methods for Crack Assessment

Log-Secant method (original and modified)

In the late 60s and early 70s, a semi-empirical model was developed by Kiefner and Maxey [7] at the Battelle Memorial Institute, known as Ln-Sec (Log-Secant) model or referred to as Battelle model or NG-18 equation. This method incorporates two failure criteria, namely, flow stress and fracture toughness, to evaluate a crack in pipelines. The failure pressure, P_f, defined by:

$$P_f = \min\left\{\frac{2t\sigma_{flow}}{D}\frac{1-a/t}{1-a/(Mt)}, \frac{4t\sigma_{flow}}{\pi D}\frac{1-a/t}{1-a/(Mt)}\arccos\left[\exp\left(-\frac{K_{mat}^2\pi}{8c\sigma_f^2}\right)\right]\right\}, \quad (1\text{-}1)$$

Where D and t denote the pipe outer diameter and wall thickness, σ_f is the flow stress and calculated based on the yield stress (σ_{flow} = σ_{YS} + 68.95 MPa), a and c denote crack depth and half length, M denotes the bulging or Folias factor, expressed as:

$$M = \begin{cases} \sqrt{1 + 0.6275\left(\frac{2c}{Dt}\right)^2 - 0.00375\left(\frac{2c}{Dt}\right)^4}, \left(\frac{2c}{Dt}\right)^2 \le 50 \\ 3.3 + 0.032\left(\frac{2c}{Dt}\right)^2, \left(\frac{2c}{Dt}\right)^2 > 50 \end{cases} \quad (1\text{-}2)$$

K_{mat} denotes the fracture toughness of the material, if direct measurement of K_{mat} is unavailable, it is recommended to be evaluated based on CVN impact energy using the following empirical equation:

$$K_{mat} = \sqrt{\frac{12CVN}{A_c}E} \quad (1\text{-}3)$$

Where E is the Young's modulus and A_c is the net cross-sectional area of the Charpy specimen.

Since the original model was found to give too conservative results for shallow cracks, Kiefner improved the model with the addition of a correction factor and published the results in the Oil and Gas Journal [30-31] in 2008. In the modified version, the failure stress is given by:

$$\sigma_F = \frac{\sigma_{flow}}{M}\frac{\cos^{-1}(e^{-x})}{\cos^{-1}(e^{-y})} \quad (1\text{-}4)$$

Where $x = \frac{\frac{12CVN}{A_c}E\pi}{8c\sigma_{flow}^2}$ and $y = x\left(1 - \left(\frac{d}{t}\right)^{0.8}\right)^{-1}$.

Failure Assessment Diagram (FAD)

In 1975, Dowling and Townley [11] developed a two-criteria model known as failure assessment diagram (FAD). As shown in **Figure 1-3**, a typical FAD comprises of three key components: the brittle fracture parameter (or toughness ratio, K_r), plastic collapse parameter (or load ratio, L_r) and assessment line. K_r is defined as the ratio of the applied stress intensity factor (K_I) to the material fracture toughness in terms of K (K_{mat}), L_r is defined as the ratio of the applied stress (σ_{ref}) to the yield strength of the material (σ_{YS}), $L_{r,max}$ is the maximum allowable value of load ratio and expressed as $L_{r,max} = \frac{\sigma_{YS}+\sigma_{UTS}}{2\sigma_{YS}}$.

If the assessment point lies underneath the grey curve, the crack is stable, otherwise, a failure is predicted to occur. The failure pressure is the pressure that causes the assessment point (L_r, K_r) falling on the assessment line, in other words, an iterative procedure is necessary for carrying out two independent calculations that the failure pressure based on L_r must be equal to the one corresponding to K_r. This method has three different assessment levels with Level 1 being the simplest form, providing conservative results based on limited information and Level 3 being the most accurate which requires detailed information.

In API 579 Level 2 [12], to evaluate the failure stress level for an axial part-through wall crack with given length (L) and depth (a), the Folias factor (M) is calculated using Eq. (1-2). Then, the reference stress (σ_{ref}) is computed using Maxey's surface flaw stress concentration factor, M_p, as expressed in Eq. (1-5).

$$M_p = \left[\frac{1-\left(\frac{A}{A_o}\right)\left(\frac{1}{M}\right)}{1-\left(\frac{A}{A_o}\right)}\right] \tag{1-5}$$

For a semi-elliptical crack, Eq. (1-5) can be rewritten as:

$$M_p = \left[\frac{1-\left(\frac{\pi a}{4t}\right)\left(\frac{1}{M}\right)}{1-\left(\frac{\pi a}{4t}\right)}\right] \tag{1-6}$$

The influence coefficient (G_0) and the crack shape factor Q, which relate the stress intensity factor (K_I) to the hoop stress at failure, can be calculated using Eqs. (1-7) and (1-8).

$$G_0 = A_o + A_1\beta + A_2\beta^2 + A_3\beta^3 + A_4\beta^4 + A_5\beta^5 + A_6\beta^6 \tag{1-7}$$

$$Q = 1.0 + 1.464\left(\frac{2d}{L}\right)^{1.65} \qquad \text{for } \frac{a}{c} \leq 1 \tag{1-8}$$

Herein, β is equal to $\frac{2\emptyset}{\pi}$ and is taken as 1 when the angular rotation $\emptyset$ is equal to $\frac{\pi}{2}$, six A values can be found in Table C.11 of the Appendix C of the API 579 standard [12] with the premise of the inside radius divided by wall thickness (R_i/t), the raio of half crack length to crack depth (c/a), and the crack depth-to-wall thickness ratio, a/t.

σ_m^c is the hoop stress and expressed as:

$$\sigma_m^c = \frac{\sigma_{ref}}{M_p} \tag{1-9}$$

$$\sigma_m^c = \frac{K_I}{G_0\sqrt{\frac{\pi a}{Q}}} \tag{1-10}$$

Where σ_{ref} and K_I are determined based on L_r and K_r, as shown in Eqs. (1-10) and (1-11).

$$\sigma_{ref} = L_r\sigma_{YS} \tag{1-10}$$

$$K_I = K_r K_{mat} \tag{1-11}$$

Finally, the failure pressure, P_f, is computed for both L_r and K_r.

$$P_f = \frac{\sigma_m^c}{(\frac{R_i}{t}+0.6t)} \tag{1-12}$$

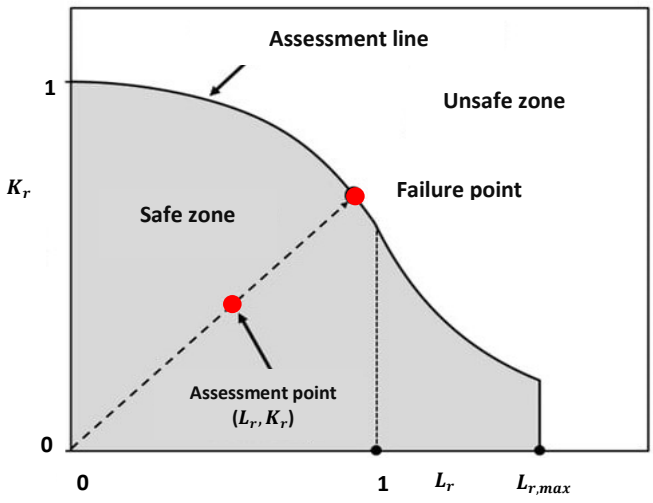

Figure 1-3: Illustration of FAD, adapted from [32]

Corrosion Life Assessment Software (CorLAS^{TM})

In 1996, Jaske and Beaver [8] proposed a J-based fracture mechanics model to evaluate the cracked pipes, known as CorLAS^{TM}. Similar to the Log-Secant model, CorLAS^{TM} also considers two independent failure criteria (i.e., flow stress and fracture toughness criteria). The failure pressure is given by:

$$P_f = \min\{\sigma_{flow}, \sigma_t\} \frac{2t}{D} \left(\frac{1-\frac{\pi a}{4t}}{1-\frac{\pi a}{4tM}} \right) \tag{1-5}$$

Where the flow stress σ_{flow} is equal to the average of yield strength (σ_{YS}) and ultimate tensile strength (σ_{UTS}) and σ_t is the local stress determined by the fracture toughness criterion. The value of σ_t is determined by solving $J = J_C$. If direct measurement of J_C is not available, it is suggested to be evaluated using the following empirical equation:

$$J = \frac{12\ CVN}{A_c} \tag{1-6}$$

Where A_c is the net cross-sectional area of full-sized Charpy specimens.

Since detailed crack profile is often not available in practice, 'equivalent area' approach is used by assuming a semi-elliptical crack profile with an equivalent length and depth. If a rectangular-shaped crack has a length of L_R, its equivalent semi-elliptical crack length would be $L_S = \frac{4L_R}{\pi}$. Detailed formulations of CorLAS^{TM} can be found in **Chapter 2**.

1.2.2 Numerical Methods for Crack Assessment

1.2.2.1 Finite Element Method

The finite element method (FEM) is a well-known numerical technique for finding approximate solutions to partial differential equations, implemented in finite element packages such as ABAQUS [33] and ANSYS [34]. However, it is considered as a computationally expensive and cumbersome approach for simulating crack propagation. Specifically, considerable mesh refinement is required especially at the vicinity of the crack tip to adequately simulate the singular asymptotic fields. In ABAQUS, a FEM crack is a seam crack which is modelled as a face partition embedded into the body part using contour integral method, as shown in **Figure 1-4**. In addition, crack front, crack tip, and crack growth path need to be defined a priori.

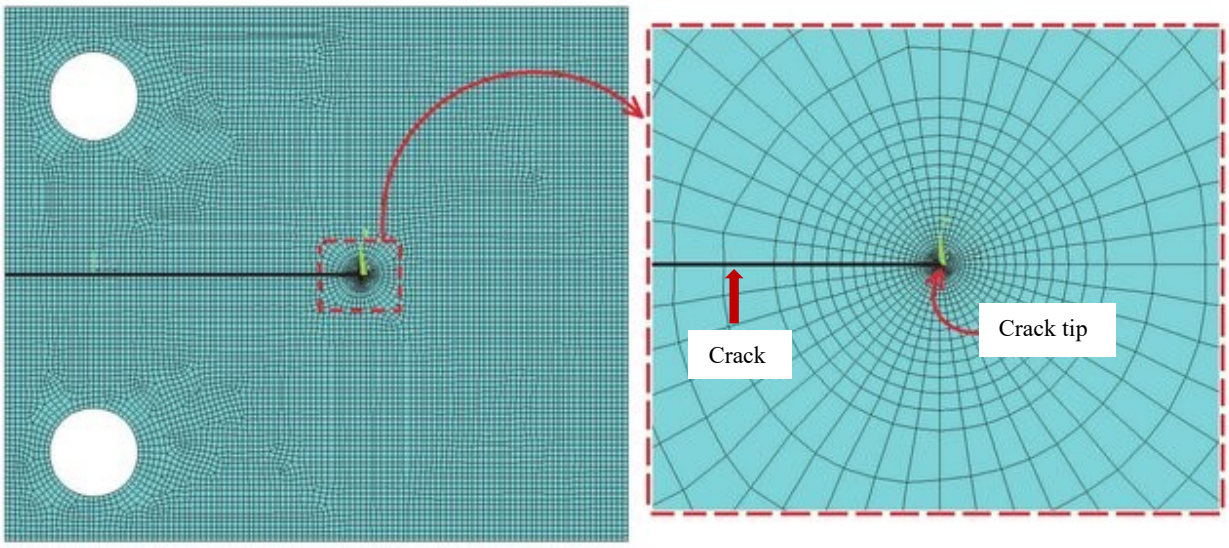

Figure 1-4: Mesh pattern used for modelling cracked specimen, adapted from [35]

1.2.2.2 Extended Finite Element Method

Based on the partition of unity method (PUM) [26], Belytschko and Black [25] proposed a numerical approach known as the extended finite element method (XFEM) that extends the traditional FEM. Special enrichment functions in conjunction with additional nodal degrees of freedom (DOF) are introduced to ensure the presence of discontinuities, by permitting the crack to be not aligned with the finite element mesh, so the crack is geometrically independent of the mesh [36]. The XFEM displacement approximation (u) is expressed as:

$$u = \sum_{I=1}^{N} N_I(x)[u_I + H(x)a_I + \sum_{\alpha=1}^{4} F_\alpha(x)b_I^\alpha] \quad (1\text{-}7)$$

Where $\sum_{I=1}^{N} N_I(x)\, u_I$ is the standard finite element approximation, a_I denotes the nodal enriched DOF vector over the crack interior, $H(x)$ is the Heaviside enrichment function that applies to the nodes whose shape functions are separated by the interior of crack, b_I^α denotes the nodal enriched DOF vector at the crack tip and $F_\alpha(x)$ is the asymptotic crack-tip enrichment function that applicable for the nodes corresponding to the elements cut by the crack tip.

However, the crack-tip function is only considered for modelling stationary cracks, as it is cumbersome to constantly keep track of the crack path in order to accurately capture the crack-tip

singularity [36]. Therefore, for moving crack, the crack has to propagate across an entire element at a time to avoid the need to model the stress singularity.

Unlike FEM, crack front or crack extension direction does not need to be explicitly defined for the contour integral (e.g., K and J-integral) evaluation in XFEM. Level set method (LSM) is used to locate the crack through the use of two functions with one (Φ) represents the crack face and one (Ψ) represents the crack front. It should be noted that the contour integral evaluation in XFEM is only supported for a stationary crack. For crack modelling using XFEM, three outputs variables are important and need to be requested, namely, PHILSM, PSILSM, and STATUSXFEM [36]. PHILSM and PSILSM are the signed distance function used to represent and virtualize the crack. STATUSXFEM indicates the status of the enriched element, a value of 1 means that the element is fully cracked.

In ABAQUS, two distinct approaches are available to model crack initiation and propagation using XFEM which are discussed below.

- **XFEM-Based cohesive segment approach**

XFEM can be used in conjunction with the cohesive zone model (CZM), which is known as the XFEM-based cohesive segment approach. This method is based on the traction-separation cohesive behavior which requires the definition of the fracture criterion, i.e., damage initiation and propagation. The most notable advantage of this approach compared to other available approaches in ABAQUS (i.e., the ones based on cohesive elements or surface-based cohesive behavior) is that cracks are no longer tied to the boundary meshes [36].

Currently, ABAQUS offers three stress-based and three strain-based built-in criteria: The maximum principal stress criterion (MAXPS), the maximum principal strain criterion (MAXPE), the maximum nominal stress criterion (MAXS), the maximum nominal strain criterion (MAXE), the quadratic nominal stress criterion (QUADS), and the quadratic nominal strain criterion (QUADE). Damage is assumed to initiate once the stress or strain reaches the specified value. Detailed information of this approach is covered in the subsequent chapters. Besides six built-in damage initiation criteria, a user-defined damage initiation criterion can be specified in user subroutine UDMGINI, which has been discussed by Lin [38] who developed a variable damage

initiation criterion using the user subroutine based on the modified Mohr-Coulomb fracture criterion.

- **XFEM-based linear elastic fracture mechanics (LEFM) approach**

Unlike the cohesive segment zone (CZM) model within the XFEM framework, this alternative XFEM-based approach is only recommended to model brittle fracture as it is based on the principal of LEFM [36]. In this approach, XFEM modelling technique is used in conjunction with the virtual crack closure technique (VCCT). Damage initiation criterion is the same as in the CZM approach and defined via the material property. Damage evolution is controlled by the strain energy release rate which is calculated using VCCT and needs to be specified as part of the contact interaction property. Crack starts to propagate when the dissipated strain energy rate reaches the critical energy release rate, which can be specified using one of the three available mixed-mode models in ABAQUS: Benzeggagh-Kenane (BK) law, the power law, and the Reeder law [36].

1.3 Problem Statement

Since the 1970s, a number of fracture mechanics models have been developed to assess the pipelines with axially-oriented cracks. The performance of a burst capacity model can be evaluated by comparing the experimental data to the prediction results. This study focuses on the CorLAS^{TM} model because it is widely used by the pipeline industry [37]. However, there is a lack of an appropriate model error associated with the CorLAS^{TM} model and information about incorporating the model error into the reliability analysis. To date, only two published sources of model error associated with the CorLAS^{TM} model are available [19-20]. Yan et al. [19] collected 103 full-scale burst test data from a wide variety of literature to study the model error distribution of CorLAS^{TM} (Version 1), the reported test-to-predicted failure pressure ratio followed a normal distribution with a mean of 0.96 and CoV of 22.8%. While the corresponding mean and CoV of test-to-prediction ratio associated with CorLAS^{TM} (Version 2) were 1.11 and 14%, respectively, as reported by Yan et al. [20]. The data were based on 12 in-service and 63 hydrostatic testing ruptures gathered from the transmission pipeline systems operated by TransCanada. Apparently, a discrepancy existed between the corresponding model errors associated with these two publications. Additionally, the reliability analysis needs to consider uncertainties in the mechanical and geometrical properties of the pipeline and/or the crack assessment models not being perfectly accurate. As suggested in

Canadian Standard Association (CSA) Z662:19 [39], it is essential to quantify the model error and incorporate it into the reliability analysis since it can be a dominating source of uncertainty. Unfortunately, CSA Z662:19 [39] does not provide sufficient guidance on how to quantify and incorporate the model error into the reliability analysis.

Numerical approaches such as the extended finite element method are widely used to simulate the crack propagation. However, conducting assessments using numerical approaches can be computationally expensive. Alternatively, machine learning techniques such as artificial neural network have been used to predict the failure pressure of pipelines with corrosion or dents. No attempt has been made on failure pressure prediction of cracked pipes using ANN. Even though the CorLAS^{TM} model is conceived to be the most accurate model as reported in the literature [16-20], it has been observed to associated with a relatively high model error, meaning that a considerably high safety factor would be required to account for the uncertainty associated with the model. Hence, a novel predictive tool with a smaller model error is needed to make reliable predictions.

To generate a large database for the development of ANN model, extensive parametric studies based on XFEM need to be conducted. However, traditional calibration of XFEM damage parameters, while effective in achieving accurate results, often incurring high computation costs. As mentioned in the previous section, analytical models evaluate failure based on fracture toughness which is generally estimated from CVN energy, therefore, there is a lack of correlation between CVN energy and XFEM damage parameters. The developed relationship would enable the direct selection of damage parameters without the need for re-calibration and provide pipeline operators with valuable guidance for selecting appropriate XFEM damage parameters based on known Charpy V-Notch impact energy values.

1.4 Research Objectives

The overarching aim of this research is to examine the performance of the CorLAS^{TM} model and develop a novel model for predicting the failure pressure of thin-walled pipelines containing axial surface cracking using artificial neural network (ANN). Specific aims are summarized as follows:

(1) Evaluate the performance of the CorLAS^{TM} model Version 2 using the same collected 103 full-scale burst test datasets as in Yan et al. [19] and compare the predictions of failure pressure using CorLAS^{TM} Versions 2 with those using Version 1 as reported in [19].

(2) Incorporate the model error into the reliability analysis and investigate the effect of pipe geometry and crack dimensions on the relationship between probability of failure and safety factor. The probability of failure is calculated using the Monte Carlo simulation (MCS) and failure pressure is predicted using the CorLAS^{TM} model.

(3) Establish the accuracy of XFEM models in assessing the severity of cracked pipelines based on more than 100 full-scale test data collected from the literature. A correlation between the Charpy V-notch impact energy and the XFEM damage properties (i.e., MAXPE and Gc) is developed.

(4) Compare the predictions between the XFEM-predicted and CorLAS^{TM}-predicted values with full-scale test data.

(5) Develop an ANN model for predicting the failure pressure of pipelines with axial cracks based on the datasets generated from XFEM parametric results. Extensive parametric analyses are performed to generate a sufficiently large database.

1.5 Thesis Outline

This research is prepared in a paper-based format as specified by the Faculty of Graduate Studies and Research (FGSR) at the University of Alberta, Edmonton, Alberta, Canada. A total of 7 chapters are included in this doctoral thesis. Each chapter, expect Chapter 1 and 7, is prepared in a manuscript format with its own list of notations and references. It is important to note that certain information, such as research background, methodology, and references, may be repeated in different chapters.

Chapter 1 provides a general introduction of the research topic, including background information, a review of relevant literature in the interested area, problem statement, research objectives, and thesis organization.

Chapter 2 examines the performance of CorLAS^{TM} version 2 based on a collection of 103 full-scale experimental data from the literature and determines the associated statistical parameters,

namely, mean and CoV. A comprehensive reliability-based assessment is conducted incorporating the model error of CorLAS^{TM}. The PoF is calculated based on Monte Carlo Simulation (MCS).

Chapter 3 conducts a further investigation on the CorLAS^{TM} model by studying its strain hardening exponent formula. The applicability and the accuracy of the stress-strain model in CorLAS^{TM} and other commonly models are explored by fitting to the experimental data obtained from tensile tests conducted at the University of Alberta. Parametric study is conducted to evaluate the effect of varying strain hardening exponent on the failure pressure predicted by CorLAS^{TM} with four different crack sizes (short and shallow, short and deep, long and shallow, and long and deep).

Chapter 4 carries out a parametric study to investigate the effect of the crack shape (i.e., sharp and blunted crack) on the failure pressure of cracked pipelines and the difference between the two shapes of cracks on the ductile fracture response of pipelines. The sharp crack is idealized as a rectangular-shaped defect with uniform depth and the blunted crack is modelled as a notch with a finite tip radius.

Chapter 5 establishes a relationship between the Charpy impact energy and XFEM damage properties (MAXPE and Gc). A sensitivity study is conducted to understand the implication of the damage parameters on the fracture behavior of cracked pipelines. XFEM damage parameters are calibrated and validated by comparing the perditions with the test values reported in the literature.

Chapter 6 develops an ANN model for assessing a crack in pipelines using the parametric results from numerous XFEM simulations. In XFEM models, damage parameters are determined from the CVN impact energy based on the correlation established in Chapter 5. The ANN model is validated using the numerical and full-scale burst test results. The performance of the ANN model is compared with CorLAS^{TM}.

Chapter 7 summarizes the research contribution, provides concluding remarks, as well as some recommendations for future work.

References

[1] Eiber, R.J. and Kiefner, J.F. Failures of pipelines, Failure Analysis and Prevention, Vol 11, Edited by Becker, W.T. and Shipley, R.J. *ASM International*, 2002.

[2] Natural Resources Canada (NRCan). Pipelines across Canada. https://www.nrcan.gc.ca/our-natural-resources/energy-sources-distribution/clean-fossil-fuels/pipelines/pipelines-across-canada/18856, Accessed on May 1st, 2022.

[3] CBC News. Pipelines and why they fail in Canada. https://www.cbc.ca/news/business/cepa-2016-safety-report-1.3654640, Accessed on May 1st, 2022.

[4] Utilities Kingston. Water main breaks. https://utilitieskingston.com/Water/mainbreaks, Accessed on December 10th, 2022.

[5] Daily Telegraph. West Ryde water main bursts again. https://www.dailytelegraph.com.au/newslocal/news/burst-water-main-near-goodwin-st-in-west-ryde-causes-havoc-this-afternoon/news-story/5de15aadf548ed48bc9c07a761362134, Accessed on April 6th, 2022.

[6] Cazenave, P., Gao, M., Moneta, A, Cruzado, J. and Hryciuk, P. An onshore pipeline failure due to hydrogen assisted cracking induced by cathodic protection operated at near -1200 mV CSE – a case study. Paper No. IPC2020-9396, *Proceedings of the 2020 13th International Pipeline Conference, American Society of Mechanical Engineers*, Virtual, Online, 2020.

[7] Kiefner, J.F., Maxey, W.A., Eiber, R.J. and Duffy, A.R. Failure stress levels of flaws in pressurized cylinders. Progress in flaw growth and fracture toughness testing, STP 536, *ASTM International*, West Conshohocken, PA, pp. 461-481, 1973.

[8] Jaske, C.E., Beavers, J.A. and Harle, B.A. Effect of stress corrosion cracking on integrity and remaining life of natural gas pipelines, Paper No. 255, Corrosion 96, NACE International, Houston, 1996.

[9] Jaske, C. E. and Beavers, J. A. Integrity and remaining life of pipe with stress corrosion cracking. PRCI 186-9709, Catalog No. L51928. Pipeline Research Council International, Falls church, 2001.

[10] Polasik, S.J., Jaske, C.E. and Bubenik, T.A. Review of engineering fracture mechanics model for pipeline applications, Paper No. IPC2016-64605, *Proceedings of the 2016 11th International Pipeline Conference, American Society of Mechanical Engineers*, Calgary, Canada, 2016.

[11] Dowling, A.R. and Townley, C.H.A. The effects of defects on structural failure: a two-criteria approach. *International Journal of Pressure Vessels and Piping*, 3(2), 77-107, 1975.

[12] API 579-1/ASME FFS-1, Fitness-for-service, American Society of Mechanical Engineers, USA, 2019.

[13] British Standards Institution. BS 7910. Guide to methods for assessing the acceptability of flaws in metallic structures. London, UK, 2019.

[14] EDF Energy. R6: Assessment of the Integrity of the Structures Containing Defect. Gloucester, UK amendment 10 R6, revision 5, 2013.

[15] British Steel, SINTAP: Final Procedure: Structural Integrity Assessment Procedures for European Industry. European Union Brite-Euram Programme, Project number BE-1426, Contract number BRPR-CT95-0024, Rotherham, British, 1999.

[16] Rothwell, A.B. and Coote, R.I. A critical review of assessment methods for axial planar surface flaws in pipe. *In: International Conference on Pipeline Technology*, Ostend, Belgium, 2009.

[17] Hosseini, A., Cronin, D., Plumtree, A. and Kania, R. Experimental testing and evaluation of crack defects in line pipe. Paper No. IPC2010-31158, *Proceedings of the 8th International Pipeline Conference*, *American Society of Mechanical Engineers,* Calgary, Canada, 2010.

[18] Tandon, S., Gao, M., Krishnamurthy, R., Kariyawasam, S. and Kania, R. Evaluation of existing fracture mechanics models for burst pressure predictions. Theoretical and Experimental Aspects, Paper No. IPC2014-33563, *Proceedings of the 2014 10th International Pipeline Conference, American Society of Mechanical Engineers,* Calgary, Canada, 2014.

[19] Yan, Z., Zhang, S. and Zhou, W. Model error assessment of burst capacity models for energy pipelines containing surface cracks, *International Journal of Pressure Vessels and Piping*, 120-121: pp. 80-92, 2014.

[20] Yan, J., Zhang, S., Kariyawasam, S., Pino, M. and Liu, T. Validate crack assessment models with In-service and Hydrotest Failures. Paper No. IPC2018-78251, *Proceedings of the 2018 12th International Pipeline Conference, American Society of Mechanical Engineers,* Calgary, Canada, 2018.

[21] Tosun, E. and Calik, A. Failure load prediction of single lap adhesive joints using artificial neural networks. *Alexandria Engineering Journal*, 55(2), 1341-1346, 2016.

[22] Oh, D., Race, J., Oterkus, S. and Koo, B. Burst pressure prediction of API 5L X-grade dented

pipelines using deep neural network. *Journal of Marine Science and Engineering*, 8(10), 766, 2020.

[23] Liu, X. Xia, M. Bolati, D. Liu, J. Zheng, Q. and Zhang, H. An ANN-based failure pressure prediction method for buried high-strength pipes with stray current corrosion effect. *Energy Science & Engineering*. 8(8), 248–259, 2020.

[24] Xu, W., Li, C.B., Choung, J. and Lee, J. Corroded pipeline failure analysis using artificial neural network scheme. *Advances in Engineering Software*. 112(11-12): 255-266, 2017.

[25] Belytschko T. and T. Black. Elastic crack growth in finite elements with minimal remeshing. *International Journal for Numerical Methods in Engineering*, 45, 601-620, 1999.

[26] Melenk, J.M. and Babuška, I. The partition of unity finite element method: basic theory and applications. *Computer Methods in Applied Mechanics and Engineering*, 139(1-4): 289–314, 1996.

[27] Agbo, S. A novel tool for predicting the tensile strain capacity of welded onshore vintage pipelines. Ph.D. Thesis, University of Alberta, Edmonton, Canada, 2020.

[28] Lin, M. Characterization of tensile and fracture properties of X52 steel pipes and their girth welds. M.Sc. Thesis, University of Alberta, Edmonton, Canada, 2015.

[29] Okodi, A., Lin, M., Yoosef-Ghodsi, N., Kainat, M., Hassanien, S. and Adeeb, S. Crack propagation and burst pressure of longitudinally cracked pipelines using extended finite element method. *International Journal of Pressure Vessels and Piping*, 184(5): 104115, 2020.

[30] Kiefner, J.F. Modified equation aids integrity management. *Oil & Gas Journal*, 106 (37), 78–82, 2008a.

[31] Kiefner, J.F. Modified ln-secant equation improves failure prediction. *Oil & Gas Journal*, 106 (38), 64–66, 2008b.

[32] Moon, D.H., Par, J.Y. and Kim, M.H. Effects of the crack tip constraint on the fracture assessment of an AI5083-O weldment for low temperature applications. *Materials*, 10(7), 815, 2017.

[33] Dassault Systèmes, 2022. Abaqus documentation.

[34] ANSYS Release 12.1 Documentation. Ansys Inc, USA, 2009.

[35] Malíková, L., Razavi, N. and Berto, F. Crack propagation in a brittle DCB specimen assessed by means of the Williams' power expansion. *Frattura ed Integrità Strtturale*, 13(48), 34-41, 2019.

[36] Abaqus 6.14. Abaqus Analysis User's Guide, Dassault Systèmes, 2014.

[37] Pipeline and Hazardous Materials Safety Administration (PHMSA) of USA, 2019. Pipeline safety: safety of gas transmission pipelines. Docket No. PHMSA-2011-0023.

[38] Lin, M. Novel XFEM variable strain damage model for predicting fracture in small-scale SENT and full-scale pipeline. Ph.D. Thesis, University of Alberta, Edmonton, Canada, 2021.

[39] CSA. Oil and gas pipeline systems. CSA Standard Z662:19, Canada Standards Association, Mississauga, Ontario, Canada, 2019.

[40] Zhang, X., Okodi, A., Tan, L., Leung, J.Y. and Adeeb, S. Failure pressure prediction of crack in corrosion defects using XFEM. Paper No. IPC2020-9312, *Proceedings of the 2020 13th International Pipeline Conference*, *American Society of Mechanical Engineers*, Virtual, Online, 2020.

[41] Zhang, X., Okodi, A., Tan, L., Leung, J.Y. and Adeeb, S. Failure pressure prediction of crack in corrosion defects in 2D by using XFEM. Paper No. PVP2020-21046, *Proceedings of the Pressure Vessel and Piping Conference*, *American Society of Mechanical Engineers,* Virtual, Online, 2020.

[42] Lin, M., Agbo, S., Cheng, J.J.R., Yoosef-Ghodsi, N. and Adeeb, S. Application of the Extended Finite Element (XFEM) to Simulate Crack Propagation in Pressurized Steel Pipes. Paper No. PVP2017-65575, *Proceedings of the Pressure Vessel and Piping Conference, American Society of Mechanical Engineers,* Hawaii, USA, 2017.

[43] Agbo, S., Lin, M., Amerli, I., Imanpour, A., Duan, D-M., Cheng, J.J.R. and Adeeb, S. Evaluation of the effect of internal pressure and flaw size on the tensile strain capacity of X42 vintage pipeline using damage plasticity model in extended finite element method (XFEM). Paper No. PVP2019-94005, *Proceedings of the Pressure Vessel and Piping Conference, American Society of Mechanical Engineers*, San Antonio, Texas, USA, 2019.

CHAPTER 2: RELIABILITY-BASED ASSESSMENT OF CRACKED PIPELINES USING MONTE CARLO SIMULATION TECHNIQUE WITH CORLAS™

This chapter is derived from a published conference proceeding:

Zhang, X., Zheng, Q., Leung, J.Y. and Adeeb, S., Reliability-based Assessment of Cracked pipelines using Monte Carlo Simulation Technique with CorLAS™, Proceeding of the ASME 2022 Pressure Vessels & Piping Conference, July 17-22, 2022, Las Vegas, Nevada, USA, PVP2022-80412, doi:10.1115/PVP2022-80412.

Abstract

If not assessed properly, unstable crack growth in pipelines could result in detrimental leaks or ruptures. Fracture mechanics models are typically used to assess the susceptibility of pipelines to fail due to the presence of cracks or crack-like anomalies. To this end, an inelastic (or elastic-plastic) fracture mechanics model, known as CorLAS^{TM} model, has been developed and frequently used by pipeline operators. This paper first reviews the development of the CorLAS^{TM} model and derives the probabilistic characteristics, including mean and coefficient of variation (CoV) associated with the CorLAS^{TM} model using a collection of 103 full-scale burst test data from the literature. A comprehensive reliability assessment of cracked pipes based on the CorLAS^{TM} model is performed through the Monte Carlo Simulation (MCS) method. For each reported scenario, the probability of failure (PoF) is calculated by MCS that considers the uncertainties associated with various parameters such as pipe geometry, material properties, and the uncertainty due to the fracture model itself, namely, the model error. Finally, a sensitivity study is conducted considering various input parameters, including pipe grade, pipe diameter, wall thickness, ratio of crack length to depth, ratio of crack depth to wall thickness, and model error CoV. The results suggest that the PoFs are highly sensitive to the CoV, i.e., the PoFs increase significantly with the increase of the CoVs, while the effects of other input parameters on the PoFs are insignificant. It is also shown that the model error CoV of CorLAS^{TM} with a value of 14% could serve as a reference value for future model error studies.

Keywords: Model error; Monte Carlo Simulation; CorLAS; Probability of failure; Pipeline

2.1 Introduction

Buried steel pipelines, which are designed to convey hydrocarbons (e.g., crude oil, gas, and their mixtures) over long distances, may experience failure as a result of mechanical damage in the form of cracks [1]. In the case of pipeline failure, the spilled products can pose an adverse effect on the surrounding environment and human safety due to the hazardousness of the transported fluids. In addition, massive costs are required for repairing or replacing the defective pipeline segments. Consequently, the reliability of cracked pipelines should be systematically evaluated in order to protect the environment and the public.

Traditionally, deterministic approaches have been utilized by the pipeline industry to make integrity decisions due to their simplicity, but they can lead to unduly conservative solutions since the methods are based on conservative inputs and cannot account for the uncertainties of the input variables and the model error. In this regard, probabilistic methods are introduced and implemented to model the uncertainties. Probabilistic methods can be classified into three major categories, namely, local reliability methods, global reliability methods, and sampling methods [2]. The first category uses the local approximation of the limit state function (LSF) in the calculation of the failure probability. Several methods, such as the mean value first-order second moment (MVFOSM) method, first-order reliability method (FORM), second-order reliability method (SORM), and response surface method (RSM), have been used to obtain a local approximation of the LSF. Global reliability methods are based on the global approximation model of the LSF, i.e., efficient global reliability analysis (EGRA). Sampling methods (or simulation methods) such as the Monte Carlo Simulation (MCS) are perceived to be the most accurate ones to evaluate the probability of failure (PoF) and are well accepted by the pipeline industry.

Over the past few decades, a number of fracture models have been proposed to predict the failure pressure for pipelines containing axial cracks, for example, the well-known American Petroleum Institute's Recommended Practice 579 (API 579), British Standard 7910 (BS 7910), and R6 defect assessment procedures by means of the failure assessment diagram (FAD), Log-Secant model, modified Log-Secant model, as well as the software-based methods such as pipe axial flaw failure criteria (PAFFC), CorLAS^{TM} model, and a more recent MAT-8 model. In general, these crack assessment methods can be subdivided into two types, i.e., the pipeline-specific methods which are developed by the pipeline industry and the generic methods that are codified but are not developed specifically for the pipeline industry [3]. An accurate failure pressure prediction plays an essential role in structural reliability analysis. Among the aforementioned models, the CorLAS^{TM} model has been proven to provide the most accurate and precise predictions. Therefore, it is adopted in the current reliability analysis.

The reliability analysis needs to consider uncertainties in the mechanical and geometrical properties of the pipeline and/or the crack assessment models not being perfectly accurate (model error). As suggested in Canadian Standard Association (CSA) Z662:19 [4], it is essential to quantify the model error and incorporate it into the reliability analysis since it can be a dominating source of uncertainty. To ensure an accurate representation of the level of risk of the defective

pipeline, it is of paramount importance to properly take all the input parameter uncertainties into consideration. Unfortunately, CSA Z662:19 [4] does not provide sufficient guidance on how to quantify and incorporate the error into a model.

Currently, two published sources of model error associated with CorLAS^{TM} are available [5,6]. Yan et al. [5] studied the model error distribution of CorLAS^{TM} (Version 1) using a collection of 103 full-scale burst test data from the literature, the reported model error of CorLAS^{TM} (Version 1) was following a normal distribution with a mean of 0.96 and CoV of 22.8%. Whereas the corresponding mean and CoV of model error associated with CorLAS^{TM} (Version 2) were 1.11 and 14%, respectively, as reported by [6] based on 12 in-service and 63 hydrostatic test pipe ruptures due to external stress corrosion cracking (SCC). Apparently, there is a discrepancy between the corresponding model errors associated with these two publications. Hence, it is essential to determine which source of model error is more appropriate to use in the reliability assessment when incorporating the model error of CorLAS^{TM} explicitly.

The aim herein is to evaluate the model error distribution of CorLAS^{TM} Version 2 by using the same dataset as in [5], investigate the effects of varying input variables (model error CoV, pipe grade, pipe geometry, and crack size) on PoFs, and explore the relationship between PoFs and safety factor. This chapter begins with a comprehensive overview of CorLAS^{TM} where the differences in terms of the equations between Version 1 and Versions 2 & 3 are discussed. The basic concepts of limit state and MSC method are then presented in the following sections with details. The results of this chapter are expected to facilitate the application of model error in the reliability analysis of cracked pipelines.

2.2 CorLAS^{TM} Model

Jaske and Beavers [7] developed a J-based fracture model which was implemented in a computer program developed by Cortest Columbus Technologies, Inc. (CC Technologies) known as CorLAS^{TM} (Corrosion Life Assessment Software). For simplicity, the underlying fracture model within the software is referred to as CorLAS^{TM}. Originally, the CorLAS^{TM} model was designed to address the issue of pipes associated with SCC, which is a type of environmental assisted cracking (EAC), but it has also been widely used by the pipeline industry to predict the failure and remaining life of pipelines containing axially-oriented surface cracks. In the model, the crack-depth profile

is characterized along with two failure criteria: flow strength and fracture toughness. Failure is predicted using the criterion which gives the least calculated failure pressures or the smallest calculated crack size. The failure pressure, P_f, is given by:

$$P_f = min\{\sigma_{flow}, \sigma_t\}\frac{2t}{D}\left(\frac{1-\frac{A}{A_0}}{1-\frac{A}{MA_0}}\right) \tag{2-1}$$

where σ_{flow} and σ_t are the flow stress for the flow-strength criterion and failure stress for the toughness criterion, respectively, t is the pipe wall thickness, D is the pipe diameter, A is the effective crack area, A_0 is the reference area $(t \times L)$, and M is the Folias factor that accounts for the stress increase due to the local bulging of a defected pipe under internal pressure, which is a function of crack length (L) relative to D and t, and can be expressed as:

$$M = \begin{cases} \sqrt{1 + 0.6275\frac{L^2}{Dt} - 0.00375\left(\frac{L^2}{Dt}\right)^2}, \frac{L^2}{Dt} \leq 50 \\ 3.3 + 0.032\frac{L^2}{Dt}, \frac{L^2}{Dt} > 50 \end{cases} \tag{2-2}$$

If a detailed crack-depth profile is available, the effective area method (EAM) is adopted, where the effective area is defined by the effective length and the actual cross-sectional depth. The effective crack depth is defined based on a semi-elliptical shape with equivalent effective area. Otherwise, the flaw profile is assumed to have a semi-elliptical shape with the length and depth equal to the maximum measured values (**Figure 2-1**).

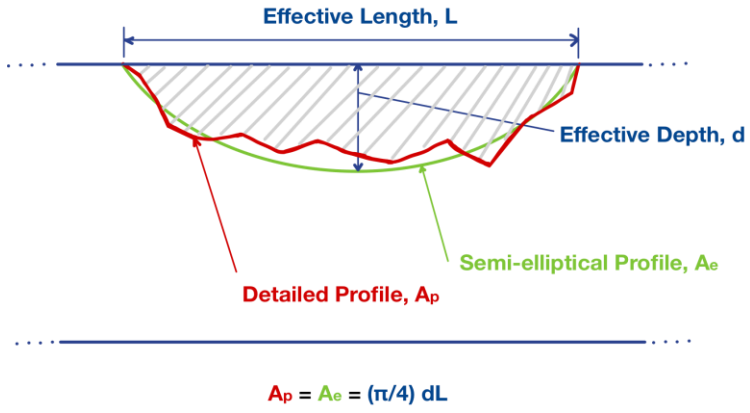

Figure 2-1: Effective area method (EAM), adapted from [8]

2.2.1 Version 1

- **Flow strength-dependent failure mode**

For the flow-strength failure criterion, the nominal stress at failure (σ_f) is calculated based on the EAM and can be computed using the flow strength (σ_{flow}) as expressed below:

$$\sigma_f = \sigma_{flow}\text{RSF} = \sigma_{flow}\left(\frac{1-\frac{A}{A_o}}{1-\frac{A}{MA_o}}\right) \tag{2-3}$$

RSF is the remaining strength factor. The flow strength is a measure of the stress at which the material starts to yield considerably or "flow" and is traditionally given as a function of the tensile yield strength (σ_{YS}) and the ultimate tensile strength (σ_u) using either of the following equations.

$$\sigma_{flow} = \sigma_{YS} + 68.75\ \text{MPa} \tag{2-4}$$

$$\sigma_{flow} = \sigma_{YS} + C(\sigma_u - \sigma_{YS}) \tag{2-5}$$

C is a constant parameter with a value ranging from 0 to 1. In general, C is taken to be 0.5 meaning that σ_{flow} is equal to the average of σ_{YS} and σ_u. For materials having values of σ_{YS} close to σ_u, C can be taken as 1. Eq. (2-4) is more frequently used as it gives more accurate failure pressure predictions and is applicable to a wide range of pipeline steels [8]. The failure pressure for the flow strength criterion can be computed by:

$$P_{f(flow)} = \frac{\sigma_{flow}}{(\frac{D}{2t}-y)}\left[\frac{1-\frac{A}{A_o}}{1-\frac{A}{MA_o}}\right] \tag{2-6}$$

where y is a factor that depends on the temperature and *t*. For a thin-walled pipe ($\frac{D}{t} > 20$), y is taken as 0; otherwise, y is equal to 0.4 [7].

- **Fracture toughness-dependent failure mode**

The CorLAS^{TM} model employs inelastic fracture mechanics (IFM) procedures using J-integral formulations to evaluate the fracture toughness-dependent failure. The J-integral (J) value is computed iteratively until the applied value of J equals or exceeds the critical value of J fracture toughness (J_c), the corresponding nominal stress is used to calculate the failure pressure. The following equation is used to compute the J-integral driving force for a semi-elliptical surface flaw:

$$J = Q_f F_{sf}[\frac{\sigma^2 \pi a}{E} + f_3(n) a \varepsilon_p \, \sigma] \tag{2-7}$$

where Q_f and F_{sf} are geometrical factors, a is the crack depth, ϵ_p is the equivalent plastic strain computed using the applied stress (σ) as shown in Eq. (2-10), while $f_3(n)$ is a dimensionless factor that depends on the strain hardening exponent (n). For fully plastic conditions, Q_f is computed using the following expression:

$$Q_f = 1.6260 - 1.4795\left(\frac{a}{L}\right) - 6.3428\left(\frac{a}{L}\right)^2 - 10.261\left(\frac{a}{L}\right)^3 \tag{2-8}$$

The values of F_{sf} is calculated using the following relation:

$$F_{sf} = \begin{cases} \left[\frac{2t}{\pi a}\tan\left(\frac{\pi a}{2t}\right)\right]^{\frac{1}{2}}, 0 < \frac{a}{t} < 0.95 \\ 2.918, 0.95 \leq \frac{a}{t} \leq 1.0 \end{cases} \tag{2-9}$$

ε_p is computed using a power-law σ-ε relationship:

$$\varepsilon_p = K\sigma^n \tag{2-10}$$

K is the strength coefficient and can be calculated as:

$$K = \frac{\sigma_{YS}}{(0.005 - \frac{\sigma_{YS}}{E})^n} \tag{2-11}$$

Where,

$$n = 0.0936 + 0.685\frac{\sigma_{YS}}{\sigma_u} - 0.774(\frac{\sigma_{YS}}{\sigma_u})^2 \tag{2-12}$$

The strain hardening factor $f_3(n)$ can be expressed as follows:

$$f_3(n) = \left[3.85\sqrt{\frac{1}{n}}(1-n) + \pi n\right](1+n) \tag{2-13}$$

The value of the local stress (σ) is the product of the nominal stress (σ_n) and the Folias factor for a surface crack (M_{sf}) which is calculated by:

$$M_{sf} = 1 + \frac{(M-1)\pi a}{4t} \tag{2-14}$$

The critical value of J fracture toughness can either be measured directly from standard laboratory tests (e.g., fracture toughness tests) or estimated from Charpy V-notch impact energy (CVN). It is recommended to use the actual J fracture toughness data. However, detailed

information of J_c is generally unavailable in practice, the values of CVN obtained from full-size specimens are adopted by pipeline operators to estimate the fracture toughness using the following empirical correlations [7]:

$$J_c = \frac{12\ \text{CVN}}{A_c} = \frac{12\ \text{CVN (ft−lb)}}{0.124\ (\text{in}^2)} \tag{2-15}$$

$$J_c = 8\ \text{CVN (ft} - \text{lb)} \tag{2-16}$$

The Eq. (2-15) is based on the correlation proposed by Kiefner et al. [9] for Log-Secant method, which provides high fracture toughness values and found to corroborate well with full-scale pipe burst tests, whearas Eq. (2-16) is based on the correlation originally developed for nuclear pipeline steels [10] and found to provide a low value of J_c resulting in conservative predictions of pipe failures. Therefore, Eq. (2-15) is preferred and widely used by the industry [8].

2.2.2 Version 2&3

As the CorLAS^{TM} (Version 1) provides overly conservative predictions for long cracks ($\frac{L}{d} > 50$) when failure was governed by fracture toughness, while it gives reasonably well predictions when using the flow strength-dependent failure criterion [11]. In 2001, a project was launched by PRCI to improve the original model and develop the CorLAS^{TM} (Version 2). Recently, Det Norske Veritas (DNV) developed CorLAS^{TM} (Version 3) where the user interface was simpler, but the equations remained the same as in Version 2. Therefore, the resulting failure pressure predictions will be the same using either one of the modified models. The major modifications in Version 2 and Version 3 are presented as followed:

Tearing instability

In CorLAS^{TM} Version 1, the toughness-dependent failure is predicted to occur only when the applied J value reaches the value of J_c which can be measured from laboratory tests. There is some conservatism since the ductile tearing could occur prior to the fracture instability for ductile and tough pipelines [11]. To address this problem, a tearing instability criterion for fracture-

toughness failure is incorporated into the model. Tearing instability is predicted to occur when the applied crack tearing parameter (T) equals or exceeds the tearing modulus (T_{mat}).

$$T_{mat} = \frac{E}{\sigma_{flow}^2}\frac{dJ}{da} \tag{2-17}$$

Toughness failure can be predicted using the tearing instability criterion when a J-integral based crack resistance curve (J-R curve) is available. It should be noted that one of the improvements in the modified CorLAS™ model is that the user has the option to choose either J_C or T_{mat} as the fracture toughness-dependent criterion.

Formulations of computing J

The formulations of computing the J value for semi-elliptical surface flaws were improved by modifying the equations in the CorLAS™ Version 1. The total J-integral (J_t) is partitioned into an elastic portion (J_e) and a plastic portion (J_p).

$$J_t = J_e + J_p \tag{2-18}$$

The elastic portion of J-integral can be expressed in terms of the stress intensity factor in Mode I loading condition (K_I) under plane-stress condition using the following expression:

$$J_e = \frac{K_I^2}{E} \tag{2-19}$$

For a surface crack, K_I is computed through the following equation derived by Irwin [12]:

$$K_I = \frac{\sigma}{\Phi}\sqrt{\pi a}\left(sin_{\varphi}^2 + \frac{a^2}{c^2}cos_{\varphi}^2\right)^{\frac{1}{4}} \tag{2-20}$$

where c is the half-length of the crack, φ is the coordinate angle (**Figure 2-2**), Φ is the complete elliptic integral of the second kind and represented by:

$$\Phi = \int_0^{\frac{\pi}{2}} \sqrt{1 - \left[\frac{c^2 - a^2}{c^2}\right]\sin^2\varphi}\, d\varphi \tag{2-21}$$

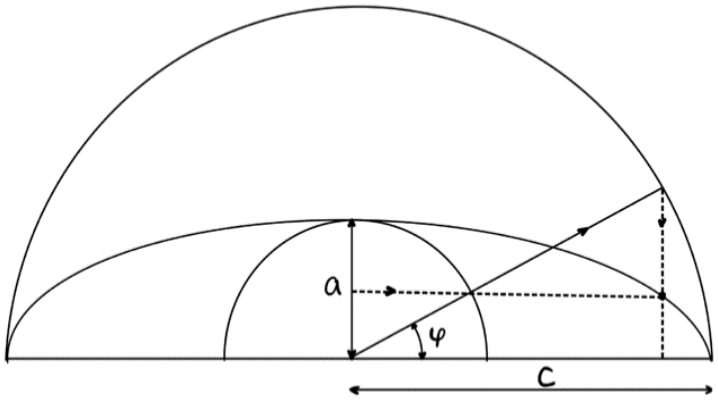

Figure 2-2: Elliptical crack profile, adapted from [13]

In comparison to edge cracks, surface flaws equations for K_I require a correction of 12 percent. This is the so-called back free-surface correction [14]. Also, a correction factor is needed to account for the proximity of the free surface in front of the crack. For this purpose, the front free-surface correction (M_k) is adopted from Kobayashi et al. [15]. A plastic zone correction (PZC) is a correction to the crack size and is usually included considering that the plastic deformation occurs at the crack tip, which means that the crack behaves as if it was slightly longer than its physical size. When the plastic zone size is considered, the stress tensity factor is expressed by ($\varphi = \frac{\pi}{2}$):

$$K_I = 1.12 M_k \frac{\sigma}{\Phi} \sqrt{\pi (a + r_p^*)} \tag{2-22}$$

$$r_p^* = \frac{1}{4\sqrt{2}\pi} \frac{K_I^2}{\sigma_{YS}^2} \tag{2-23}$$

Substituting Eq. (2-23) into Eq. (2-22), gives

$$K_I = \frac{1.12 M_k \, \sigma \sqrt{\pi a}}{\sqrt{\Phi^2 - 0.212 (\frac{\sigma}{\sigma_{YS}})^2}} \tag{2-24}$$

The equation under the radical in the denominator in Eq. (2-24) is defined as Q, which is a flaw shape parameter. Eq. (2-19) can be rewritten using Eq. (2-8) as:

$$J_e = Q_f F_{sf} a \, \frac{\sigma^2 \pi}{E} \tag{2-25}$$

Q_f is the elliptical-correction shape factor ($Q_f = \frac{1.12^2}{Q}$) with F_{sf} denoting the free-surface-correction factor ($F_{sf} = M_k^2$). It should be emphasized that compared to the previous model, Q_f is modified slightly to eliminate the effective plastic zone correction (r_p^*) to crack size. This is because, the predictions of failure conditions were more accurate when the crack-tip plastic zone correction was not incorporated in the model, as shown by Jaske and Beavers [11]. In the absence of the consideration of the crack-tip plastic zone size correction, the ratio of $\frac{\sigma}{\sigma_{ys}}$ is 0, thus, Q is equal to Φ^2. Hence, Q_f can be formulated as:

$$Q_f = 1.2581 - 0.20589\left(\frac{a}{L}\right) - 11.493\left(\frac{a}{L}\right)^2 + 29.586\left(\frac{a}{L}\right)^3 - 23.584\left(\frac{a}{L}\right)^4 \quad (2\text{-}26)$$

The value of F_{sf} is computed using the following empirical relation:

$$F_{sf} = \begin{cases} 1.0, \ \frac{a}{t} \leq 0.01 \\ \frac{2t}{\pi a}\tan\left(\frac{\pi a}{2t}\right)\left(1 - \frac{2a}{L}\right) + \frac{2a}{L}, 0.01 < \frac{a}{t} \leq 0.95 \\ \left[8.515 + (\frac{a}{t} - 0.95)\frac{162}{t}\right]\left(1 - \frac{2a}{L}\right) + \frac{2a}{L}, \frac{a}{t} > 0.95 \end{cases} \quad (2\text{-}27)$$

The EAM is employed to compute the local stress (σ) which is shown below:

$$\sigma = \begin{cases} \sigma_n \left[\frac{1-\frac{\pi a}{4tM}}{1-\frac{\pi a}{4t}}\right], \text{external flaw} \\ (\sigma_n + P\frac{\pi a}{4t}) \left[\frac{1-\frac{\pi a}{4tM}}{1-\frac{\pi a}{4t}}\right], \text{internal flaw} \end{cases} \quad (2\text{-}28)$$

The geometrical factors (Q_f and F_{sf}) in the plastic portion of J-integral formulation remain the same as J_e. The expression for J_p can be written as follows:

$$J_p = Q_f F_{sf} a f_3(n) \epsilon_p \, \sigma \quad (2\text{-}29)$$

Eq. (2-18) can be rewritten as:

$$J_t = Q_f F_{sf} a[\frac{\sigma^2 \pi}{E} + f_3(n)\varepsilon_p \, \sigma] \quad (2\text{-}30)$$

The strain hardening exponent in the original model was obtained from calibrated data for carbon and low-alloy steels, while the modified expression for strain hardening exponent was obtained using data of pipeline steels from past studies.

$$n = -0.00546 + 0.556\frac{\sigma_{YS}}{\sigma_u} - 0.547(\frac{\sigma_{YS}}{\sigma_u})^2 \quad (2\text{-}31)$$

In comparison with Version 1, the major modification is the expression for J_p. Jaske and Beavers [11] evaluated the modifications by comparing the J_p values obtained from the modified equations with the published finite-element stress analysis results, where the J integral was computed employing the virtual crack extension technique. It is shown that the adjusted formulations could provide reasonable approximations of the stress analysis results.

Interaction flaw criteria

Jaske and Beaver [16] reported that multiple surface flaws often develop on oil and gas pipelines due to the presence of SCC. If the interaction happens, the failure pressure will decrease. In this context, a procedure for evaluating the flaw interaction is incorporated into the modified CorLAS^{TM} model for flow-strength and fracture-toughness failure criteria.

For the flow-strength failure criterion, the evaluation procedure is based on the EAM and is done by repeating the Eq. (2-3) for all possible flaw combinations. If the single flaw has the lowest RSF value, no interaction is expected; otherwise, flaw interaction should be considered. For the fracture-toughness failure criterion, multiple flaws are assessed by comparing the applied J integral values. If the J value for the combined flaws reaches or exceeds the value for the individual flaw, flaw interaction should be considered.

Overall, Jaske and Beavers [17] reviewed the modifications made to Versions 2 & 3 and concluded that the overly conservative predictions for long cracks in the Version 1 has been successfully removed.

2.2.3 Model Error

The performance of the CorLAS^{TM} model have been studied in the existing literature based on a variety of sources. For example, Yan et al. [5] conducted a study comparing five commonly used crack assessment models/methodologies (Log-secant and CorLAS^{TM} Version 1 models, the FAD methodologies recommended in BS7910, API 579, and R6) based on 103 full-scale test data collected from the literature [9,18-25]. Among the five crack models, CorLAS^{TM} Version 1

provided the most accurate predictions with the corresponding model error characterized by a normal (or Gaussian) distribution with a mean equal to 0.96 and a CoV of 22.8%.

Although the accuracy of CorLAS^{TM} Version 1 is high (the average value of test-to-predicted failure pressure ratio is close to 1), comparison with the experiments indicates a high value for the CoV. As discussed in Zheng et al. [26], when employing the model error of CorLAS^{TM} derived by [5] in a reliability analysis, the resulting PoF can be as high as 2.0E-01.

As mentioned previously, there is a noticeable discrepancy between the reported model errors of CorLAS Version 1 and 2. Therefore, an investigation of the probabilistic characteristics associated with CorLAS^{TM} Version 2 is conducted and presented in **Figure 2-3**. Details of the test data are tabulated in **Appendix A**.

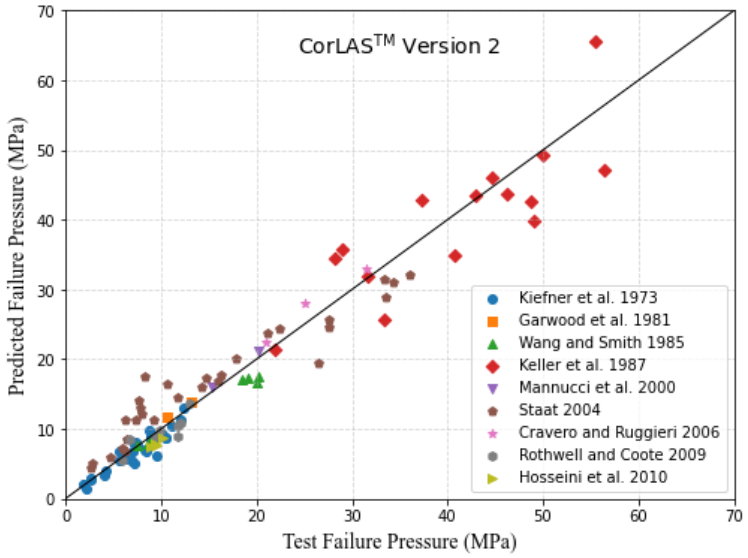

Figure 2-3: Comparison of the predicted and test failure pressures based on the CorLAS^{TM} model

The comparison between the predicted failure pressure and the test failure pressure is depicted by a unity plot, demonstrating the accuracy of CorLAS^{TM} Version 2. As can be observed in **Figure 2-3**, the predicted failure pressures calculated by CorLAS^{TM} Version 2 correspond well with the test data. The area below the unity line (or 1:1 line) indicates conservative predictions, where the test failure pressure is higher than the predicted result. Conversely, the area above the

1:1 line represents unconservative predictions, with the majority of the data points spread along the unity line.

The model error is a factor used to characterize the difference between the predicted pressure and the test pressure, it is defined as the ratio of the test failure pressure to the predicted failure pressure obtained from a given crack model. The test-to-predicted failure pressure ratios corresponding to each test data are calculated for CorLAS^{TM} Version 2. By analyzing the test-to-prediction ratios, the probability characteristics including the mean and CoV associated with Version 2 are derived. The probability distribution is obtained by plotting the test-to-predicted failure pressure ratios on probability papers (**Figure 2-4**). It is shown that the test-to-prediction ratios for the CorLAS^{TM} Version 2 model yields a normal distribution with the mean and CoV equal to 1.01 and 20.8%, respectively. Compared with the predictions based on CorLAS^{TM} Version 1 which reported by [5], the difference between the results is less pronounced. This is because the aim of the modifications on the model is to merely extend the model applicability rather than improve the predictions [17].

However, reviewing the literature again would reveal that the datasets in [18] are less reliable. Although the database in reported by Staat [18] contains a large and comprehensive collection of full-scale burst test data, no first-hand information about the tests is provided. In such a case, using this database for calibrating the predictive model might be the cause for the reported high CoV value. If the datasets in [18] are excluded from the model error calculation, the mean and CoV of the test-to-prediction ratios are 1.07 and 13.9 %, respectively. It is worth mentioning that this CoV value is similar to the one obtained by Yan et al. [6] who investigated the accuracy of CorLAS^{TM} Version 2 using 12 in-service and 63 hydrostatic test pipe ruptures caused by external SCC. This suggests that the model error CoV with a value of 14% could serve as a reference value for future model error studies.

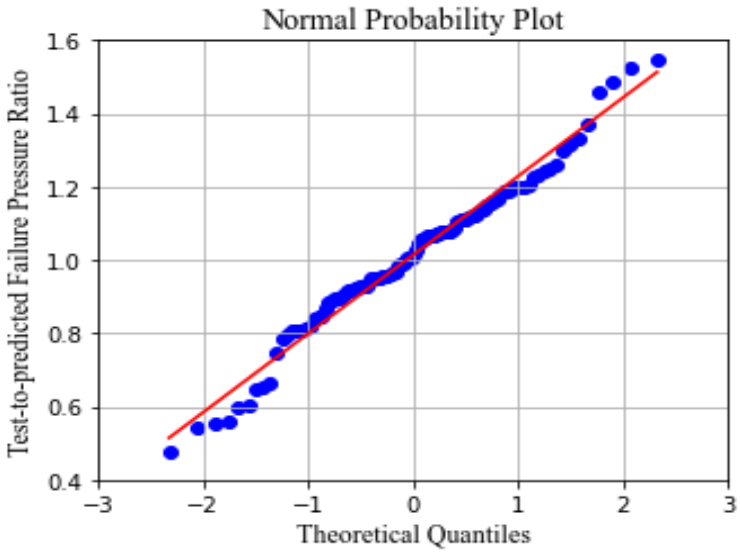

Figure 2-4: Fitted normal distribution of the test-to-predicted failure pressure ratio

2.3 Reliability Analysis

2.3.1 Limit State Function

A limit state (LS) refers to a specific condition beyond which either an entire or part of the structure no longer fulfills functional requirements; in other words, it is the borderline state between safety and failure. According to CSA Z662:19 [4], limit states can be mainly classified into three categories, namely, ultimate limit state (ULS) which leads to loss of containment (LOC) resulting in a significant safety hazard (i.e., a large leak or rupture), leakage limit state (LLS) which is associated with limited LOC (i.e., a small leak), and serviceability limit state (SLS) that fails without leading to a LOC.

The limit state and the performance of structure usually are represented mathematically to quantitatively analyze the structural reliability. Let $X = (X_1, X_2, \dots, X_n)^{\mathrm{T}}$ be a set of basic random variables (RVs) such as geometry, material properties, and loads that govern the performance of the structure. Consequently, the performance function (PF) can be defined as:

$$Z = g(X) = g(X_1, X_2, \dots, X_n) \tag{2-32}$$

As demonstrated in **Figure 2-5**, when $Z > 0$, the structure is in a safe state, $Z < 0$ is the failure state, and $Z = 0$ is the limit state. The function g is the so-called LSF as expressed in Eq. (2-33).

$$Z = g(X) = g(X_1, X_2, \dots, X_n) = 0 \tag{2-33}$$

Depending on the number of random variables, LSF can be simple or complex. If there are only two basic random variables R and L, the LSF is given by:

$$g(X) = R - L \tag{2-34}$$

where R is the resistance and L is the load. Failure will occur if the load exceeds the resistance.

For a cracked pipe subjected to internal pressure, the burst limit state (belonging to ULS) should be used as specified in Table O.1 of CSA Z662:19. The LSF can be expressed as the predicted failure pressure (P_f) minus the maximum annual pressure (MAP) which is a randomly applied pressure and can be estimated using the maximum operating pressure (MOP) (Eq. (2-34)).

$$MAP = R_P \cdot MOP \tag{2-35}$$

Safety factor (SF), also known as failure pressure ratio (FPR), is used to ensure the operating pressure never exceeds the failure pressure. The deterministic MOP can be estimated based on the deterministically calculated failure pressure considering various safety factors (ranging from 1 to 1.4), as expressed in Eq. (2-36).

$$MOP = \frac{P_f}{FoS}, \tag{2-36}$$

where P_f is the predicted failure pressure using CorLAS™.

In order to incorporate the model error into the analysis, the failure pressure needs to be adjusted using a random variable (R) that represents the model error distribution. Normally, the model error distribution is defined by mean ($R_{\bar{x}}$) and CoV (R_{cov}). The adjusted failure pressure (P_f^*) can be estimated by:

$$P_f^* = P_f \times R \tag{2-37}$$

By introducing the model error, the new burst limit state function is presented by:

$$g(X) = P_f^* - MAP \tag{2-38}$$

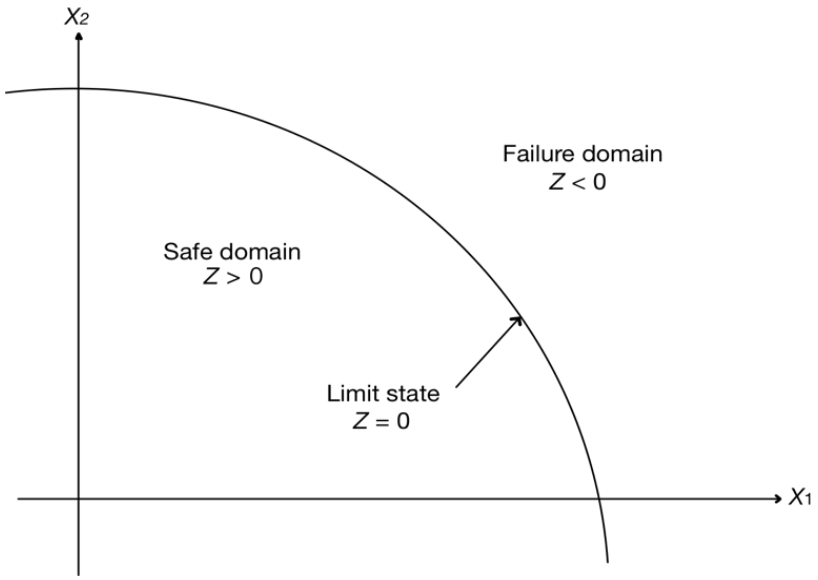

Figure 2-5: Illustration of limit state surface in 2-dimensional space

2.3.2 Monte Carlo Simulation

MCS, a stochastic sampling method, is based on statistical principles, i.e., Bernoulli's law and Chebyshev's law. As shown in Monte Carlo algorithm (**Figure 2-6**), the principle of MCS is to randomly generate a large number of sampled input basic variables in accordance with their respective probability distributions, perform the deterministic computation by substituting the generated variables in the LSF (Eq. (2-38)), and then count the numbers of the sample points falling into the failure domain ($g(X) \leq 0$), finally, the failure probability of the structure can be estimated as the ratio of the total number of cases where failure occurs (N_f) to the total number of performed simulations (N).

As mentioned previously, MCS has several attractive features such as it is simple and straightforward to implement, more accurate than other reliability assessment methods since there is no need to linearize the LSF, and capable of solving a wide range of reliability-related problems. Therefore, MCS method is employed in this work to estimate the likelihood of failure of oil and gas pipelines due to external surface cracks considering all the uncertainties associated with each parameter including the CorLAS^{TM} model error (**Appendix B**).

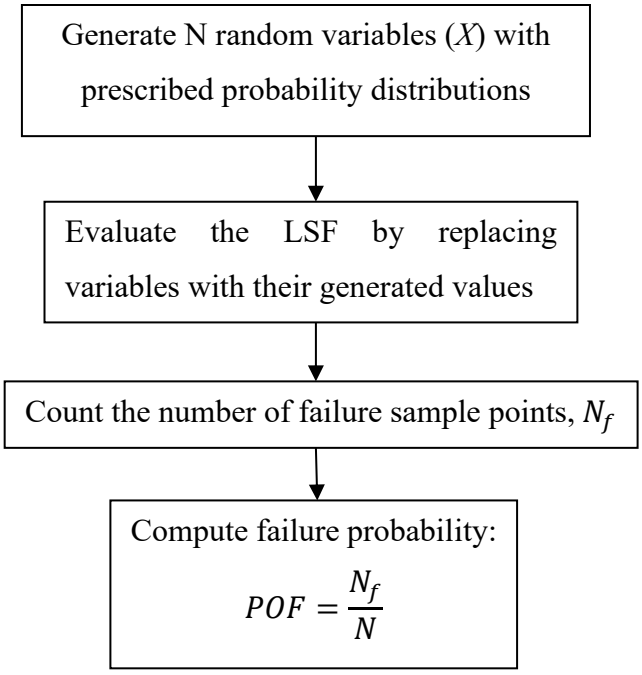

Figure 2-6: The PoF computation process by MCS

2.3.3 Sensitivity Analysis

To investigate the effects of several important parameters on PoF with respect to safety factor, the range of pipe properties considered in this study is as follows: The pipe grade varies from X42 to X80, the pipe diameter ranges from 711 mm to 1016 mm, and the wall thickness ranges between 8.74 mm to 25.4 mm. The distributions of RVs used in this study are summarized in **Table 2-1**.

Table 2-1: Random variable distributions

Variables	Distribution type	Mean	CoV (%)	Source
Pipe diameter/nominal pipe diameter	Normal	1.0	0.06	CSA Z662 Annex O [4]
Wall thickness/nominal wall thickness	Normal	1.01	1	
Yield strength/SMYS	Normal	1.1	3.6	
Tensile strength/SMTS	Normal	1.12	3.5	
Young's modulus, E	Normal	210	4	
MAP/MOP	Gumbel	1.03	1	
Model error, R_{tp}	Normal	1.07	14	Developed in this work

The PoFs are plotted against the safety factor for different parameters as shown in **Figure 2-7** and **Figure 2-8**. Overall, it indicates that the PoF decrease with the increase of the safety factor. This is reasonable, considering that the safety factor is defined as the capacity over the applied load. A margin of safety (M) is typically defined as capacity minus load and the failure probability is the probability P(M≤0). According to this definition, it is expected that an increase in the safety factor will imply a decrease in PoF due to the larger safety margin.

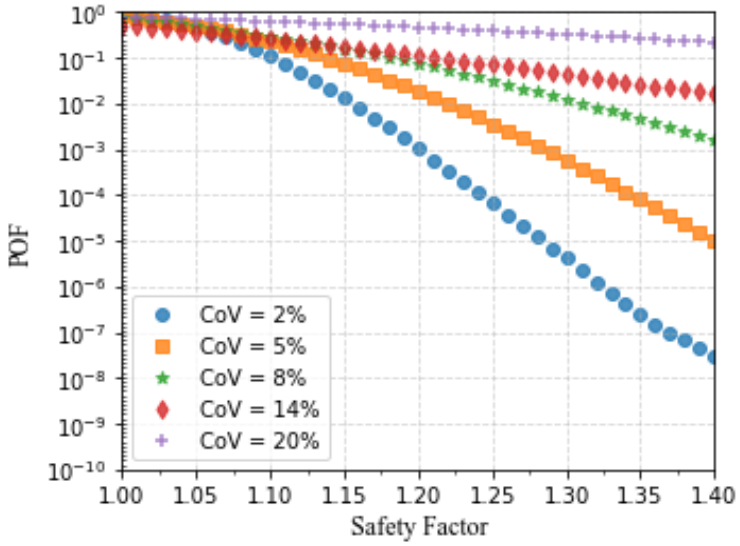

Figure 2-7: Model error CoV sensitivity

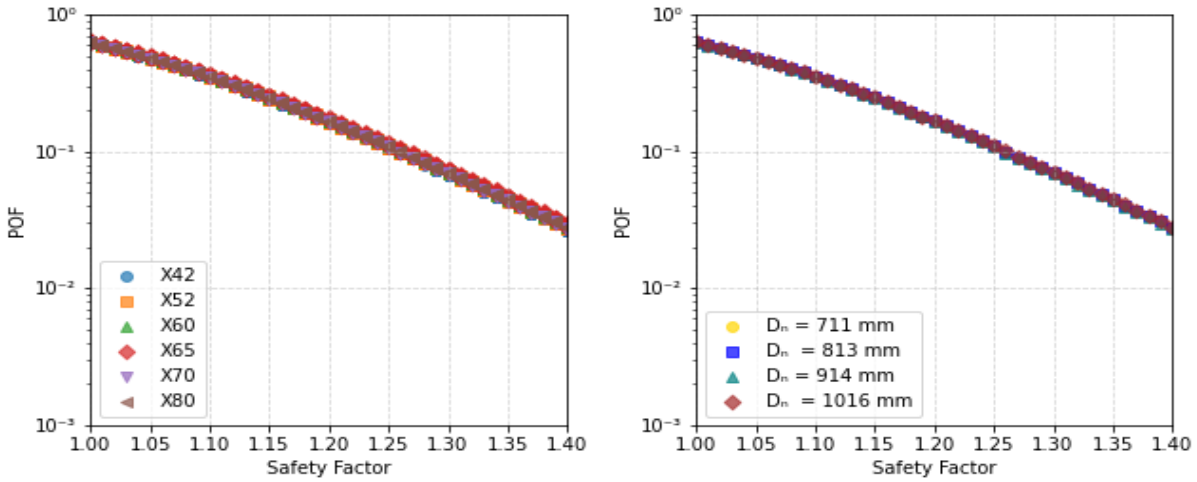

(a) (b)

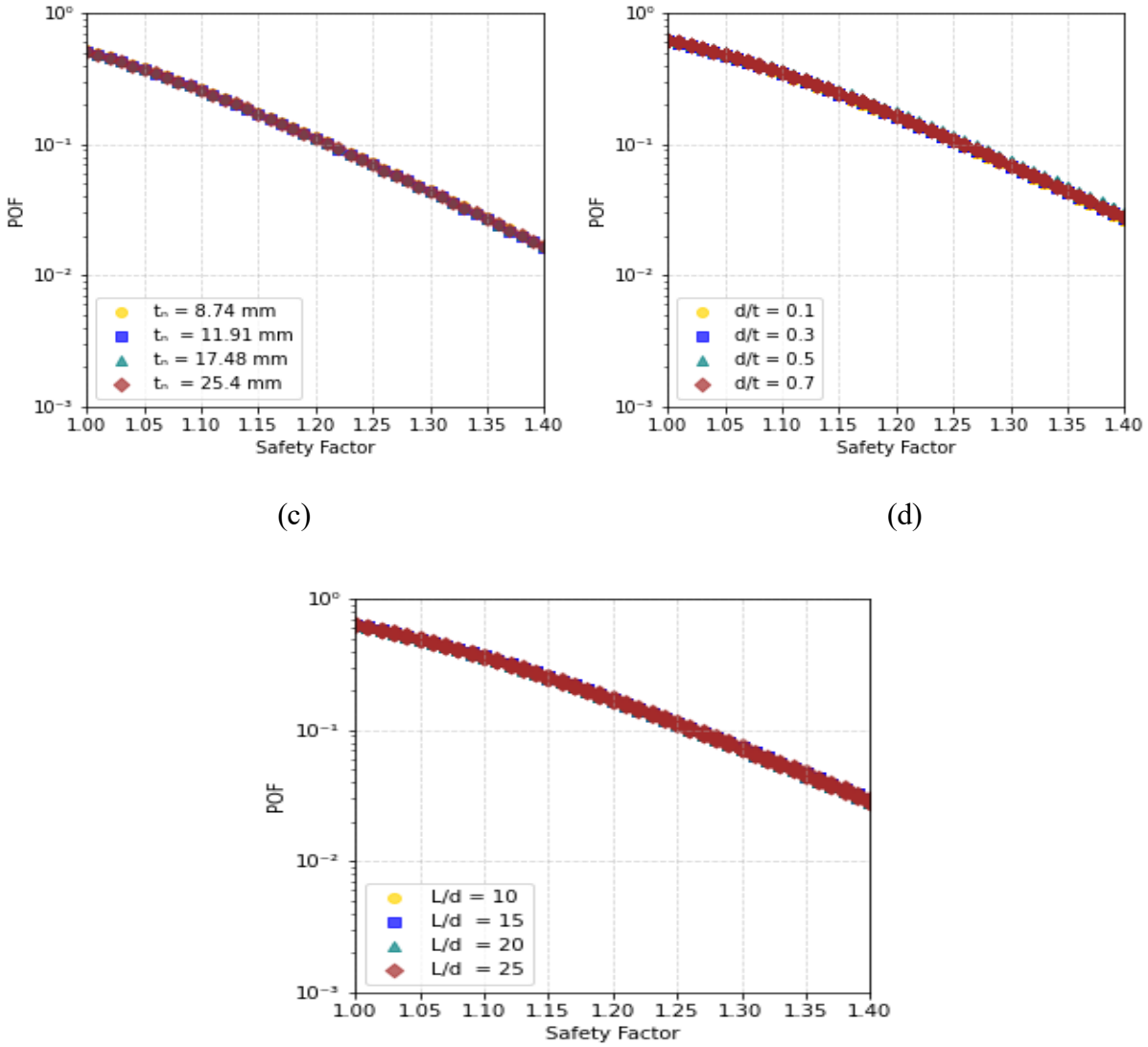

(c) (d)

(e)

Figure 2-8: PoF vs SF for different (a) pipe grades; (b) pipe diameters; (c) wall thickness; (d) crack depth-to-wall thickness ratio; (e) crack length-to-depth ratio

The effect of changing the model error CoV is demonstrated in **Figure 2-7**. A fixed model error mean value of 1.07 is used. As can be observed, the failure probability increases significantly with the increase of the model error CoV. The finding is supported by Ibrahim et al. [28] who investigated the model error CoV sensitivity by changing the CoV values from 1% to 25% using a fixed low mean value of 1.0. Their results show that a CoV value of 25% results in a significant increase in PoFs, where PoFs are estimated using FORM.

Figure 2-8 illustrates the correlation between PoF and the safety factor for different pipe grades, pipe dimensions (pipe diameter and wall thickness), the ratios of crack depth to wall thickness, and the ratios of crack length to depth. It is found that PoFs are not very sensitive to changing these factors. Similar findings are reported by Zheng et al. [26] who conducted a sensitivity study to analyze the effects of uncertainties on PoFs but without applying the model error associated with the CorLAS^{TM} model. It is interesting to note that the effects of pipe grade, pipe dimension, and crack size on the PoFs are negligible with and without considering the model error. The fact that PoF is not sensitive to the abovementioned factors is not surprising given the LSF in this study is defined as the predicted failure pressure minus MAP, which is correlated to the ratio of the predicted failure pressure to the safety factor. Therefore, the PoF is predominated by the safety factor, whereas the effects of the pipe dimensions and crack sizes on PoF are less significant.

Safety factor is an essential term in the field of buried pipeline design, thus, it is important to understand how it is calculated. By definition, safety factor is the ratio of the structural strength to the applied stress. Alternatively, safety factor can be expressed as the predicted failure pressure divided by the operating pressure, as shown in Eq. (2-36). It is apparent that safety factor varies with different input parameters. For example, the material strength can either be the value obtained by conducting material testing or the specified minimum yield strength (SMYS). Several material test reports have shown that the yield strength obtained from the material testing can be above SMYS [29]. The pipeline industry usually uses SMYS or lower-bound toughness to estimate the failure pressure. In addition, the crack dimensions (crack length and depth) can be treated probabilistically with statistical distributions derived from the tool tolerance; the uncertainty in the tool measurements of crack dimensions. In general, a safety factor of 1.25 using upper bounds of crack dimensions calculated using the tool tolerance is widely used by the pipeline industry as it is consistent with the API RP 1176 [29]. As described in API RP 1176 [29], prompt action is required by operators if the FPR (or safety factor) associated with a crack-like imperfection is less than 1.1. Besides, several scenarios could pose severe threats to pipeline integrity if the anomalies are left untreated, i.e., a scenario where a crack in-line inspection (ILI) indication with FPR less than 1.25. By contrast, in this study, although SMYS is used in the calculation of FPR, crack depth and length are treated deterministically at measured/reported values and the tool tolerance is not

taken into consideration. Therefore, the safety factor mentioned in this study cannot be directly compared to the FPR in API RP 1176 [29].

To better illustrate the difference between the safety factor defined in this study (denoted by SF_{CC}) and the one used by some pipeline operators (denoted by $SF_{industry}$), a comparison between the abovementioned SFs is presented. Assuming a standard 711.2 mm diameter API 5L X65 steel pipe with 9.525 mm wall thickness containing axially-oriented surface cracks whose dimensions of crack depth and length are 6.65 mm and 100 mm, respectively. The operating pressure is set to 6 MPa. According to the definition of SF_{CC}, the reported crack dimensions with an average toughness value (50.16 J) are used in Eq. (2-36). As previously stated, the calculation of $SF_{industry}$ is based on upper bounds of crack dimensions and lower-bound toughness. In order to achieve a high degree of accuracy in crack sizing, tool tolerance of 1.19 mm and 10.16 mm are added to crack depth and length as suggested in Willems and Hennig [30]. In this context, the crack depth and length are increased accordingly to 7.84 mm and 110.16 mm, whereas the toughness value is decreased to 36.6 J. As a result, the values of SF_{CC} and $SF_{industry}$ are 1.57 and 1.25, respectively.

Per DNV standard [31], the acceptable PoFs associated with three different safety classes for ULS are listed in **Table 2-2**.

Table 2-2: Target PoFs vs safety class for ULS

Safety class	**Target PoFs**
High	10^{-5}
Medium	10^{-4}
Low	10^{-3}

In order to achieve the target safety level for different safety classes, the results from **Figure 2-9** show that when using the CorLAS^{TM} model with the inclusion of the model error, safety factor of around 2 corresponds to high safety class, safety factor of 1.9 corresponds to medium safety class, and safety factor with a value of 1.6 corresponds to low safety class. It should be noted that this finding is limited to the LSF and choice of input parameters used here.

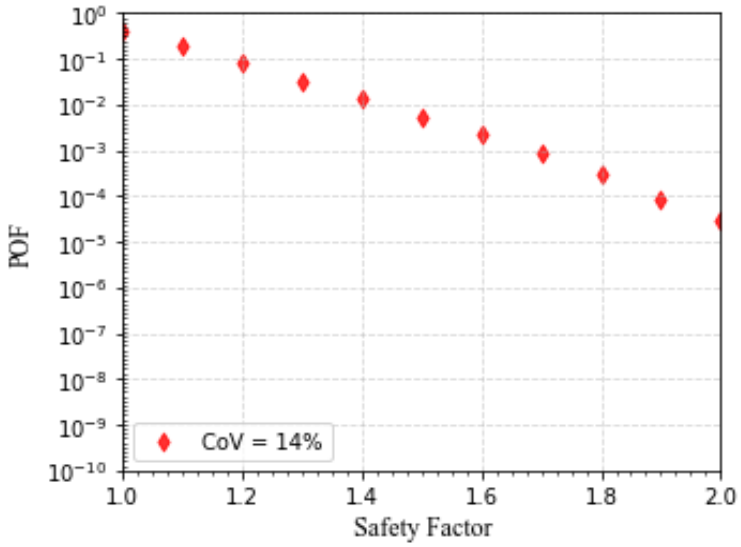

Figure 2-9: PoF vs safety factor with the inclusion of CorLAS^{TM}

2.4 Conclusions

The major accomplishments of this chapter are the evaluation of the model error distribution associated with CorLAS^{TM} Version 2 by using the collected 103 test data from the literature, the comparison of the accuracy between CorLAS^{TM} Version 1 and 2, and the investigation of the effects of input parameter uncertainties on PoFs incorporates the model error of CorLAS^{TM}, where PoFs are estimated using Monte Carlo simulation method. The following results are obtained:

(1) The modified CorLAS^{TM} model (Version 2) has similar accuracy to Version 1.

(2) After excluding the less reliable datasets, the mean and CoV of the test-to-prediction ratios for the CorLAS^{TM} model are 1.07 and 13.9%, respectively.

(3) PoF is independent of pipe grade, pipe dimension, and crack size, while it is a function of model error CoV and safety factor. To be more specific, the model error CoV is proportional to log (PoF) and safety factor is inversely proportional to log (PoF).

While this chapter contributes a study of the model error distribution associated with CorLAS^{TM} and reconciled the discrepancy between the two published studies by removing some subsets of the data, it still suffers some limitations. Namely, most input parameters such as crack dimensions are treated deterministically rather than probabilistically.

References

[1] Zhang, X., Lin, M., Okodi, A., Tan, L., Leung, J.Y. and Adeeb, S. Numerical analysis of API X42 and X52 vintage pipes with cracks in corrosion defects using extended finite element method. *Journal of Pressure Vessel Technology*, 143(6):061302, 2021.

[2] Bichon, B.J., Eldred, M.S., Swiler, L.P., Mahadevan, S. and McFarland, J.M. Multimodal reliability assessment for complex engineering applications using efficient global optimization. AIAA Paper No. AIAA-2007-1946, 2007.

[3] Cosham, A., Hopkins, P. and Leis, B. Crack-like defects in pipelines: the relevance of pipeline-specific methods and standards. Paper No. IPC2012-90459, *Proceedings of the 2012 9th International Pipeline Conference, American Society of Mechanical Engineers,* Calgary, Canada, 2012.

[4] CSA. Oil and gas pipeline systems. CSA Standard Z662:19, Canada Standards Association, Mississauga, Ontario, Canada, 2019.

[5] Yan, Z., Zhang, S. and Zhou, W. Model error assessment of burst capacity models for energy pipelines containing surface cracks. *International Journal of Pressure Vessels and Piping*, 120-121: pp. 80-92, 2014.

[6] Yan, J., Zhang, S., Kariyawasam, S., Pino, M. and Liu, T. Validate crack assessment models with in-service and hydrotest failures. Paper No. IPC2018-78251, *Proceedings of the 2018 12th International Pipeline Conference, American Society of Mechanical Engineers*, Calgary, Canada, 2018.

[7] Jaske, C.E., Beavers, J.A. and Harle, B.A. Effect of stress corrosion cracking on integrity and remaining life of natural gas pipelines. Paper No. 255, Corrosion 96, NACE International, Houston, 1996.

[8] Jaske, C.E., Polasik, S.J. and Maier, C.J. Inelastic fracture mechanics model for assessment of crack-like flaws. Paper No. PVP2011-57099, *Proceedings of the Pressure Vessels & Piping Conference, American Society of Mechanical Engineers,* Baltimore, Maryland, USA, 2011.

[9] Kiefner, J.F., Maxey, W.A., Eiber, R.J. and Duffy, A.R. Failure stress levels of flaws in pressurized cylinders. Progress in flaw growth and fracture toughness testing, STP 536, *ASTM International*, West Conshohocken, PA, pp. 461-481, 1973.

[10] Wilkowski, G.M., Ahmad, J., et al. Degraded piping program: Phase II, Semiannual report, April 1986 – September 1986, NUREG/CR-4082, Volume 5, 1987.

[11] Jaske, C. E. and Beavers, J. A. Integrity and Remaining Life of Pipe with Stress Corrosion Cracking. PRCI 186-9709, Catalog No. L51928. Pipeline Research Council International, Falls church, 2001.

[12] Irwin, G.R. The crack extension force for a part-through crack in a plate. *Journal of Applied Mechanics*, 30(3), 651-654, 1963.

[13] Broek, D. Elementary engineering fracture mechanics, 3rd edition. Martinus Nijhoff Publishers, The Hague, 1982.

[14] Paris, P.C and Sih, G.C. Stress analysis of cracks. ASTM STP 381, pp, 30-81, 1965.

[15] Kobayashi, A. S., Ziv, M. and Hall, L. R. Approximate stress intensity factor for an embedded elliptical crack near to parallel free surfaces. *International Journal of Fracture Mechanics 1*, pp.81-95, 1965.

[16] Jaske, C. E. and Beavers, J.A. Review and proposed improvement of a failure model for SCC of pipelines. Paper No. IPC1998-2051, *Proceedings of the 1998 2nd International Pipeline Conference, American Society of Mechanical Engineers,* Calgary, Canada, 1998.

[17] Jaske, C. E. and Beavers, J.A. Development and evaluation of improved model for engineering critical assessment of pipelines. Paper No. IPC2002-27027, *Proceedings of 4th International Pipeline Conference, American Society of Mechanical Engineers,* Calgary, Canada, 2002.

[18] Staat, M. Plastic collapse analysis of longitudinally flawed pipes and vessels, *Nuclear Engineering and Design*, 234(1-3), 25-43, 2004.

[19] Cravero, S. and Ruggieri, C. Structural integrity analysis of axially cracked pipelines using conventional and constraint-modified failure assessment diagrams, *International Journal of Pressure Vessel and Piping*, 83(8), 607-17, 2006.

[20] Demofonti, G., Mannucci, G., Barsanti, L., Spinelli, C.M. and Hillenbrand, H.G. Fracture behaviour and defect evaluation of large diameter, HSLA steels, very high pressure linepipes. Paper No. IPC2000-168, *Proceedings of the 2000 3rd International Pipeline Conference, American Society of Mechanical Engineers,* Calgary, Canada, 2000.

[21] Hosseini, A., Cronin, D., Plumtree, A. and Kania, R. Experimental testing and evaluation of crack defects in line pipe. Paper No. IPC2010-31158, *Proceedings of the 2010 8th International Pipeline Conference, American Society of Mechanical Engineers*, Calgary, Canada, 2010.

[22] Keller, H.P., Junker, G. and Merker, W. Fracture analysis of surface cracks in cylindrical pressure vessels applying the two parameter fracture criterion (TPFC). *International Journal Pressure Vessels and Piping*, 29(2), 113-153, 1987.

[23] Rothwell, A.B. and Coote, R.I. A critical review of assessment methods for axial planar surface flaws in pipe. *Proceedings of the International Conference on Pipeline Technology*, Ostend, Belgium, 2009.

[24] Wang, K.C. and Smith, E.D. The effect of mechanical damage on fracture initiation in linepipe: part II e gouges. Canadian Centre for Mineral and Energy Technology (CANMET); 1988. Report ERP/PMRL 88e16 (TR), Canada.

[25] Garwood, S.J., Willoughby, A.A. and Rietjens, P. The application of CTOD methods for safety assessment in ductile pipeline steels. In: International Conference on Fitness for Purpose Validation of Welded Constructions, London, UK; 1981.

[26] Zheng, Q., Abdelmoety, A.K., Li, Y., Kainat, M., Yoosef-Ghodsi, N. and Adeeb, S. Reliability analysis of intact and defected pipes for internal pressure related limit states specified in CSA Z622:19. *International Journal of Pressure Vessels and Piping*, 192(2021) 104411.

[27] Smart, L.J. Review of materials property data for nondestructive characterization of pipeline materials. MSc Thesis, Iowa State University, 2015.

[28] Ibrahim, M., Doucette, K., Hassanien, S. and Langer, D. Effect of model error on reliability analysis of surface cracks. Paper No. IPC2018-78237, *Proceedings of the 2018 12th International Pipeline Conference, American Society of Mechanical Engineers*, Calgary, Canada, 2018.

[29] API RP 1176. Recommended practice for assessment and management of cracking in pipelines. API Publishing, Errata 1, 2021.

[30] Willems, H. and Hennig, T. Recent improvements regarding ultrasonic crack inspection of pipelines. Pigging Products & Services Association, NDT Global, 2017.

[31] Det Norske Veritas (DNV). Submarine Pipeline Systems: Offshore standard DNV-OS-F101, 2012.

CHAPTER 3: INFLUENCE OF STRAIN HARDENING MODEL ON THE CORLAS^{TM} MODEL FOR CRACKED PIPELINES

This chapter is derived from the published conference proceeding:

Zhang, X., Lin, M., Kainat, M., Yoosef-Ghodsi, N., Leung, J. and Adeeb, S., Influence of Strain Hardening Model on the CorLAS^{TM} model for Cracked Pipelines, Proceedings of the ASME 2022 International Pipeline Conference, September 26-30, 2022, Calgary, Alberta, Canada, Paper No. IPC2022-86856, doi: 10.1115/IPC2022-86856.

Abstract

Underground steel pipelines may experience failure due to the occurrence of cracks or crack-like anomalies as a result of internal and external factors such as manufacturing imperfection and geotechnical movement. Metallic materials like steel often undergo strain hardening as deformation increases. The strain hardening characteristics of materials are usually described by strain hardening models. Accurate approximations of the stress-strain curves are essential for numerical simulations. For pipelines containing axially-oriented cracks, a software-based model often referred to as CorLAS^{TM} is widely accepted and commonly used by the pipeline industry to estimate the failure pressures. In CorLAS^{TM}, the stress-strain behavior of pipeline steel is modelled based on a simple power-law relationship known as the Hollomon equation. However, the Hollomon model cannot characterize the full-range strain hardening behavior of metallic materials, which is an approximation by design. Additionally, the strain-hardening exponent, n, in the CorLAS^{TM} model is estimated based on an expression using yield strength and ultimate tensile strength. By contrast, the n value in mathematical models such as the Ramberg-Osgood equation, Swift equation, Ludwik equation, Ludwigson equation can be evaluated by using curve-fitting regression techniques, i.e., fitting the experimental true stress versus true strain data to the empirical models. This paper reviews the most frequently used strain hardening formulas and explores the applicability and accuracy of these stress-strain models including the hardening exponent expression in CorLAS^{TM} (Version 2). This is followed by a sensitivity study to investigate the effect of n on the failure pressure predicted by CorLAS^{TM}. The holistic accuracy of CorLAS in predicting burst pressure, compared to other widely accepted models, is not explored.

Keywords: Strain hardening exponent, true stress, true strain, CorLAS^{TM}, pipelines.

NOMENCLATURE

α	Ramberg-Osgood material constant
σ	true stress
σ_{eng}	engineering stress
σ_{UTS}	ultimate tensile stress
σ_{YS}, σ_0	yield stress

ε	true strain
ε_e	elastic strain
ε_{eng}	engineering strain
ε_p	true plastic strain
ε_{Py}	true plastic strain at yield
ε_0	yield strain
E	Young's modulus
K	strength coefficient
n	strain hardening exponent
Δ	Ludwigson correction term

3.1 Introduction

Pipelines, the safest and most economical mode to transport natural gas and crude oil, often experience plastic deformation while passing through some geologically unstable areas [1]. From a micro point of view, pipeline steels can undergo strain hardening as the strain deformation increases. The strain hardening behavior of metallic materials can be characterized using a true stress-true strain curve [2], also known as the flow curve, which can be generally divided into two distinct regions: the before and after necking parts (as illustrated in **Figure 3-1** [3]). Before the onset of necking, Eqs. (3-1) and (3-2) are used to convert true stress-strain values from the engineering stress-strain values obtained from standard tensile tests.

$$\varepsilon = \ln(1 + \varepsilon_{eng}) \tag{3-1}$$

$$\sigma = \sigma_{eng}(1 + \varepsilon_{eng}) \tag{3-2}$$

where ε, ε_{eng}, σ, and σ_{eng} are, respectively, true strain, engineering strain, true stress, and engineering (or the so-called "nominal") stress.

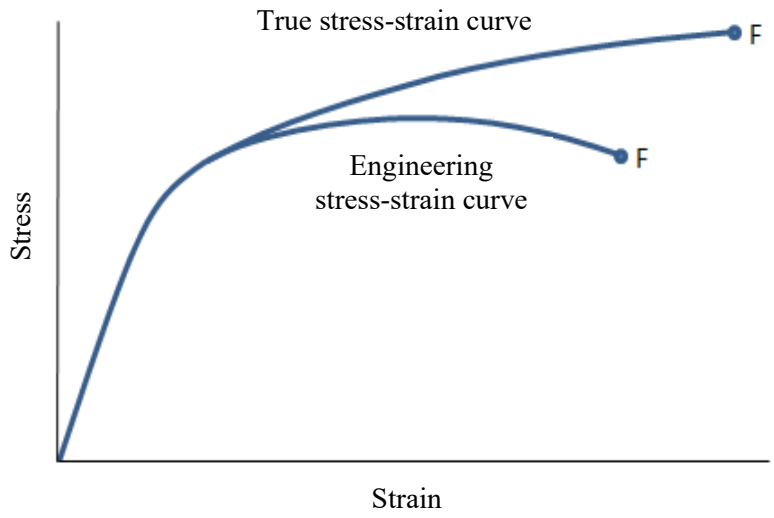

Figure 3-1: Comparison of true and engineering stress-strain curves, adapted from [3]

After the ductile material exhibits necking, Eqs. (3-1) and (3-2) are not suitable for calculating the true stress and true strain as the specimen geometry changes, while the equations assume that specimens are uniformly deformed [4]. Beyond the necking point, the true stress and true strain are determined from the instantaneously measured load and cross-sectional area, which requires accurate measurement systems to get accurate records [3]. In practice, it is preferred to represent the plastic flow behavior of metallic materials using simplified mathematical expressions instead of conducting tensile tests to retrieve the test data, which can be costly and time consuming [5].

For this purpose, a number of empirical and/or mathematical equations have been developed by numerous investigators over the past few decades to model the strain hardening behavior of metallic materials. For instance, the power-law form relationships, i.e., the Ludwik [6], Ramberg-Osgood [7], Hollomon [8], Swift [9], and Ludwigson [10] equations. It may be of interest to note that these empirical equations are based on an expression of true stress as a power function of true plastic strain, which is calculated by subtracting the elastic strain from true total strain, where the elastic strain is defined as true stress over the Young's modulus ($\frac{\sigma}{\mathrm{E}}$) according to Hooke's law.

The above-stated empirical equations usually contain two unknown model parameters: strain hardening exponent and strength coefficient. Strain hardening exponent, or strain hardening index, denoted by n, is a dimensionless and unitless parameter. The higher the n value, the better stretch

formability of a material [11]. Strength coefficient, also known as the strain hardening coefficient, denoted by K, with a unit of Pascal which is the same unit as stress and is equivalent to the true stress at $\varepsilon = 1$.

Traditionally, there are two methods to determine the unknown K and n: One method is linear regression (LR) by linearizing the constitutive equation and convert it into the form of $y = mx + b$, then the fitting parameters can be found through plotting experimental data in a log-log curve. The other method is called curve-fitting using non-linear regression (NR), which is fitting the experimental data to the non-linear stress-strain models, and the constitutive model parameters can thus be obtained by minimizing the sum of the squares of the error between the actual curve and the mathematical model (also termed as "least square method"). However, in the cases where multiple sets of test data are unavailable, alternatively, mathematical expressions can be used to estimate the K and n with the premise of knowing only the tensile properties, like the one adopted in the CorLAS^{TM} model, which will be discussed in more details in the upcoming section.

Through a comprehensive literature review, most researchers evaluate the fitting parameters by linearizing the constitutive relationship. Meanwhile, limited attention was given to the NR analysis. Hence, this paper aims to compare the accuracy between the LR and NR analysis, in terms of describing the actual stress-strain curve.

This chapter is organized into different sections. The theoretical background of five commonly used strain hardening equations and the computational methods of fitting parameters for these constitutive equations are chronologically presented in **Section 3.2**. In **Section 3.3**, a comparison of the flow curves described by these equations where the fitting parameters are obtained through linearization of the constitutive relation and NR analysis, an investigation of the accuracy of these stress-strain models, including CorLAS^{TM} model explicitly, and a sensitivity study regarding the effects of the strain hardening exponent on the failure pressure predicted by CorLAS^{TM} model and the stress-strain diagram are carried out. Finally, principal conclusions and recommendations can be found in **Section 3.4**.

3.2 Strain Hardening Exponent

3.2.1 Ludwik Model

The Ludwik equation [6], developed in 1909, is the oldest among the aforementioned fundamental stress-strain models. In the Ludwik equation, a power law relation between true stress and true plastic strain is assumed in the form of:

$$\sigma = \sigma_0 + K_L \varepsilon_p^{n_L} \tag{3-3}$$

where σ denotes the true stress, σ_0 is the yield stress, ε_P is the true plastic strain, K_L is referred to as the strength coefficient, and n_L is the strain hardening exponent for the Ludwik equation.

In 1950, Crussard and Jaoul [12] proposed a method, so-called differential Crussard-Jaoul ($\mathrm{D_{C-J}}$) analysis, to evaluate the material constants (K_L and n_L) in the Ludwik equation by first differentiating Eq. (3-3) with respect to ε_P, expressed as:

$$\frac{d\sigma}{d\varepsilon_p} = K_L n_L \varepsilon_p^{n_L - 1} \tag{3-4}$$

The logarithmic form of Eq. (3-4) is expressed as:

$$\log\left(\frac{d\sigma}{d\varepsilon_p}\right) = \log(K_L n_L) + (n_L - 1)\log\left(\varepsilon_P\right) \tag{3-5}$$

As can be seen in Eq. (3-5), the equation yields a straight line of the form $y = mx + b$, the slope of the resulting straight line $m = n_L - 1$, while its intersection with Y-axis ($\log(\varepsilon_P) = 0$) gives $b = \log(K_L n_L)$ so that K_L and n_L can be determined.

However, Liessem [13] noted that the inclusion of the yield strength is inconvenient and that there is a substantial deviation between the power-law curve and the stress-strain diagram, which may lead to inaccurate representations.

3.2.2 Ramberg-Osgood Model

It is important to notice that the linear-elastic portion of the stress-strain curve is not considered in the Ludwik equation. About four decades later, Ramberg and Osgood [7] proposed a non-linear relationship which accounts for the linear elastic branch of the stress-strain diagram

to better model the strain hardening behavior of the material. A general form of the Ramberg-Osgood equation (ROE) in terms of three parameters is given as:

$$\varepsilon = \frac{\sigma}{E} + K_{RO} \cdot (\frac{\sigma}{E})^{n_{RO}} \tag{3-6}$$

Therein, ε denotes the true strain, E stands for the Young's modulus (or modulus of elasticity), K_{RO} and n_{RO} are the strength coefficient and strain-hardening exponent in the ROE. The initial term on the right side, $\frac{\sigma}{E}$, equals to the elastic strain (ε_e), signifies the linear behavior, while the second term represents the non-linear behavior. Originally, the ROE was designed for aluminum alloys but then extended to non-linear metals such as stainless steels [14].

Similar to Ludwik's equation, K_{RO} and n_{RO} are often determined from the intercept and slope of the plastic strain versus true stress curve, plotted on a logarithmic scale [7]. Log-log plot produces a straight line from which the coefficients can be found.

$$\log(\varepsilon_P) = n_{RO} \cdot \log(\frac{\sigma}{E}) + \log(K_{RO}) \tag{3-7}$$

In 1944, Hill [15] proposed an alternative ROE by introducing the yield strength of the material (σ_{YS}) and a dimensionless parameter (α), (See Zhang et al. [16]), whose expression is given by:

$$\varepsilon = \frac{\sigma}{E} + \alpha \frac{\sigma_{YS}}{E} (\frac{\sigma}{\sigma_{YS}})^{n_{RO}} \tag{3-8}$$

where,

$$\alpha = K_{RO} \left(\frac{\sigma_{YS}}{E}\right)^{n_{RO}-1} \tag{3-9}$$

As σ_{YS} is generally determined by 0.2% offset method, meaning that $\alpha \frac{\sigma_{YS}}{E} = 0.002$, thus, Eq. (3-8) can be further stated as:

$$\varepsilon = \frac{\sigma}{E} + 0.002(\frac{\sigma}{\sigma_{YS}})^{n_{RO}} \tag{3-10}$$

In 2007, API579-1/ASME FFS-1 [17] proposed the following slight modification to the ROE (See Zhang et al. [18]):

$$\varepsilon = \frac{\sigma}{\mathrm{E}} + \left(\frac{\sigma}{H_{\mathrm{RO}}}\right)^{\frac{1}{n_{\mathrm{RO}}}} \tag{3-11}$$

Ideally, the fitting parameters (H_{RO} and n_{RO}) could be derived through regression analysis if multiple sets of true stress-strain data are available. Otherwise, the fitting constants can be computed based on mathematical expressions using known tensile properties [17], i.e., σ_{YS} and ultimate tensile stress (σ_{UTS}).

$$n_{\mathrm{RO}} = \frac{1+1.3495\left(\frac{\sigma_{YS}}{\sigma_{UTS}}\right)-5.3117\left(\frac{\sigma_{YS}}{\sigma_{UTS}}\right)^2+2.9643\left(\frac{\sigma_{YS}}{\sigma_{UTS}}\right)^3}{1.1249+11.0097\left(\frac{\sigma_{YS}}{\sigma_{UTS}}\right)-11.7464\left(\frac{\sigma_{YS}}{\sigma_{UTS}}\right)^2} \tag{3-12}$$

$$H_{\mathrm{RO}} = \frac{\sigma_{UTS}\exp(n_{RO})}{{n_{RO}}^{n_{RO}}} \tag{3-13}$$

3.2.3 Hollomon Model

In 1945, Hollomon [8] proposed a simpler equation by waiving the parameter σ_0 from the Ludwik equation. In the equation, the true plastic strain (ε_P) is related to stress (σ) by a power-law relationship:

$$\sigma = K_H \varepsilon_p^{n_H} \tag{3-14}$$

Herein, K_H is the strength coefficient and n_H is the strain-hardening exponent in the Hollomon relationship.

By taking the logarithm of both sides in Eq. (3-14), the equation is expressed as:

$$\log(\sigma) = n_H \cdot \log(\varepsilon_P) + \log(K_H) \tag{3-15}$$

According to this equation, the values of K_H and n_H can be easily obtained from the linear fitting of Eq. (3-15) (refer to as 'Hollomon analysis'). The slope of the straight-line equals n_H and its intersection with $\log(\varepsilon_P) = 0$ ($\varepsilon_P = 1$) gives $\log(K_H)$.

Unlike the Ludwik equation, the Hollomon equation implies that strain hardening begins at the very start of the tensile test (zero plastic strain, zero stress). However, some researchers consider that the onset of the strain hardening is at the yield point and continues up and beyond the ultimate tensile point [19]. Moreover, the Hollomon equation is described as being too simplistic to model the entire range of the stress-strain curve since the equation only has two parameters [20].

3.2.4 Swift Model

Swift [9] proposed a modification to the Hollomon equation in 1952, by introducing a constant into the strain term to account for the possible pre-strain left in the material, which is perceived to be a more successful power-law formula, the relationship between stress and strain can be expressed in follows:

$$\sigma = K_S(\varepsilon_0 + \varepsilon_p)^{n_S} \tag{3-16}$$

where ε_0 denotes the initial yield strain which represents the amount of pre-strain in the material (residual strain, might be left over from the cold forming). K_S and n_S are, respectively, the Swift strength coefficient and Swift strain hardening exponent.

Modified Crussard and Jaoul analysis [21] is used to determine the fitting parameters (K_S and n_S) in the Swift equation. Likewise, Eq. (3-16) is first differentiated with respect to ε_p to give:

$$\frac{d\sigma}{d\varepsilon_p} = \frac{n_S K_S^{\frac{1}{n_S}}}{\sigma^{\frac{1}{n_S}-1}} \tag{3-17}$$

By applying the logarithm operator to both sides of Eq. (3-17):

$$\log\left(\frac{d\sigma}{d\varepsilon_p}\right) = \log\left(n_S K_S^{\frac{1}{n_S}}\right) + (1 - \frac{1}{n_S})\log(\sigma) \tag{3-18}$$

Therefore, the plot of $\log\left(\frac{d\sigma}{d\varepsilon_p}\right)$ versus $\log(\sigma)$ would result in a straight-line from which K_S and n_S can be determined.

3.2.5 Ludwigson Model

As stated previously, the Hollomon equation is found to be inadequate to model the plastic flow behavior of materials, especially at low strain levels. To improve the approximation, Ludwigson [10] adjusted the Hollomon equation in 1971 by adding a second term which is

intended to address the discrepancy between the experimental stress data and that estimated by the Hollomon relationship at low strains, in the form of:

$$\sigma = K_1 \varepsilon_p^{n_1} + \Delta \tag{3-19}$$

where Δ accounts for the stress deviation and is defined as:

$$\Delta = \exp\left(K_2 + n_2 \varepsilon_P\right) \tag{3-20}$$

K_1 and n_1 are the strength coefficient and strain hardening exponent as in the Hollomon equation. K_2 and n_2 are two additional dimensionless coefficients.

It can be seen from **Figure 3-2** that the stress calculated by the ideal Hollomon equation (red curve) deviates from the actual stress data (black curve). As evident in Figure 3-2, the ε_P vs σ curve is nearly linear at the high strain levels, thus, K_1 and n_1 can be obtained through linear regression by considering the data only at high strain region.

$$\ln\left(\Delta\right) = K_2 + n_2 \varepsilon_P \tag{3-21}$$

According to Eq. (3-21), K_2 and n_2 can be determined from a plot of ε_P - lnΔ, where n_2 is the slope and K_2 is the intercept at $\varepsilon_P = 0$. It is noteworthy that the value of n_2 is always negative, but the exponential term (Δ) can either be positive or negative [5].

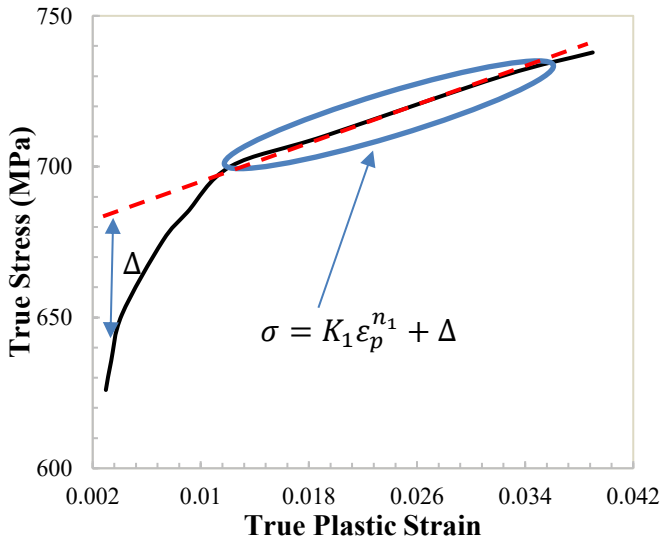

Figure 3-2: Illustration of the stress deviation using the Hollomon equation, adapted from [22]

3.2.6 CorLAS^{TM} Model

In 1996, Jaske and Beaver [23] proposed a software-based model, known as CorLAS^{TM}, to evaluate the failure pressure associated with axially-cracked pipelines. Two failure criteria are adopted in the model, namely, flow-strength and fracture-toughness based failure criteria. Whichever criterion gives the least failure pressure is selected to estimate the final failure pressure [24]. In the latter criterion, the failure stress (σ) is determined when the J integral (J_t) reaches the critical J through iteratively calculating the J integral. It is important to state that the computation of the plastic component of J integral (J_p) requires characterizing the strain hardening behavior of the materials, as shown in Eq. (3-24).

$$J_p = Q_f F_{sf} a f_3(n) \varepsilon_p \, \sigma \tag{3-24}$$

where $Q_f, F_{sf}, a, f_3(n)$ are, respectively, the elliptical shape factor, free-surface factor, crack depth, and a dimensionless factor depends on the strain hardening exponent. The plastic strain (ε_P) is computed from stress using the simple Hollomon power-law relationship as follows:

$$\varepsilon_P = K_C \sigma^{n_C} \tag{3-25}$$

K_C and n_C are the strength coefficient and strain hardening exponent in the CorLAS^{TM} model. Since the published *n* values may not be available for all pipe grades [25], in this case, it is fairly straightforward to approximate the parameters using an expression based on known material properties. In general, 0.2% offset method is chosen to determine the yield strength. However, for API pipeline steels, yield strength defined as the stress corresponding to a total strain of 0.5% (0.5% strain method) is more preferred [26]. The expression for the plastic strain at yield (ε_{Py}) is given by:

$$\varepsilon_{Py} = \varepsilon - \varepsilon_e = 0.005 - \frac{\sigma_{YS}}{E} \tag{3-26}$$

As shown in the Eqs. (3-27) and (3-28), yield strength is used to compute K_C, whereas n_C is estimated using the ratio of yield strength and ultimate tensile strength. It is of interest to note that Eq. (3-28) was developed by curve-fitting data (API X42, X52, X70, and X80 steels) obtained from past studies. Due to the limited data, Jaske et al. [25] found that X42 data did not fit well to the curve, as the data point fell lower than expected. In fact, the authors acknowledged in their original article [25] that additional test data could be leveraged to further revise the Eq. (3-28).

$$K_C = \frac{0.005 - \frac{\sigma_{YS}}{E}}{{\sigma_{YS}}^{n_C}} \tag{3-27}$$

$$n_C = -0.00546 + 0.556\frac{\sigma_{YS}}{\sigma_{UTS}} - 0.547\left(\frac{\sigma_{YS}}{\sigma_{UTS}}\right)^2 \tag{3-28}$$

3.3 Results and Discussion

3.3.1 Comparison of the Stress-strain Curves Generated Through NR and LR

Five constitutive equations, namely, the Ludwik, Ramberg-Osgood, Hollomon, Swift, and Ludwigson equations, are evaluated in this section using experimental stress-strain data obtained at the University of Alberta. Specifically, three tension specimens (1A, 1B, and 1C) machined from the base metal of X52 steel pipe in the longitudinal orientation were tested by Lin [27] and a total of five tension tests were performed by Fathi [28] on longitudinal round-bar (LR) and strap (LS) coupon specimens for X80 steel pipes. It should be noted that the average stress-strain curves were treated as the representative curves for the subsequent studies, as shown in **Figure 3-3**. Apparently, a significant difference is seen in the X52 and X80 flow curves. The X80 steel pipe has a relatively flat curve with the yield stress-to-tensile stress ratio (Y/T) equal to 0.71 in comparison to the X52 curve with the Y/T ratio of 0.81, meaning that the presented specimens represent two families of steels. Therefore, it is expected that the obtained n values would be different given the difference between the curves for these grades. The fitting parameters (K and n) for the abovementioned formulas are derived successively through linear and non-linear regression analysis.

As described earlier in **Section 3.2**, the two fitting constants can be determined through LR analysis by plotting the actual stress-strain data before necking on a double logarithmic curve using TREND function in Excel. Therefore, all the five mentioned models are first evaluated using the LR; detailed descriptions of how to analyse the fitting constants for each model are shown in **Figure 3-4** and **Figure 3-5** for grades X52 and X80, respectively. When conducting the NR analysis, Python function (scipy.optimize.curve_fit) is used to fit the test data to the Ludwik, Hollomon, Swift, and Ludwigson models, while the online code through MecSimCalc [29] is used to obtain the fitting parameters for the Ramberg-Osgood model (Interested readers can find it at: https://www.mecsimcalc.com/app/4568297/stress_strain_curve_of_steel_materials_table) by simply inputting eight representative true stress-strain data points.

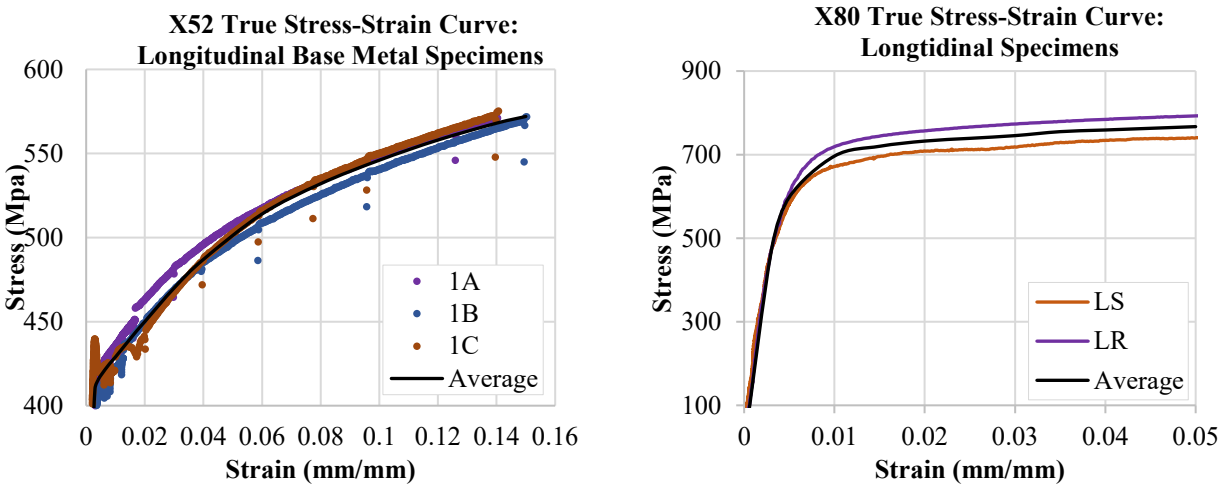

Figure 3-3: Average true stress-strain curves for X52 and X80 pipe grades

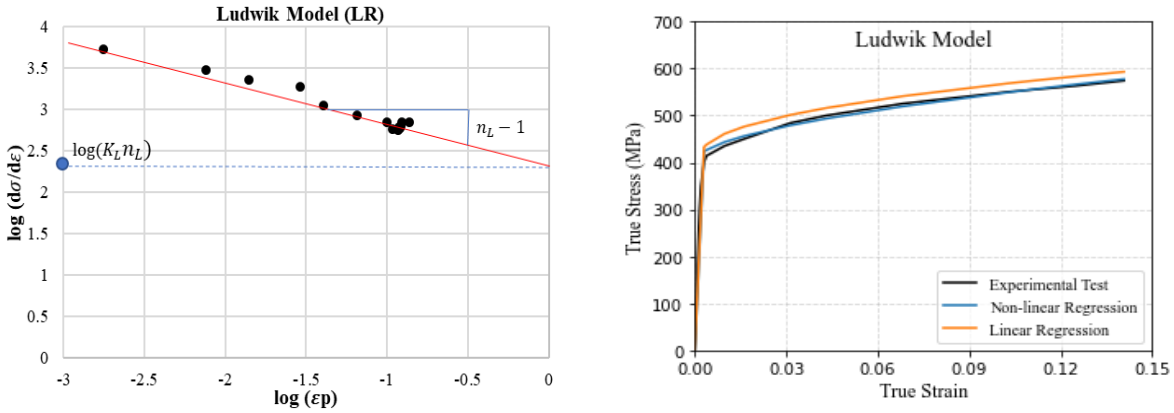

(a)

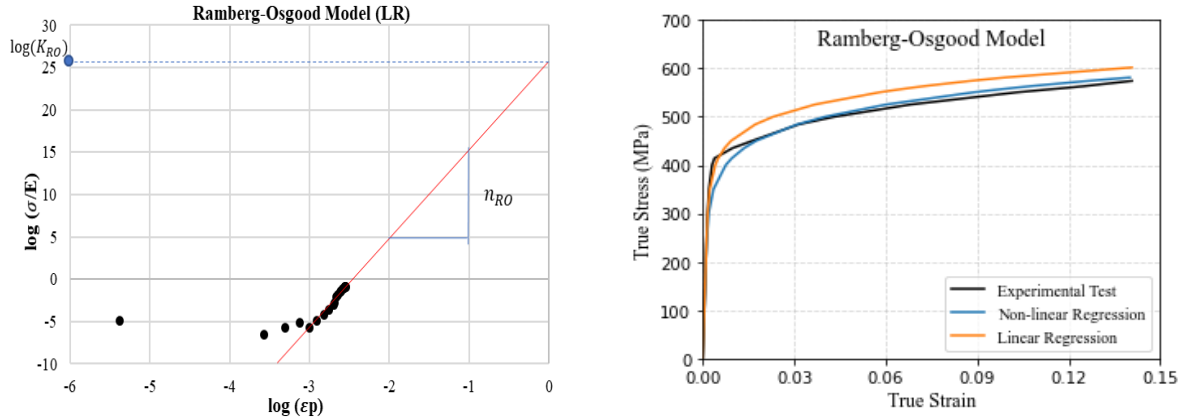

(b)

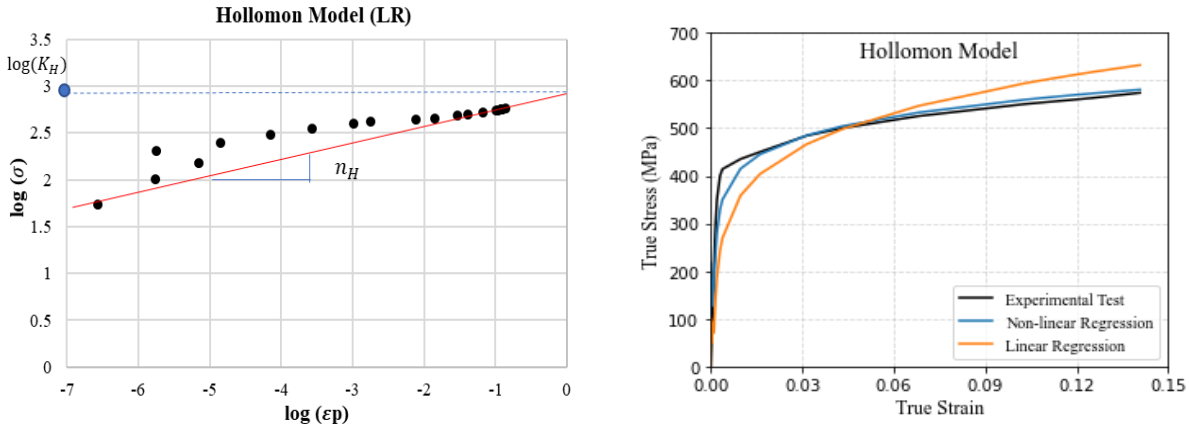

(c)

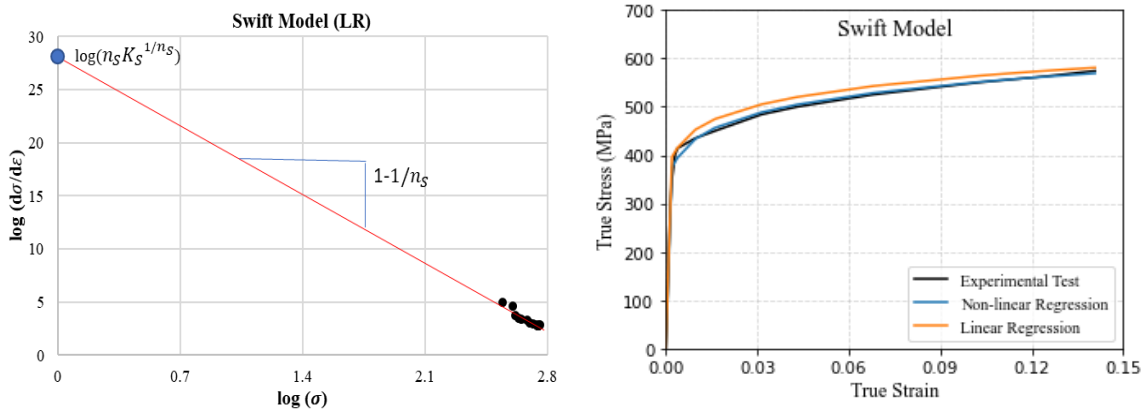

(d)

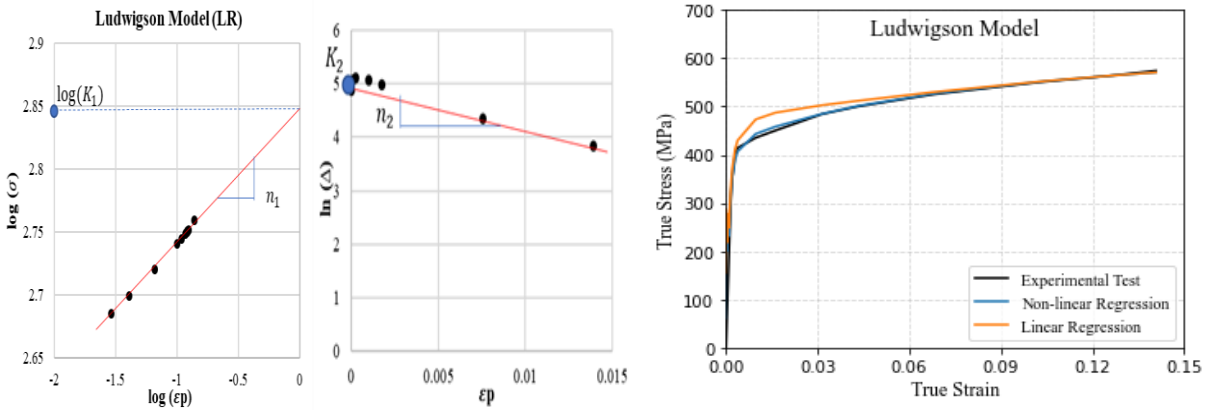

(e)

Figure 3-4: Flow curves for X52 grade generated by non-linear and linear regression techniques based on five empirical models

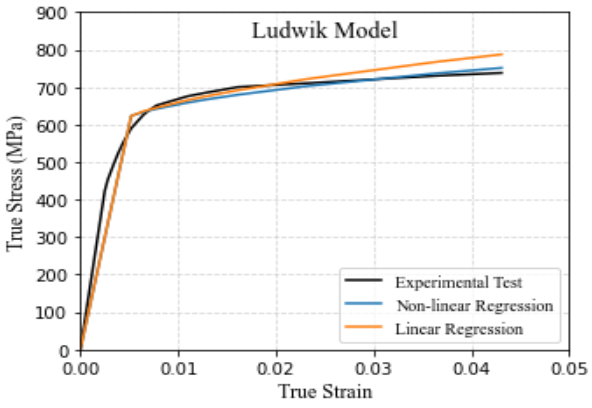

(a)

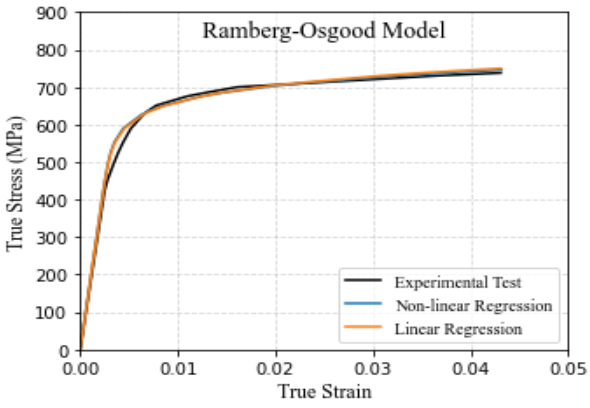

(b)

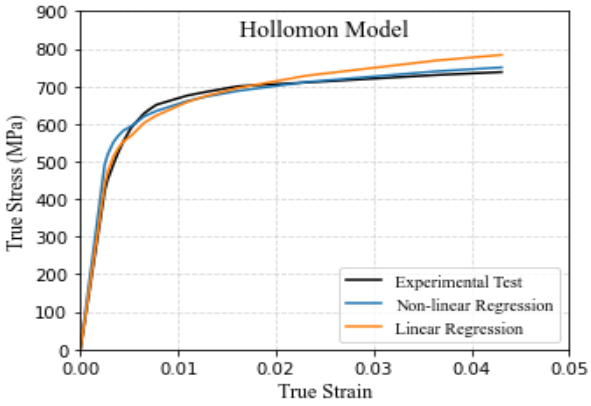

(c)

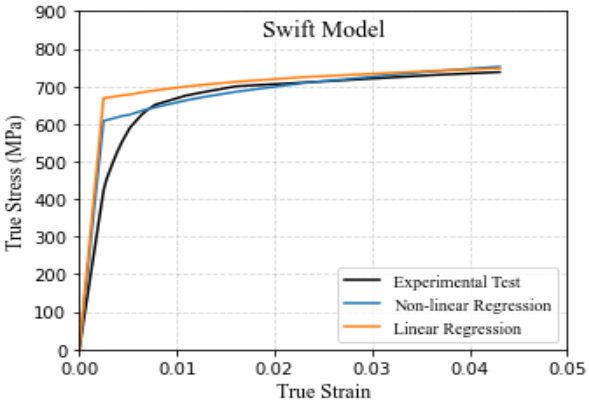

(d)

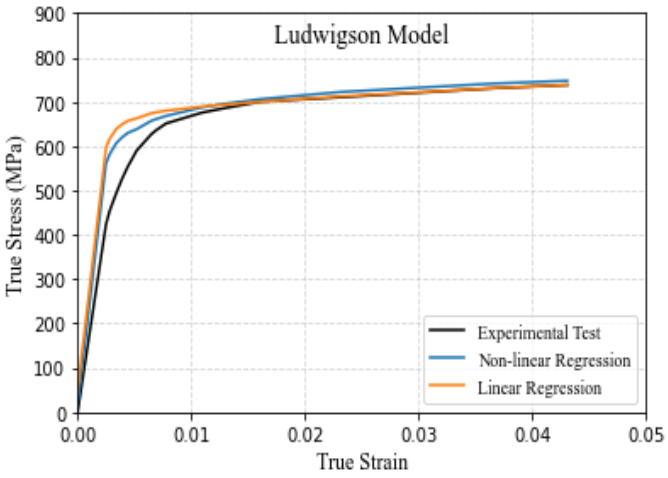

(e)

Figure 3-5: Stress-strain curves for X80 grade generated by non-linear and linear regression technique based on five empirical models

As illustrated in **Figure 3-4** and **Figure 3-5**, it is obvious that the curves generated by LR generally do not match well with the experimental stress-strain curves. By contrast, the actual curves can be described satisfactorily by using NR and the plots regenerated by NL are found to match the experimental curves far better than those generated by LR. Specifically, for X52 pipeline steel, the Ludwigson equation appears to excellently approximate the flow curve, whereas the ROE and the Hollomon equation gave similar results. For X80 pipeline steel, the ROE has a slight edge over the other four equations. The reported fitting parameters for the Ludwik, Ramberg-Osgood, Hollomon, Swift, and Ludwigson models through LR and NR analysis are summarized in **Table 3-1**.

Table 3-1: Obtained model parameters for X52 and X80 pipeline steels

Grade / Regression Methods		**Ludwik**		**RO**		**Hollomon**		**Swift**		**Ludwigson**			
		K_L	n_L	K_{RO}	n_{RO}	K_H	n_H	K_S	n_S	K_1	n_1	K_2	n_2
X52	LR	445.65	0.46	1.0E+25	10.25	931.53	0.195	697.5	0.0929	708.435	0.1092	4.404	-46.27
	NR	526.5	0.59	9.25E+20	8.6	709.2	0.104	694.8	0.1014	706.466	0.1076	4.115	-115.3
X80	LR	1262.1	0.572	4.64E+32	14.31	1094.4	0.103	879.5	0.052	878.011	0.0537	3.948	-168.9
	NR	833	0.5	4.91E+34	15.15	957	0.075	1025	0.099	878.103	0.053	2.67	-10.3

3.3.2 The Applicability and Accuracy of the Empirical Strain Hardening Formulas

Comparisons of the stress-strain curves approximated by the Ludwik, Hollomon, Ludwigson, Ramberg-Osgood, Swift, and CorLAS^{TM} equations with the experimental stress-strain data for X52 and X80 pipeline steels are demonstrated in **Figure 3-6**. The fitting parameters for these constitutive relationships were obtained by performing NR analysis.

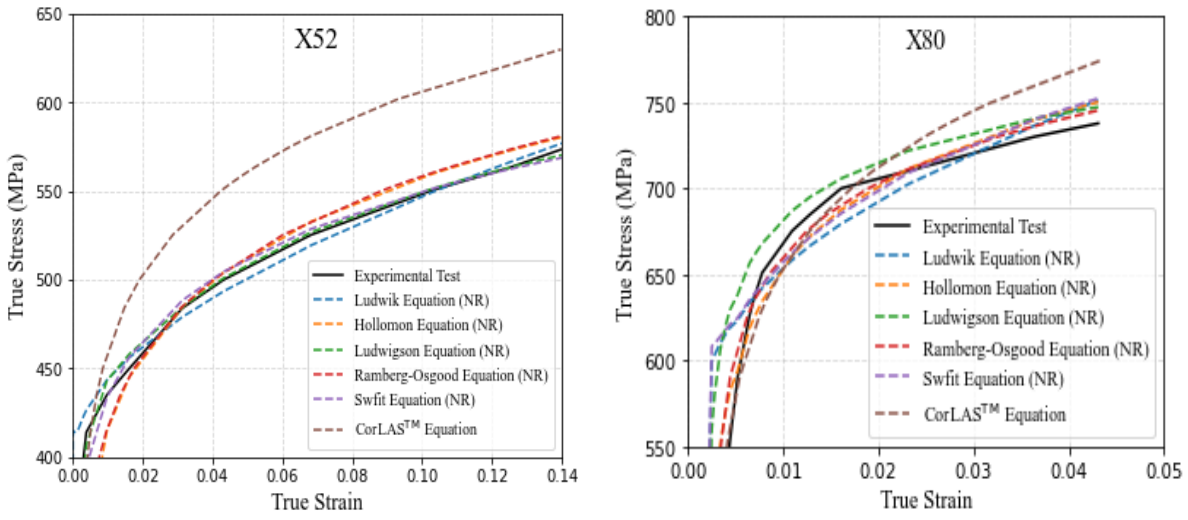

(a) (b)

Figure 3-6: Comparison of flow curves described by different constitutive equations with the experimental curve for (a) X52 grade; and (b) X80 grade

Apparently, for both X52 and X80 pipeline steels, it can be seen that all the constitutive relationships fit the experimental curve well, except the CorLAS™ equation. This is reasonable considering the fact that the strain hardening behavior in the CorLAS™ model is characterized based on the Hollomon equation, and the fitting parameters are obtained from simplified mathematical expressions using the tensile properties (σ_{YS} and σ_{UTS}) instead of obtaining the values through curve fitting techniques. The difference between the reported n values in the Hollomon and CorLAS™ models is shown in

Table 3-2.

Table 3-2: Comparison of the obtained *n* values between the Hollomon and CorLAS equations

Grade	**Strain hardening exponent (n)**	
	Hollomon (NR)	CorLAS™
X52	0.104	0.109
X80	0.075	0.093

3.3.3 Effect of n on the Failure Pressure Predicted by CorLAS^{TM} Model

Due to the variability of the results using different methods to obtain the strain hardening exponent, a sensitivity analysis of the effect of the variation in n on the predictions of the CorLAS^{TM} model is further conducted.

Regarding the computation in CorLAS^{TM} model, the outer diameter (D) of the pipe and wall thickness (t) are taken as 28-inch and 0.375-inch which represent an example of typical dimensions of X42 steel pipelines with specified tensile properties: yield stress (YS) and ultimate tensile stress (UTS) equal to 42000 psi and 60000 psi. Four sizes of crack defects were considered here. The dimensions of the length (L) and depth (a) for a short and shallow crack are $\frac{L}{a} = 10, \frac{a}{t} = 0.3$. The size of a short and deep crack is $\frac{L}{a} = 10, \frac{a}{t} = 0.7$. The size of a long and shallow crack is $\frac{L}{a} = 30, \frac{a}{t} = 0.3$. The size of a long and deep crack is $\frac{L}{a} = 30, \frac{a}{t} = 0.7$.

The failure pressures of pipelines with four crack sizes predicted by the fracture toughness-dependent criterion are found to be approximately linearly proportional to the strain hardening exponent (**Figure 3-7**). As the strain hardening exponent increases, the failure pressure continues to increase. It can be seen that the failure pressures for shallow cracks are higher than those for deep cracks. In addition, for deep cracks, the strain hardening exponent has a small effect on the failure pressure predicted by CorLAS^{TM} as when the strain hardening exponent varies from 0.05 to 0.15, the predicted failure pressures of a long crack and a short crack increase respectively from roughly 705 psi to 810 psi and 980 psi to 1145 psi, implying the effect of n can be considered insignificant. For shallow cracks, the failure pressure increases more sharply with the increase of the strain hardening exponent since the predicted failure pressures of a long crack and a short crack increase respectively from roughly 1165 psi to 1500 psi and 1240 psi to 1600 psi, meaning n can have a profound effect on the failure pressure. Nevertheless, it should be noted that the strain hardening exponent will no longer impact the final failure pressure when the failure pressure predicted by the fracture toughness criterion reaches or exceeds the one by the flow stress-dependent criterion, as the definition of the final pressure in CorLAS^{TM} is the smaller of the values calculated by the two criteria. This scenario typically applies to shallow cracks.

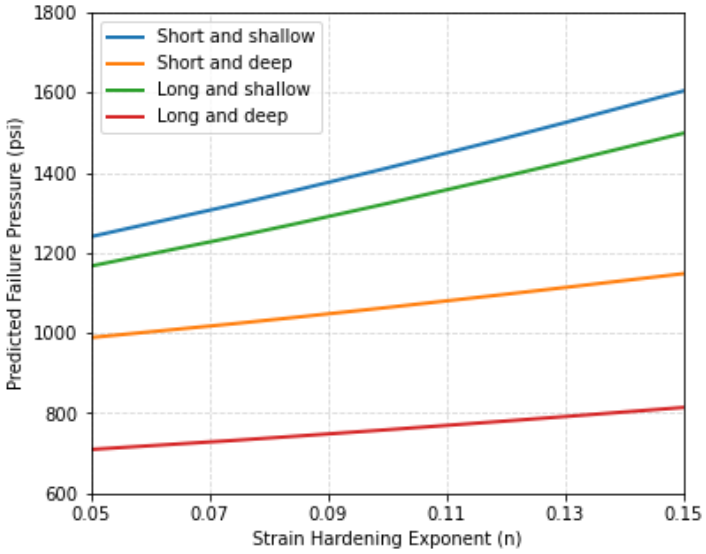

Figure 3-7: Dependence of the strain hardening exponent on the predicted failure pressure

In fact, an investigation is further conducted to compare the predicted failure pressures for different crack dimensions and pipe grades (X52 and X80) when using the obtained n values respectively from the Hollomon and CorLAS^{TM} equations, as listed in

Table 3-2. The information of pipe diameter and wall thickness for X52 and X80 pipe grades are adopted from [27] and [28], the values of D and t for X52 grade are respectively taken as 12.75-inch and 0.27-inch, while those values for X80 grade are taken as 30-inch and 0.5-inch. As can be seen from **Table 3-3**, the predicted failure pressures when using n from CorLAS^{TM} are higher than those by using n from the Hollomon equation, suggesting that CorLAS^{TM} may provide overpredicted results. Moreover, the differences between the failure pressures for both grades using Hollomon and CorLAS^{TM} are insignificant. Specifically, for X52 grade, the differences between the failure pressure values for deep cracks when using Hollomon and CorLAS^{TM} are around 20 psi, and the differences for shallow cracks are 50 psi. For X80 grade, the differences between the failure pressure values for deep cracks are approximately 100 psi and the differences for shallow cracks are 200 psi. By adopting a design factor (DF) with the value of 0.8, the maximum allowable operating pressure (MAOP) can be easily calculated based on the DF, specified minimum yield stress (SMYS), t, and D as: $\text{MAOP} = \frac{2\times\text{DF}\times\text{SMYS}\times\text{t}}{D}$. In this case, the calculated MAOP for the X52 and X80 pipe grades are respectively 1761.9 psi and 2133.3 psi.

Since for shallow cracks and the short & deep crack, the calculated failure pressures are higher than MAOP, the difference between the Hollomon and CorLAS^{TM} equations would not impact the integrity decision making [30].

Table 3-3: Comparison of the failure pressure for different crack sizes and pipe grades using the obtained *n* values from Hollomon and CorLAS^{TM}

Crack Dimensions	**Failure Pressures (psi) (Divided by the SF = 1.25)**			
	X52		X80	
	Hollomon	CorLAS^{TM}	Hollomon	CorLAS^{TM}
Short & shallow	2550.6	2602.5	2783.5	2992.2
Long & shallow	2352.3	2399.2	2594.0	2784.6
Short & deep	1810.4	1836.8	2099.4	2210.6
Long & deep	1300.5	1318.7	1503.5	1579.4

To better illustrate how the values of the strain hardening exponent impact the stress-strain curve, the stress-strain curves are plotted where the strain hardening exponent is taken as 0.05 and 0.15. It can be seen from **Figure 3-8** that the shape of the flow curve alters as the strain hardening exponent varies.

Overall, although the variation in the strain hardening exponent has a discernible effect on the flow curve, its effect on the failure pressure of deep cracks predicted by CorLAS^{TM} is slight, thus, it is suitable to use the Hollomon equation in CorLAS^{TM} to characterize the relationship between true stress and true plastic strain. However, for shallow cracks, previous study [24] showed that CorLAS^{TM} tended to over-predict the failure pressures, thus, additional work would be needed to better understand the effect of the inaccuracies in the Hollomon equation on the overall accuracy of the CorLAS^{TM} prediction results. However, it should be noted that shallow cracks typically are not credible integrity threats and are generally not governed by the fracture toughness criterion.

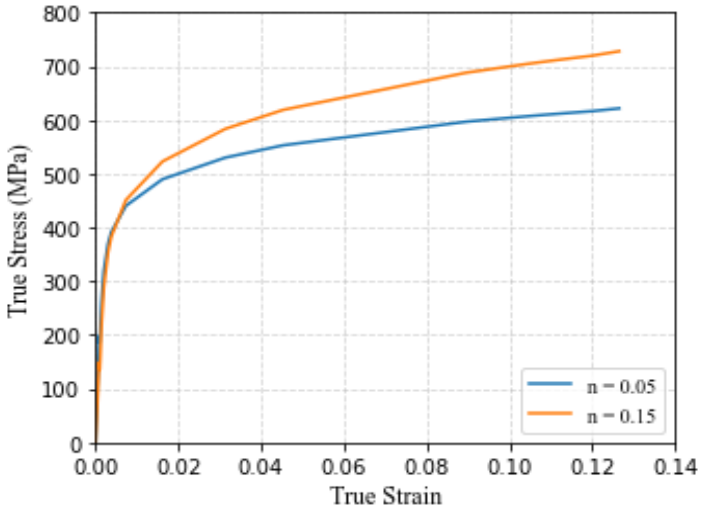

Figure 3-8: Dependence on the strain hardening exponent on the stress-strain curve

3.4 Conclusions

In the present study, a comparison between the linear regression and non-linear regression techniques in terms of describing the stress-strain curves is carried out. Non-linear regression analysis was performed with the utilization of a powerful general-purpose computational software package (Python) coupled with an online platform called MecSimCalc developed recently at the University of Alberta. The results show that the stress-strain curves obtained using non-linear regression technique matched the actual curves better than those obtained by linear regression technique. Thus, to provide a better and more accurate approximation of the flow curves, the fitting parameters for the constitutive relationships should be obtained through non-linear regression analysis for future references.

Moreover, the accuracy of some frequently used constitutive relationships, including the CorLAS^{TM} equation in describing the stress-strain curves, is studied based on the experimental stress-strain data for X52 and X80 grades. The results indicated that all the constitutive equations were able to provide satisfactory approximations of the stress-strain curves for both X52 and X80 grades, except the CorLAS^{TM} equation. Further investigation illustrates that the strain hardening exponent has a minor impact on the predicted failure pressure of pipelines with deep cracks using CorLAS^{TM} model, and while it has a significant impact on the predicted failure pressure of shallow cracks, the calculated failure pressures have much higher values than typical MAOP, implying the

difference between the Hollomon and CorLAS^{TM} equations would not impact the integrity decision making and the Hollomon relationship is suitable to be adopted in CorLAS^{TM}.

Furthermore, given the rather large variability in yield and tensile properties associated with a given pipeline grade, more work is required to examine whether a more accurate strain hardening model would practically precipitate more accurate predictions or not.

References

[1] Tu, X.Y., Ren, Y., Shi, X.B., Li, C.S., Yan, W., Shan, Y.Y. and Yang, K. Enhancing Strain Capacity by the Introduction of Pearlite in Bainite and Polygonal Ferrite Dual-Phase Pipeline Steel. *Materials* Vol. 14 No. 18 (2021):5358.

[2] Kweon, H.D., Kim, J.W., Song, O. and Oh, D. Determination of True Stress-Strain Curve of Type 304 and 316 Stainless Steels using a Typical Tensile Test and Finite Element Analysis. *Nuclear Engineering and Technology* Vol. 53 No. 2 (2021): pp. 647-656.

[3] MechaniCalc. Mechanical Properties of Materials. Accessed in March 2022. https://mechanicalc.com/reference/mechanical-properties-of-materials.

[4] Tu, S.W., Ren, X.B., He, J.Y. and Zhang, Z.L. Stress-Strain Curves of Metallic Materials and Post-necking Strain Hardening Characterization: A Review. *Fatigue and Fracture of Engineering Materials and Structures* Vol. 43 No. 3 (2019): pp. 1-17.

[5] Selin, M. Comparing three equations used for modeling the tensile flow behavior of compacted graphite cast irons at elevated temperatures. *Metallurgical and Materials Transactions A*, Vol. 41 No. 11 (2010): pp. 2805-2815.

[6] Ludwik, P. Elemente der Technologischen Mechanik. *Verlag Von Julius Springer*, Berlin, 1909.

[7] Ramberg, W and Osgood, W.R. Description of stress-strain curves by three parameters. Technical Note No.902, National Advisory Committee For Aeronautics, Washington DC, 1943.

[8] Hollomon, J.R. Tensile deformation. *Transaction of the Metallurgical Society of AIME* Vol. 162, (1945): pp. 268-290.

[9] Swift, H.W. Plastic instability under plane stress. *Journal of the Mechanical and Physics of Solids* Vol. 1 No. 1 (1952): pp. 1-18.

[10] Ludwigson, D.C. Modified stress-strain relation for FCC metals and alloys. *Metallurgical and Materials Transactions B*, Vol. 2 No. 10 (1971): pp. 2825-2828.

[11] Samuel, K.G. Limitations of Hollomon and Ludwigson Stress-Strain Relations in Assessing the Strain Hardening Parameters. *Journal of Physics D: Applied Physics*, 39(1): pp. 203-212, 2005.

[12] Crussard, C.H. and Jaoul, B. Contribution à l'étude de la forme des courbes de traction des me'taux et à son interprétation physique. *Materials Science Revue De Metallurgie*, 47(8), 589–600, 1950.

[13] Liessem, A. Strain Based Design-What the Contribution of a Pipe Manufacturer Can Be. Paper No. ISPOE-I-07-500, *The Seventeenth International Offshore and Polar Engineering Conference*, Lisbon, Portugal, July 2007.

[14] Rasmussen, K.J.R. Full-range Stress-strain Curves for Stainless Steel Alloys. *Journal of Constructional Steel Research*, 59(1), 47-61, 2003.

[15] Hill, H.N. Determination of stress-strain relations from "offset" yield strength values. NACA Technical Note No. 927, Washington, D.C., 1944.

[16] Zhang, X., Okodi, A., Tan, L., Leung, J.Y. and Adeeb, S. Failure pressure prediction of crack in corrosion defects using XFEM. Paper No. IPC2020-9312, *Proceedings of the 13th International Pipeline Conference*, American Society of Mechanical Engineers, Virtual, Online, 2020.

[17] API 579-1/ASME FFS-1, Fitness-for-service, American Society of Mechanical Engineers, USA, 2019.

[18] Zhang, X., Okodi, A., Tan, L., Leung, J.Y. and Adeeb, S. Failure pressure prediction of crack in corrosion defects in 2D by using XFEM. Paper No. PVP2020-21046, *Proceedings of the Pressure Vessel and Piping Conference*, American Society of Mechanical Engineers, Virtual, Online, 2020.

[19] Nutor, R.K., Adomako, N.K. and Fang, Y.Z. Using the Hollomon model to predict strain-hardening in metals. *American Journal of Materials Synthesis and Processing*, 2(1), 1-4, 2017.

[20] Hertelé, S., Waele, W.D. and Denys, R. A generic stress-strain model for metallic materials with two-stage strain hardening behavior. *International Journal of Non-Linear Mechanics*, 46(3), 519-531, 2011.

[21] Reed-Hill, R.E., Cribb, W.R. and Monteiro, S.N. Concerning the Analysis of Tensile Stress-Strain Data Using Log $(d\sigma/d\varepsilon_p)$ versus Log σ Diagrams. *Metallurgical Transaction* Vol. 4 (1973): pp. 2665-2667.

[22] Lavakumar, A., Sarangi, S.S., Chilla, V., Narsimhachary, D. and Ray, R.K. A "new" empirical equation to describe the strain hardening behavior of steels and other metallic materials. *Materials Science and Engineering A*, 802(2021)140641.

[23] Jaske, C.E., Beavers, J.A. and Harle, B.A. Effect of stress corrosion cracking on integrity and remaining life of natural gas pipelines. Paper No. 255, Corrosion 96, NACE International, Houston, 1996.

[24] Zhang, X., Zheng, Q., Leung, J.Y. and Adeeb, S. Reliability-based assessment of cracked pipelines using monte carlo simulation technique with CorLAS^{TM}. Paper No. PVP2022-80412, *Proceedings of the Pressure Vessel and Piping Conference*, *American Society of Mechanical Engineers,* Las Vegas, USA, 2022.

[25] Jaske, C. E. and Beavers, J. A. Integrity and Remaining Life of Pipe with Stress Corrosion Cracking. PRCI 186-9709, Catalog No. L51928. Pipeline Research Council International, Falls church, 2001.

[26] Polasik, S.J., Jaske, C.E. and Bubenik, T.A. Review of engineering fracture mechanics model for pipeline applications. Paper No. IPC2016-64605, *Proceedings of the 11th International Pipeline Conference*, *American Society of Mechanical Engineers*, Calgary, Canada, 2016.

[27] Lin, M. Characterization of tensile and fracture properties of X52 steel pipes and their girth welds. MSc Thesis, University of Alberta, Edmonton, Canada. 2015.

[28] Fathi, A. Effects of Material Anisotropy on the Buckling Resistance of High Strength Steel Pipelines. PhD Thesis. University of Alberta, Edmonton, Canada. 2012.

[29] Adeeb, S. The simplest way to share computational tools. MecSimCalc. Accessed in 2022. https://www.mecsimcalc.com/app/.

[30] Hart Energy. Accessed in 2024. Not every pipeline repair is equally urgent. How can pipeline operators tell the difference? https://www.hartenergy.com/exclusives/better-prediction-30439#:~:text=A%20small%2C%20shallow%20crack%20typically,to%20develop%20until%20failure%20occurs.

CHAPTER 4: COMPARATIVE STUDY OF CRACK SHAPE ON THE DUCTILE FRACTURE RESPONSE OF CRACKED PIPELINES

This chapter is derived from a research article that intended for publication in the following conference proceeding:

Zhang, X., Yoosef-Ghodsi, N., Kainat, M., Leung, Y.J. and Adeeb, S., Comparative study of crack shape on the ductile fracture response of cracked pipelines, Proceeding of the ASME 2024 Pressure Vessels & Piping Conference, July 29-August 2, 2024, Bellevue, Washington, USA, PVP2024-121892.

Abstract

Buried pipelines are subjected to various types of loads, including external pressure from soil overburden and internal pressure from pressurized fluids. These loads can induce axial and hoop stresses, which are the primary factors leading to the formation of integrity threats, such as cracks. The presence of cracks can render a pipeline susceptible to failure, posing a significant threat to its operation, safety, and the environment. This underscores the importance of promptly detecting and evaluating even seemingly minor surface defects, as they can significantly damage the structural integrity of the pipeline. It is also crucial to accurately predict the failure pressures of pipelines with cracks to ensure that the operating pressure remains below this critical limit with an adequate margin of safety. A variety of approaches exist for assessing cracks in pipes, including empirical approaches such as MAT-8, Ln-Sec and CorLAS^{TM} models, as well as numerical approaches like the extended finite element method (XFEM). XFEM is a powerful tool to estimate the failure pressures of pipelines containing cracks. It extends the capabilities of the traditional Finite Element Method (FEM) and offers a more effective means of simulating crack propagation. In ABAQUS, initial cracks can be modelled in either sharp or blunted shapes. However, it is uncertain whether the shape of the crack affects the failure pressures of cracked pipelines. For this purpose, parametric study is necessary to investigate the implications of pre-existing cracking shapes on the ductile fracture response of pipes subjected to pure mode I loading.

Keywords: Pipeline failure; fracture; XFEM; crack; crack shape

NOMENCLATURE

The following abbreviations are defined and used thereafter:

a	Crack depth
CMOD	Crack mouth opening displacement
CTOD	Crack tip opening displacement
D	Outer diameter
DIC	Digital image correlation
DOF	Degrees of freedom

E	Young's modulus
FEA	Finite element analysis
FEM	Finite element method
G_C	Fracture energy
L	Length of the pipe model
LEFM	Linear elastic fracture mechanics
MAXPE	Maximum principal strain
MAXPS	Maximum principal stress
RP	Reference point
t	Pipe wall thickness
TSL	Traction-separation law
XFEM	Extended finite element method
Δa	Crack extension
θ	Rotation angle at the surface plane
σ_{YS}	Yield strength
σ_{UTS}	Ultimate tensile strength

4.1 Introduction

Cracks can be found in high-pressure infrastructure components like pipelines either at the beginning of service due to manufacturing or installation or form during operation. Cracks may occur in the pipe wall in various directions, which makes them a major concern to the safe operation of pipelines. When the steel pipelines are located underground and transport highly pressurized substances from remote areas, they experience internal and external loadings, which produce circumferential stress and longitudinal stress in the pipe wall. Circumferential (or hoop) stress results from internal fluid pressures, and it can cause the initiation of axial cracks, while longitudinal stress (or axial stress) is often generated from external loadings such as the soil

loading due to ground settlement or slope movement and the live load (vehicles) on the ground surface if pipelines are crossing construction sites, which create an environment for circumferential cracks [1]. The live surface loading can also generate significant hoop stresses (or stress cycles), and thus contribute to axial crack initiation and propagation. When the internal pressure is the primary loading, axial cracks are of more structural integrity concern than the circumferential cracks as the hoop stress is much higher than the longitudinal stress.

Although naturally occurring cracks are often in irregular shapes, crack defects that are considered in simulations are typically in idealized shapes. XFEM is available in several finite element analysis (FEA) software packages such as ABAQUS [2] and ANSYS. The numerical work conducted in this study was performed using ABAQUS/CAE. In ABAQUS, surface cracks can be modelled as either sharp or blunted. A sharp crack is generated by simply embedding a planar part into the pipe body [3], while a blunted crack is often created by adding a cut feature, commonly referred to as an open crack, such as a notch.

The applications of XFEM have been explored extensively by previous researchers [4-9]. Zhang et al. [4] evaluated the burst capacity of cracked pipelines subjected to internal pressure using XFEM implemented in ABAQUS software. Later, the same authors [6] employed the XFEM technique in predicting the failure pressure of pipes containing the hybrid defect, i.e., cracks in corrosion, where the crack was simulated with a rectangular shape, uniform depth, embedded in a semi-elliptical shaped corrosion defect, and the combined defect was placed at the outer diameter surface of the pipe. Okodi et al. [7] investigated the effect of the crack location on the failure pressure of pipelines with cracks in dent defects. In their models, the semi-elliptical crack was placed inside a rectangular dent in the axial direction. The predicted results using the above-mentioned numerical models agreed well with the published burst test data, showing the effectiveness of XFEM in predicting the failure pressure of pipes containing not only single crack defects but also hybrid defects. Moreover, XFEM has also proven to be an attractive approach in predicting the ductile fracture response of cracked pipelines. Lin et al. [8] calibrated and validated two XFEM models of pipes containing circumferential cracks based on two damage parameters, i.e., the maximum principal stress (MAXPS) and fracture energy (Gc), by changing one parameter while keeping the other parameter constant to match the load versus crack mouth opening displacement (CMOD) curve obtained from their numerical simulations to the experimentally measured load versus CMOD curve. In their models, the circumferential crack was placed at the

middle length of the pipe and generated in rectangular shapes. A good agreement between the numerical and experimental results was achieved when the MAXPS = 700 MPa and Gc = 900 N/mm. This optimal damage parameter set was then used to predict the tensile strain capacity. Similarly, Agbo et al. [9] calibrated the XFEM damage parameters (maximum principal strain (MAXPE) and Gc) by numerically fitting experimental CMOD-Moment curves obtained from four-point bending tests. The initial crack in their models was created as a rectangular crack and inserted into a specific location. It is noteworthy here that the experimental data used by [8] and [9] were obtained from eight full-scale pressurized tests conducted by the pipeline research group at the University of Alberta [10-11].

While the XFEM modelling technique has proven to be an effective and accurate tool in simulating the crack propagation with initial sharp cracks, the ductile fracture behavior of an initially blunted crack has not been well understood. Apparently, there is a need to investigate the implications of crack shape on the burst capacity of cracked pipelines and the difference between sharp and blunted cracks on the ductile fracture behavior of pipelines. In this chapter, the sharp crack in the parametric studies is considered as a rectangular-shaped crack with uniform depth as it is the most severe scenario.

The remaining of this chapter is organized as follows: the basic concept of XFEM is introduced in **Section 4.2**, followed by a detailed description of the numerical model setup, including information on meshing, loading, and boundary conditions. **Section 4.3** presents the obtained numerical results for the parametric studies along with discussions. Finally, key findings are summarized at the end of the chapter.

4.2 Extended Finite Element Method (XFEM)

For decades, the conventional finite element method (FEM) has been employed to solve the fracture problem; however, it is not a preferrable approach when it comes to modelling strong discontinuities such as cracks in complex geometries due to the conformal mesh requirement [11]. When simulating crack propagation using the FEM technique, it is always necessary to re-mesh the finite elements to conform to the crack geometry, typically with very fine meshes at the crack front vicinity, which is tedious and may incur numerical difficulties [11]. To mitigate the difficulties of mesh refinement, the extended finite element method (XFEM) was proposed by

Belytschko and his collaborators [12] based on the partition of unity [13] by introducing two extra enrichment functions (**Figure 4-1**) to the conventional finite element approximation as an alternative approach to solve dynamic crack problems. In XFEM, cracks are no longer required to be coincident with the edges of the finite elements, thereby alleviating the burden of re-meshing and simulating crack growth in a simplified manner.

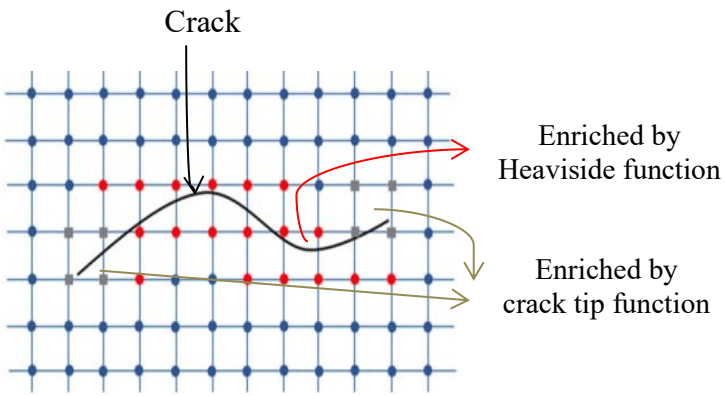

Figure 4-1: XFEM enrichment scheme: squares show nodes enriched with crack tip functions while the circles indicate the nodes enriched with Heaviside function, adapted from [14]

ABAQUS currently offers two distinct modelling approaches to simulate the crack initiation and propagation process within the XFEM framework, i.e., the XFEM-based cohesive segments method [5] and the XFEM-based Linear Elastic Fracture Mechanics (LEFM) method. The principle of LEFM is recommended to model brittle fracture, while the former is appropriate to model ductile or brittle fracture. Another advantage of the XFEM-based cohesive segment method is that it does not need a pre-defined crack propagation path, as the crack is no longer tied to the element boundaries. The failure mechanism of this approach consists of a damage initiation criterion and a damage evolution law. Once the damage initiation criterion is met, the crack propagates according to a user-defined damage evolution law.

4.3 Parametric Analysis

To explore the impact of initial crack shapes on the ductile fracture response of cracked pipelines, the parametric study encompasses two types of initial cracks (depicted in **Figure 4-2** as the red-colored area). A sharp crack is idealized and modelled as a rectangular-shaped defect with

uniform depth, and it is in axial direction because, compared to circumferential cracks, axial cracks are more critical. The blunted crack is simulated as a notch with a small tip radius equal to 0.05 mm. The pipe attributes (D, t, E, σ_{YS}, and σ_{UTS}) for the parametric cases are partially retrieved from [15], as tabulated in **Table 4-1**. Both the notch and crack depths are set at 52% of the wall thickness, rounding up to 3 mm and the lengths of the defects are taken as 200 mm.

Table 4-1: Mechanical properties of the steel pipe

	Steel grade	***D*** **(mm)**	***t*** **(mm)**	***L*** **(mm)**	***E*** **(GPa)**	$\boldsymbol{\sigma_{YS}}$ **(MPa)**	$\boldsymbol{\sigma_{UTS}}$ **(MPa)**
Test	X60	508	5.7	1800	207	433	618

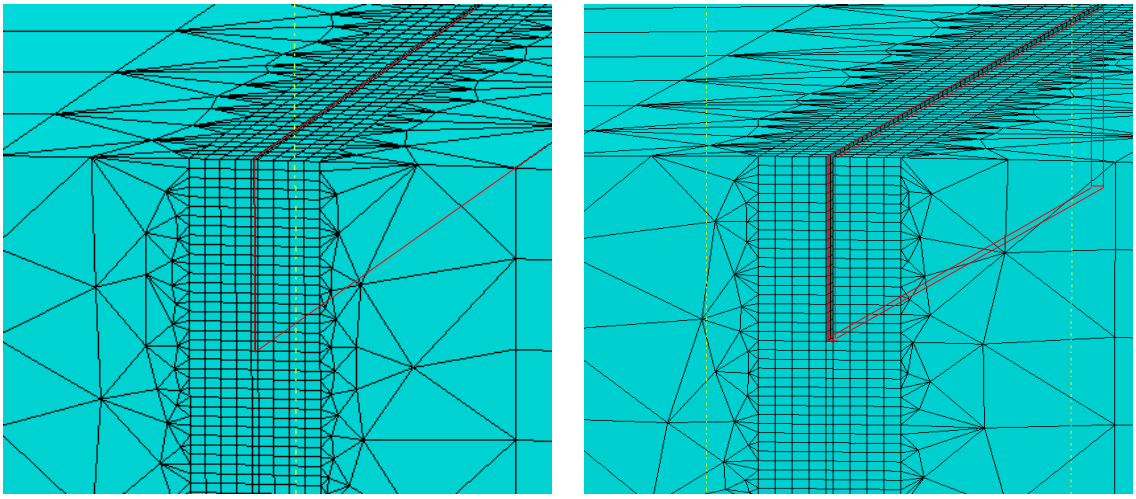

Figure 4-2: Pre-existing cracks in the numerical models: sharp crack (left); blunted crack (right)

For the sake of simplicity, only half of the pipe is modelled by taking advantage of its symmetric property to reduce the computation cost. The same symmetric boundary conditions as in our previous papers [3,5] are employed. A reference point (RP) is coupled to the left end of the pipe by kinematic coupling to allow that side to be fixed yet still capable of expanding. A uniform pressure of 10 MPa is applied to all the interior surfaces of the pipe. **Figure 4-3** shows the numerical model with the applied boundary and loading conditions. The crack defect is located on the external surface at the middle of the pipe body. To ensure an appropriately fine mesh size so

that the crack propagation can be captured better with moderate computation cost, the mesh size for the model is selected based on a mesh sensitivity study conducted in [6]. The finite element meshes of the pipe body and crack domain are constructed using three-dimensional, 8-node linear brick elements with reduced integration (C3D8R). The transmission area is meshed with 10-node quadratic tetrahedral elements (C3D10). It is important to note that the crack part need not to be meshed or assigned any material properties [3].

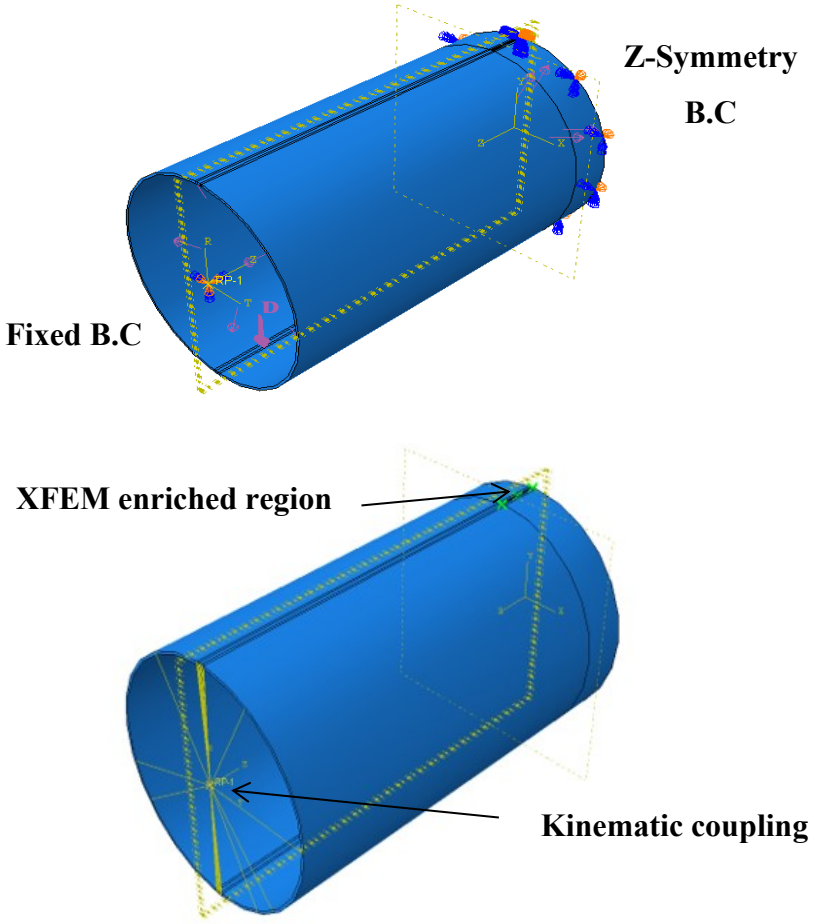

Figure 4-3: Schematic of the numerical model

This work adopts the XFEM-based cohesive segments approach to simulate the crack propagation. As mentioned previously, two key fracture properties govern the onset of crack initiation and the rate of crack propagation. The built-in crack initiation criterion employed in this study is the maximum principal strain (MAXPE) criterion, i.e., the crack is assumed to initiate when the maximum principal strain criterion is met. The crack propagation is defined in terms of

the energy required for failure, known as fracture energy (G_C), which is equal to the entire area under the traction-separation law (TSL) curve (**Figure 4-4**). When the dissipated energy due to the crack opening reaches or exceeds the critical G_C, the failure occurs. It is critical to note that the crack always propagates in the direction perpendicular to the maximum principal strain.

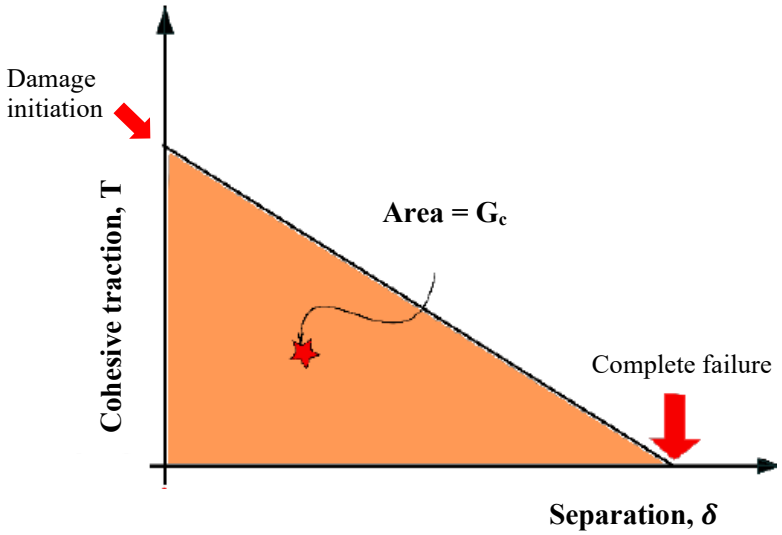

Figure 4-4: Traction-Separation Law curve, adapted from [16]

The failure pressure, as the name implies, is the maximum load at which a pipeline can withstand before it fails. In the context of the XFEM modelling conducted in this study, the failure pressure corresponds to the pressure at which the pipe wall is thoroughly breached by the crack. **Figure 4-5** shows the stress distribution in the crack region at the time step at which the ultimate failure occurs. It can be seen from the figures that the stress distributions of sharp crack and blunted crack at the moment of failure are basically the same.

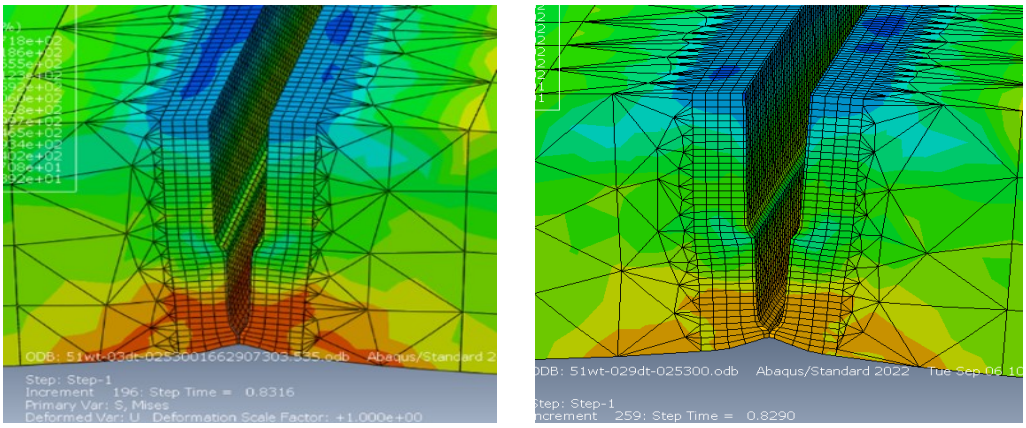

(a) Blunted crack (b) Sharp crack

Figure 4-5: Stress distribution of the crack region at failure: (a) blunted crack; (b) sharp crack

Generally, failure due to the presence of cracks is evaluated based on fracture mechanics, thus, fracture mechanics parameters like crack-tip opening displacement (CTOD) and crack mouth opening displacement (CMOD) play an important role in characterizing the ductile fracture behavior of material. For ductile material, the conceptual definition of CTOD can be understood as the opening displacement of the deformed crack at the tip position. CMOD, on the other hand, is the opening displacement of the crack specimen at its surface and can be directly measured from laboratory testing either through single- or double-clip gauge measurement techniques or with advanced tools such as digital image correlation (DIC). However, due to the inherent difficulties in directly measuring CTOD, i.e., it is hard to locate the crack tip precisely once the crack grows, its value is often derived from the experimentally measured CMOD using a simple mathematical expression (as shown in **Figure 4-6**). In the numerical simulations, CMOD is defined as the nodal distance between the two upper faces of a growing crack, while CTOD is measured as the nodal displacement near the original crack tip, as depicted in **Figure 4-7**.

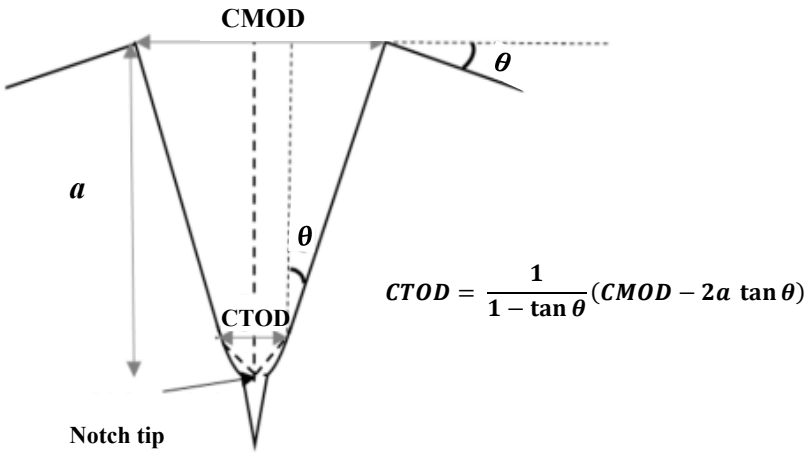

Figure 4-6: Calculation of CTOD, adapted from [17]

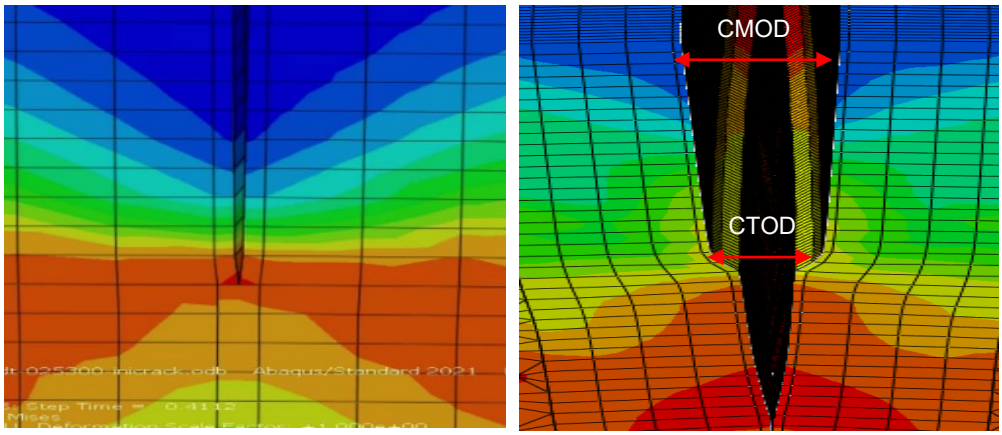

Figure 4-7: Measurement of the CMOD and CTOD in simulations

The sensitivity studies of fracture energy and maximum principal strain on the load versus displacement curves are carried out subsequently, and the results are presented in Figures 4-8 to 4-14. The maximum principal strain and fracture energy values were selected from the following sets:

- MAXPE values: 0.015, 0.02, 0.025, and 0.03
- G_C values: 50, 150, 300, and 400 N/mm

Initially, the MAXPE value is fixed at 0.025 while G_C is varied from 50 to 400 N/mm. **Figure 4-8** illustrates the impact of the crack shape and different fracture energies on the load versus crack extension curve. In general, the difference between the sharp crack (S) and blunted crack (B) in the load versus crack extension curve is not significant. The difference in failure pressures is more noticeable for higher fracture energy values, where blunted cracks show slightly higher failure pressure values. Only a slight difference is observed between the sharp crack and blunted crack at the initial crack propagation stage (Δa is less than approximately 0.3mm). An effort is made to reconcile this discrepancy by decreasing the time increment size to apply the load more gradually; however, the difference is not eliminated. A subsequent attempt is made by comparing the variation of the equivalent plastic strain (PEEQ) at the crack tip between the two types of cracks (**Figure 4-12**); the results indicate that the blunted crack exhibits a higher strain at the crack tip compared to the sharp crack for the MAXPE value of 0.025. Consequently, the observed discrepancy at the onset of crack propagation is reasonable, as higher strain is associated with lower pressure at the onset of crack propagation. The same observation was reported by Lin et al. [18]. Their study compared the J integral versus crack extension curve (J-R curve) between a sharp planar crack and a blunted notch when employing the MAXPE initiation criterion. Their results demonstrated that the J-integral value associated with a sharp crack was slightly higher than that of a blunted notch when $\Delta a < 0.3$mm and the effect of the crack shape has minimal impact on the J-R curve. The authors believed that the difference was caused by the existence of the initial cohesion at the crack tip region of a sharp crack.

The load versus CMOD and load versus CTOD curves, using sharp and blunted cracks with various fracture energy values, are respectively demonstrated in **Figure 4-9** and **Figure 4-10**. As can be observed from these curves, there is no discernable difference between the sharp crack and blunted crack in terms of ductile fracture behavior for relatively high fracture energy (300 and 400 N/mm). Slight differences are noticed at low fracture energy cases (50 and 150 N/mm). **Figure 4-11** shows the displacement versus crack extension curve for different crack shapes and fracture energy values. It reveals that both factors had negligible effects on the relationship between displacement and crack extension.

Overall, as expected, an increase in fracture energy corresponds to an increase in the failure pressure. This could be explained by the definition of the fracture energy from the TSL curve (**Figure 4-4**), which is equivalent to the area enclosed by the TSL curve. Fixing the damage

initiation point and subsequently increasing the fracture energy results in a larger area of the TSL curve. This, in turn, leads to a larger separation at failure. This observation is aligned with findings from Lin et al. [7] and Moghaddam et al. [19]. The former authors conducted a sensitivity analysis of maximum principal stress and fracture energy by plotting the CMOD versus applied force to identify the most suitable damage parameter set. The latter authors explored the effect of the fracture energy on the force-displacement curve for a three-point bending beam model subjected to pure mode I. During their investigation, only fracture energy was changing while other parameters were kept constant. Their results indicated higher fracture energy values produced a higher burst load.

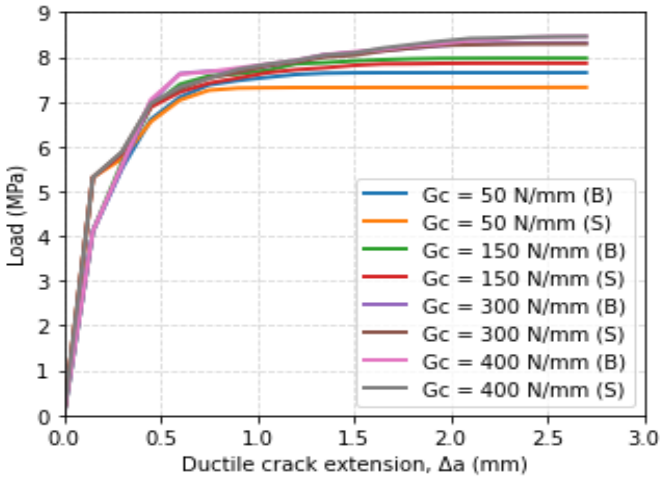

Figure 4-8: Effect of fracture energy on Load-Δa curve

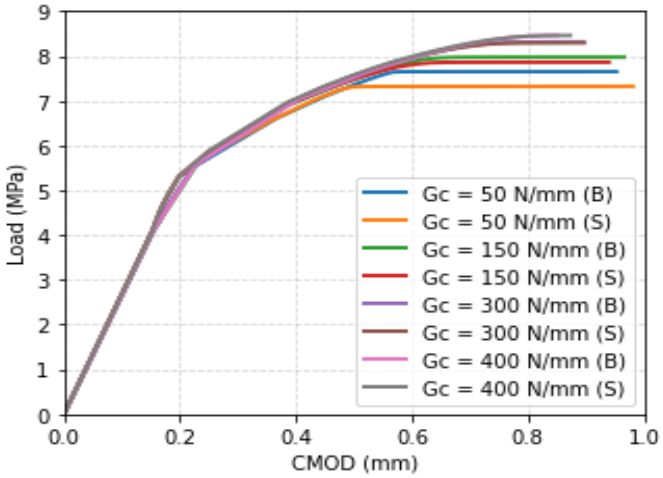

Figure 4-9: Effect of fracture energy on Load-CMOD curve

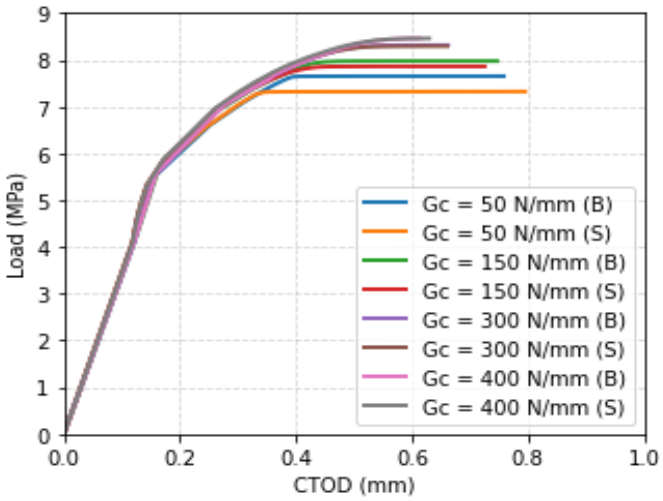

Figure 4-10: Effect of fracture energy on Load-CTOD curve

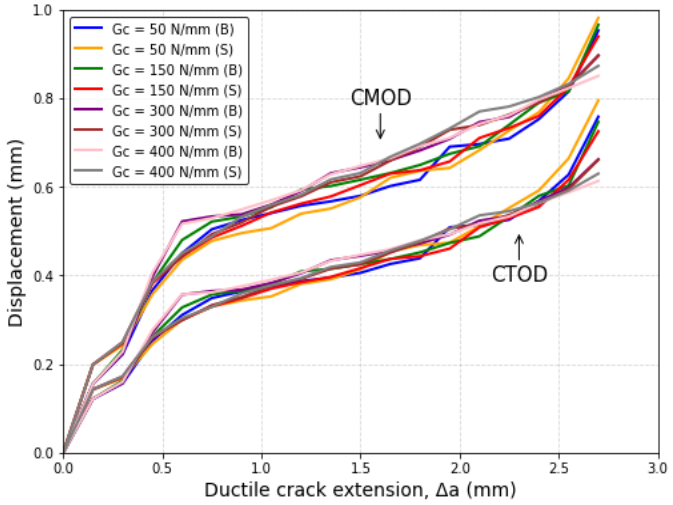

Figure 4-11: Effect of fracture energy on displacement-Δa curve

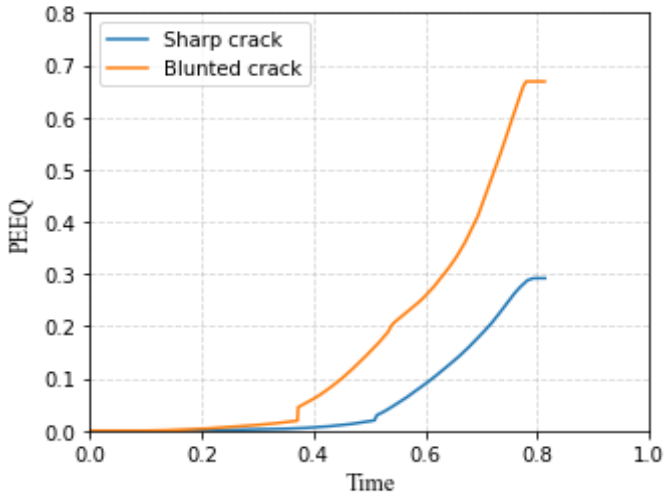

Figure 4-12: Variation of PEEQ between a sharp crack and a blunted crack (notch)

The next set of results are obtained for a fixed G_C value of 300 N/mm. The impact of crack shape at different maximum principal strain values on the load versus crack extension curve is presented in **Figure 4-13**. Consistent with the findings in **Figure 4-8**, the initial sharp crack exhibits higher pressure than the blunted crack at the onset of crack propagation. In contrast to the effect of fracture energy, the load-Δa curve is relatively insensitive to changing the maximum principal strain. As shown in **Figure 4-14** and **Figure 4-15**, a blunted crack (notch) has a slightly higher failure pressure than a sharp crack at higher MAXPE values (0.025 and 0.03), but the trend reverses at lower MAXPE values (0.015 and 0.02).

Overall, the failure pressure increases with the increase of the maximum principal strain. A similar observation was reported by Agbo et al. [8], who investigated the influence of the maximum principal strain on the load-deformation curve of a four-point bending model. Their study involved varying strain values from 0.009 to 0.02 while the fracture energy remained constant at 500 N/mm. The results showed that the load increased as the maximum principal strain increased.

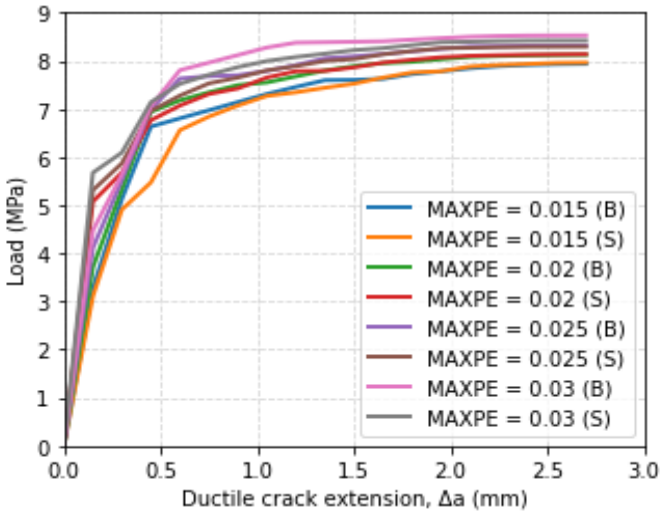

Figure 4-13: Effect of the maximum principal strain on Load-Δa curve

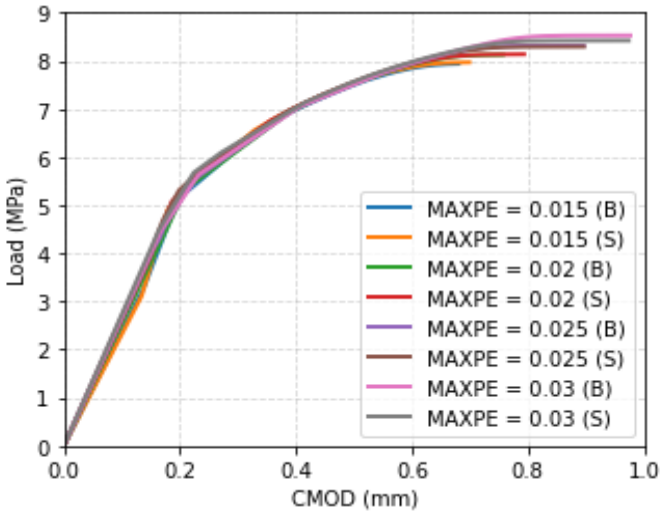

Figure 4-14: Effect of the maximum principal strain on Load-CMOD curve

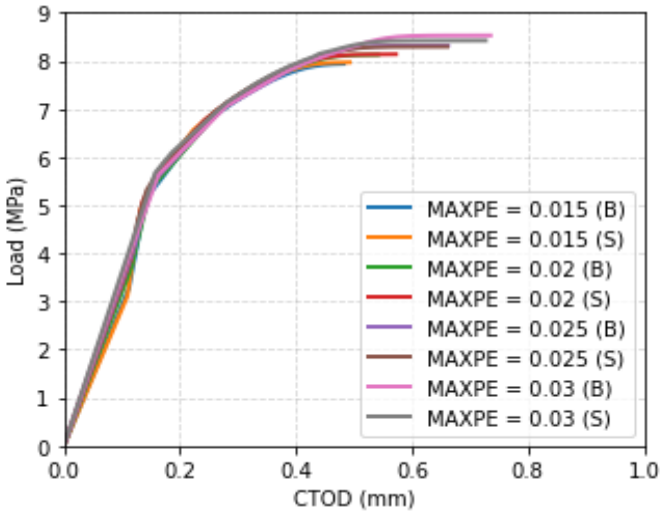

Figure 4-15: Effect of the maximum principal strain on Load-CTOD curve

4.4 Conclusions

Parametric analyses are conducted in this chapter to investigate the implications of crack shape, specifically a rectangular-shaped sharp crack and a blunted crack, along with two XFEM damage parameters (MAXPE and G_C) on the ductile fracture response of cracked pipelines. The following observations are as follows:

- A sharp crack requires a higher force than a blunted crack to initiate propagation, attributed

to the initial cohesion at the crack tip vicinity.

- Failure pressure increases with the increase of fracture energy and the maximum principal strain values.
- Compared to maximum principal strain, ductile fracture response is more sensitive to fracture energy.
- The difference between a rectangular-shaped crack and a blunted crack on the load-displacement response is found to be negligible.

References

[1] Fan, Z., Branam, N., Zand, B. and Auker, M.V. A new approach to determine the stresses in buried pipes under surface loading. Paper No. IPC2016-64050, *Proceedings of the 2016 11th International Pipeline Conference, American Society of Mechanical Engineers*, Calgary, Alberta, Canada, 2016.

[2] Dassault Systèmes, 2022. Abaqus documentation.

[3] Zhang, X., Okodi, A., Tan, L., Leung, J.Y. and Adeeb, S. Failure pressure prediction of crack in corrosion defects using XFEM. Paper No. IPC2020-9312, *Proceedings of the 2020 13th International Pipeline Conference, American Society of Mechanical Engineers*, Virtual, Online, 2020.

[4] Zhang, X., Okodi, A., Tan, L., Leung, J.Y. and Adeeb, S. Failure pressure prediction of crack in corrosion defects in 2D by using XFEM. Paper No. PVP2020-21046, *Proceedings of the Pressure Vessel and Piping Conference, American Society of Mechanical Engineers*, Virtual, Online, 2020.

[5] Zhang, X., Lin, M., Okodi, A., Tan, L., Leung, J.Y. and Adeeb, S. Numerical analysis of API X42 and X52 vintage pipes with cracks in corrosion defects using extended finite element method. Paper No. PVT-20-1218, *Journal of Pressure Vessel Technology*, 143(6):061302, 2021.

[6] Okodi, A., Li, Y., Cheng, J.J.R., Kainat, M., Yoosef-Ghodsi, N. and Adeeb, S. Effect of location of crack in dent on burst pressure of pipelines with combined dent and crack defects. *Journal of Pipeline Science and Engineering*, 1(2): 252-263, 2021.

[7] Lin, M., Agbo, S., Cheng, J.J.R., Yoosef-Ghodsi, N. and Adeeb, S. Application of the Extended Finite Element (XFEM) to Simulate Crack Propagation in Pressurized Steel Pipes. Paper No. PVP2017-65575, *Proceedings of the Pressure Vessel and Piping Conference, American Society of Mechanical Engineers,* Hawaii, USA, 2017.

[8] Agbo, S., Lin, M., Amerli, I., Imanpour, A., Duan, D-M., Cheng, J.J.R. and Adeeb, S. Evaluation of the effect of internal pressure and flaw size on the tensile strain capacity of X42 vintage pipeline using damage plasticity model in extended finite element method (XFEM). Paper No. PVP2019-94005, *Proceedings of the Pressure Vessel and Piping Conference, American Society of Mechanical Engineers*, San Antonio, Texas, USA, 2019.

[9] Abdulhameed, D., Cakiroglu, C., Lin, M., Cheng, J.J.R., Nychka, J., Sen, M. and Adeeb, S. The Effect of Internal Pressure on the Tensile Strain Capacity of X52 Pipelines with Circumferential Flaws. Paper No. PVT-15-1045, *Journal of Pressure Vessel Technology*, 138(6):061701, 2016.

[10] Agbo, S., Lin, M., Ameli, I., Imanpour, A., Duan, D-M., Cheng, J.J.R. and Adeeb, S. Experimental Evaluation of the Effect of the Internal Pressure and Flaw Size on the Tensile Strain Capacity of Welded X42 Vintage Pipelines. *International Journal of Pressure Vessels and Piping*, Vol. 173, pp. 55-67, 2019.

[11] Abaqus 6.14. Abaqus Analysis User's Guide, Dassault Systèmes, 2014.

[12] Belytschko T. and T. Black. Elastic crack growth in finite elements with minimal remeshing. *International Journal for Numerical Methods in Engineering*, 45, 601-620, 1999.

[13] Melenk, J.M. and Babuška, I. The partition of unity finite element method: basic theory and applications. *Computer Methods in Applied Mechanics and Engineering*, 139(1-4): 289–314, 1996.

[14] Gairola, S and Ren, J. XFEM simulation of tensile and fracture behavior of ultrafine-grained AI 6061 alloy. *Metals*, 11(11):1761, 2021.

[15] Hosseini, A., Cronin, D., Plumtree, A. and Kania, R. Experimental Testing and Evaluation of Crack Defects in Line Pipe. Paper No. IPC2010-31158, *Proceedings of the 8th International Pipeline Conference*, *American Society of Mechanical Engineers,* Calgary, Canada, 2010.

[16] Haddad, M. Integration of XFEM and CZM to model 3D multiple-stage hydraulic fracturing in quasi-brittle shale formations: Solution-dependent propagation direction. *Proceedings of the 2015 AADE National Technical Conference and Exhibition*, San Antonio, Texas, USA, 2015.

[17] Samadian, K., Hertele, S. and Waele, W.D. Using 3D Digital Image Correlation (3D-DIC) to Measure CTOD in a Semi-Elliptical Surface Crack. *The Eighteenth International Conference of Experimental Mechanics*, 2(8):5311, 2018.

[18] Lin, M., Li, Y., Cheng, J.J.R., Koduru, S., Kainat, M., Zhang, X. and Adeeb, S. Novel XFEM Variable Strain Damage Model for Predicting Fracture in Small-scale SENT and Full-scale Pipe Tests. *Engineering Fracture Mechanics*, 271(2):108628, 2022.

[19] Moghaddam, H.N., Keyhani, A. and Aghayan, I. Modeling of Crack Propagation in Layered Structures Using Extended Finite Element Method. *Civil Engineering Journal*, 2(5):180-188, 2016.

CHAPTER 5: ESTABLISHING THE CORRELATION BETWEEN CHARPY V-NOTCH (CVN) TOUGHNESS AND XFEM DAMAGE PROPERTIES

This chapter is derived from a research article submitted for publication in the International Journal of Pressure Vessel and Piping: Zhang, X., Yoosef-Ghodsi, N., Leung, J.Y. and Adeeb, S. Establishing the correlation between the Charpy V-Notch (CVN) toughness and XFEM damage properties (under review).

Abstract

Prompt detection or management of imperfections, such as cracks or crack-like anomalies, in onshore and offshore oil and gas pipelines is one of the main challenges in pipeline maintenance. The presence of cracks can compromise structural integrity, potentially resulting in severe economic and environmental consequences. The repair or replacement of damaged pipe segments incurs substantial costs, which makes accurately evaluating their failure pressures crucial. The failure pressures of pipelines containing surface cracks can be predicted using fracture mechanics-based analytical models, such as CorLAS^{TM} and Ln-Sec models, or through numerical tools. A more recently developed numerical approach, known as the eXtended Finite Element Method (XFEM), extends the capabilities of the traditional Finite Element Method (FEM) and offers a more effective means of modelling crack growth. In ABAQUS software, XFEM is often employed in conjunction with the cohesive segment modelling approach, consisting of a damage initiation criterion and a damage evolution law to simulate crack initiation and propagation. In this XFEM-based approach, fracture criteria are typically defined using two damage properties that are specific to the material properties. Similarly, in fracture mechanics models, fracture toughness parameters are also determined either through standard fracture testing of the materials or derived from Charpy energy using empirical correlations. Therefore, this chapter presents a study to establish a correlation between Charpy energy and the XFEM damage parameters. The findings of this chapter are expected to provide pipeline operators with valuable guidance for selecting appropriate XFEM damage parameters based on known Charpy V-Notch impact energy values.

Keywords: Pipelines; fracture toughness; Charpy energy; XFEM; failure pressure.

List of abbreviation

API	American Petroleum Institute
ASME	American Society of Mechanical Engineers
CMOD	Crack mouth opening displacement
CSA	Canadian Society Association
CT	Compact tension

CTOD	Crack tip opening displacement
CVN	Charpy-V-notch impact energy
CZM	Cohesive zone model
DOF	Degree of freedom
EPFM	Elastic plastic fracture mechanics
FEA	Finite element analysis
FEM	Finite element method
LEFM	Linear elastic fracture mechanics
MAXPE	Maximum principal strain
MAXPS	Maximum principal stress
MAXS	Maximum nominal stress
MAXE	Maximum nominal strain
PRCI	Pipeline Research Council International
QUADS	Quadratic nominal stress
QUADE	Quadratic nominal strain
RP	Reference point
SCC	Stress corrosion cracking
SENB	Single-edge notch bending
TSL	Traction-separation law
VCCT	Virtual crack closure technique
XFEM	Extended finite element method

Nomenclature

A_c	Net cross-sectional area of Charpy specimens

a	Crack depth
CVN	Charpy-V-notch impact energy
E	Young's modulus
G_C	Fracture energy
$H_{RO,}n_{RO}$	Dimensionless fitting parameters
J	J-Integral
J_c, K_c	Fracture toughness of material
K	Stress intensity factor
L	Crack length
t	Pipe wall thickness
Δa	Crack extension
σ	True stress
σ_{eng}	Engineering stress
σ_{YS}	Yield strength
σ_{UTS}	Ultimate tensile strength
ε	True strain
ε_{eng}	Engineering strain
$\mathcal{E}^{o}_{max}$	Maximum allowable principal strain

5.1 Introduction

Pipelines are designed, constructed and installed in accordance with national standards such as the Canadian Society Association (CSA) [1] or the American Society of Mechanical Engineers (ASME) [2] to convey natural gas and liquid petroleum products (e.g. crude oil and fuels). To date, most pipelines used by the pipeline industry are constructed according to the standard promulgated by the American Petroleum Institute (API) [3]. During its service life,

anomalies can threaten the structural integrity. Among the existing pipeline integrity threats including cracking (often found in pipe bodies, seam welds, or hard spots), corrosion, mechanical damage (e.g., plain dents and dents with gauges), and pipeline displacement (due to ground movement), cracking is the most severe threat to the oil and gas pipeline integrity. Compared to circumferential cracking (induced by axial stress), axial cracking is more critical as it can propagate quickly along the length of the pipe once it initiates [4]. Over the years, various fracture mechanics-based models, like Log-Secant and CorLAS^{TM} models, were developed to predict the failure of pipelines with axial cracking defects to ensure safe and reliable pipeline operation. Such fracture mechanics models are typically expressed in terms of the driving force (function of applied stress and crack size) and material resistance (or fracture toughness), which is a material property that describes the material's ability to resist fracture [5].

The stress intensity factor (K) and J-integral are two common parameters that characterize crack driving force. The former, proposed by Irwin [6] in 1957, describes the stress state at the tip of a crack for elastic materials. The critical value of the stress intensity factor at failure is a measure of fracture toughness, designated as K_C. The latter, originally proposed by Rice [7] in 1968, characterizes the stress state in the crack front zone for elasto-plastic materials in the presence of significant plastic deformation at the crack tip, and the corresponding fracture toughness is denoted as J_C. Failure is predicted to occur when the driving force exceeds the material resistance. The crack is expected to grow after the driving force at the crack tip exceeds a critical value, aka fracture toughness, which can be inferred from the materials testing. Therefore, crack driving force and fracture toughness comprise a whole fracture mechanics model, and they both play a vital role in the risk assessment for fractures.

In the 1970s, a project sponsored by Pipeline Research Council International (PRCI) [8] was launched at the Battle Memorial Institute to develop a K-based fracture mechanics model, known as the NG-18 approach or the Log-Secant (Ln-Sec) model, for evaluating the failure pressure of pipelines with a crack or crack-like defects. In the model, the fracture toughness (K_c) is calculated based on the Charpy-V-Notch impact energy (CVN) using the correlation proposed by Kiefner et al. [8] as follows:

$$K_c = \sqrt{\frac{12\ CVN}{A_c} E} \tag{5-1}$$

In the above equation, E is the Young's modulus (typically 29500000 psi for API steel pipe [9]), CVN is the energy required to break a Charpy specimen with a machined V-notch, and it is also called Charpy energy (ft-lb) measured from Charpy impact test, a factor of 12 converts the unit feet to inch. A_c is the net cross-sectional area for the Charpy specimen, i.e., the area for a full-sized Charpy specimen is 0.124 in^2 and 0.08 in^2 for a 2/3-sized specimen.

In 1996, Jaske and Beavers [10] developed an elastic-plastic fracture mechanics (EPFM)-based model for predicting the burst capacity of pipelines with corrosion or stress corrosion cracking (SCC), which is now referred to as the CorLAS^{TM} model. The model was updated in 2002 by the same authors [9]. In the latest version, failure due to a crack-like flaw is evaluated based on two independent criteria: the flow-strength criterion and fracture-toughness criterion. Whichever failure criterion gives the lower failure stress is predicted to control the failure. In the fracture toughness criterion, the failure stress is determined by iteratively calculating the *J*-integral until the applied value equals or exceeds the critical *J*-integral (J_c). However, the values of J_c are often unavailable in practice; in this case, *J* fracture toughness is estimated using the CVN - K_c relationship that Kiefner [8] originally developed for the Ln-Sec model (Eq. (5-1)), where K_c is replaced by J_c based on the following correlation [11]:

$$J_c = \frac{{K_c}^2}{E} \tag{5-2}$$

Substitute Eq. (5-1) into Eq. (5-2), the CVN - J_c relationship is established as follows:

$$J_c = \frac{12\ \text{CVN}}{A_c} \tag{5-3}$$

Besides fracture mechanics models, the crack initiation and propagation criteria can also be defined using a numerical approach such as the extended finite element method (XFEM). Two distinct damage modelling approaches are available within the XFEM framework: linear elastic fracture mechanic (LEFM)-based and cohesive segment model (CZM)-based approaches. The LEFM-based approach uses the virtual crack closure technique (VCCT) to calculate the strain energy release rate at the crack tip, and the damage properties are specified via the interaction property [12]. The CZM approach adopts the traction-separation laws (TSL). The shape of the softening law can be linear (by default) or exponential [12]. One big difference between these two XFEM-based approaches is that the CZM-based approach is suitable to model both brittle and

ductile fractures, whereas the LEFM-based approach is only recommended to model brittle fractures.

Recall that fracture mechanics models determine the failure based on fracture toughness, i.e., failure is predicted when the crack driving force (K or J-integral) value exceeds the corresponding fracture toughness (K_c or J_c), typically obtained from laboratory testing such as single-edge notch bending (SENB) or compact tension (CT) tests. However, these tests are relatively complex and expensive; as a result, the data of K_c or J_c are often unavailable. In contrast, the Charpy test is low-cost and can be performed without sophisticated laboratory equipment. In the absence of fracture toughness data, the values of fracture toughness, i.e., K_c or J_c, are often estimated from the Charpy V-notch impact energy data using empirical formulations. Several empirical correlations exist for predicting fracture toughness as a function of Charpy energy. Apart from the previously mentioned correlations, another widely used relationship between K_c and CVN is derived from the work of Rolfe, Novak, and Barson [13-14]. This correlation is based on numerous experimental measurements, establishing a linear correlation between the square of the K toughness-yield strength ratio and the ratio of Charpy energy to yield strength.

In the XFEM-based cohesive segment approach, failure is governed by two key damage properties, which the user defines as part of material property. Traditionally, the XFEM damage parameters were selected by fixing one parameter and adjusting the other until the numerical predictions matched well with the experimental tests [15-16]. This determination process, while effective in achieving accurate results, often incurs high computation costs. It is reasonable to assume that a relationship exists between the toughness properties and XFEM damage properties. Still, no effort has been made to establish a correlation between fracture toughness and XFEM damage properties for modelling crack propagation in pipelines. Such a correlation would enable the direct selection of damage parameters without re-calibration, offering significant computation cost savings. However, before attempting to develop such a correlation, it is imperative first to gain insight into how these XFEM damage parameters influence the failure pressure predictions. Thus, one objective of this chapter is to understand which one of the damage parameters has a more pronounced impact on the results. The other objective is to explore the relationship between the Chary impact energy and the validated XFEM damage parameters. To the best of the authors'

knowledge, this work is the first rigorous attempt to link the CVN impact energy and the XFEM damage properties.

The organization of this chapter is as follows: First, the implication of the chosen XFEM parameters on the fracture behavior of cracked pipes is studied to identify the most influential parameter, serving as the basis for the correlation development. Then, a comprehensive database is compiled, including the burst test data of pipes with axial surface cracks collected from open literature. Next, the XFEM models are calibrated and validated by comparing the predictions with the actual failure pressures. Lastly, statistical analyses are carried out to evaluate the performance of XFEM, with input damage parameters selected based on the established correlations.

5.2 Methodology

5.2.1 XFEM-based Cohesive Segment Approach

In 1999, Belytschko and Black [17] proposed the extended finite element method (XFEM) based on the idea of partition of unity introduced by Melenk and Babuska [18] to model crack propagation. Special enrichment functions (Heaviside enrichment and crack-tip enrichment functions) are introduced to the standard finite element method (FEM) formulation to model cracks that are not aligned with the finite element mesh. The addition of the extra enrichment functions overcomes the main FEM constraint, in which the crack can only propagate along a predefined path (element boundaries), typically with very fine meshes at the crack front. The ease of modelling as compared to the conventional method is pretty evident. Within the XFEM framework, the level set method (LSM) is used to locate the crack, which is accomplished by means of two orthogonal level set signed distance functions: ψ represents the crack surface, and φ denotes the crack front or tip [12]. It should be noted that although the capability of XFEM features in ABAQUS does allow the crack to be initiated in an intact region, a pre-existing crack is often used in the numerical simulation to reduce the computation cost [12].

As shown in **Figure 5-1**, the XFEM displacement function consists of two distinct parts, the first part is from FEM that is used in most of the domain, and the second part is the enriched elements used in the crack domain. The crack tip function accounts for crack tip singularity and applies to the nodes corresponding to the elements cut by the crack tip. Heaviside function accounts

for the displacement jump across the crack surface and applies to the nodes whose shape functions are separated by the interior of a crack. When modelling moving cracks using XFEM, two assumptions are made [12]:

- The crack-tip function is not considered; only the displacement jump across the crack surface is considered.
- In a time increment, the crack propagates through the whole element to avoid modelling the crack-tip singularity.

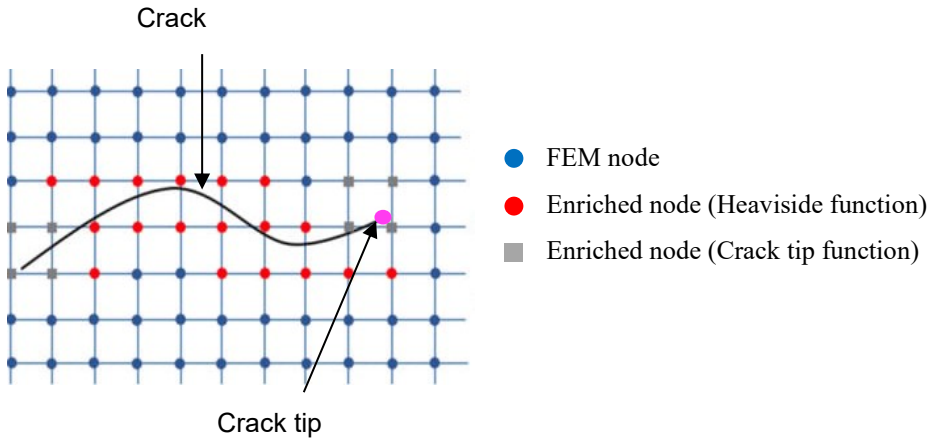

Figure 5-1: XFEM function and enriched nodes in XFEM, adapted from [19]

This work adopted the XFEM-based CZM approach to characterize the crack initiation and propagation and was executed in Abaqus/Standard Version 2022 [20]. As shown in **Figure 5-2**, the failure mechanism of the CZM approach consists of a damage initiation criterion and damage evolution law. Damage is predicted to occur when traction reaches the critical value. Once the damage initiation criterion is satisfied, traction reduces linearly to zero, resulting in complete separation. Damage evolution law can be defined either based on the energy dissipated due to fracture (per unit area), aka fracture energy (G_c) which is equivalent to the area under the TSL curve or the effective plastic displacement (δ_f) at failure. Three stress-based and three strain-based built-in damage initiation criteria are available in ABAQUS:

- Maximum principal stress (MAXPS)
- Maximum principal strain (MAXPE)

- Maximum nominal stress (MAXS)
- Maximum nominal strain (MAXE)
- Quadratic nominal stress (QUADS)
- Quadratic nominal strain (QUADE)

The built-in model employed in this study is the MAXPE criterion, which is defined as:

$$f = \left\{\frac{\varepsilon_{max}}{\varepsilon^{o}_{max}}\right\} \tag{5-4}$$

Herein, ε_{max} denotes the maximum principal strain and ε^{o}_{max} designates the maximum allowable principal strain. Damage takes place when the maximum principal strain ratio reaches one [12]. Additionally, a variable criterion can be specified in the user subroutine UGMGINI to characterize the onset of crack, as discussed in Lin et al. [21]. In this study, the crack grows orthogonally to the maximum principal strain and the crack propagation criterion is defined in terms of the fracture energy.

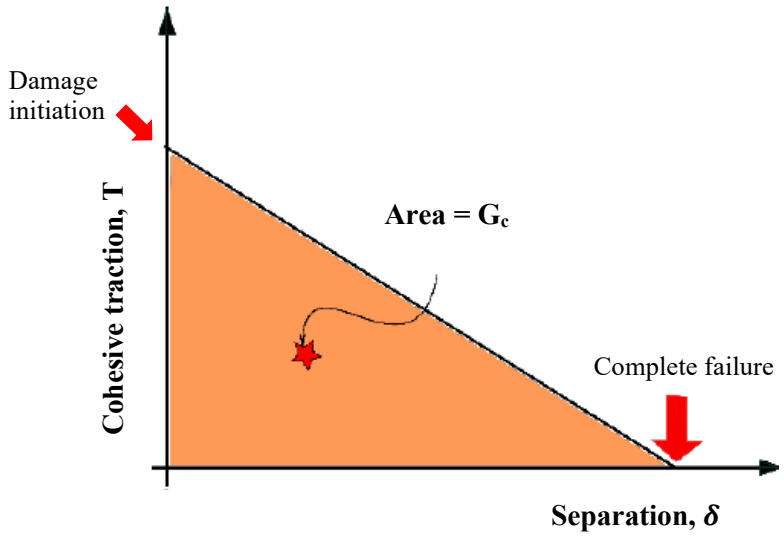

Figure 5-2: TSL curve, adapted from [22]

5.2.2 Fracture Toughness Parameters

For evaluating the fracture behavior of materials, crack mouth opening displacement (CMOD) and crack tip opening displacement (CTOD) are the two critical fracture toughness parameters. The concepts of CTOD and CMOD were conceived after the Second World War and

envisaged by Wells [23] from the British Welding Research Association in 1963. Typically, CTOD is defined either as the displacement of the deformed crack at the original crack tip or the displacement at the intersection of a 90° vertex with the crack flanks (as shown in **Figure 5-3** (a)) [24]. While performing numerical simulations in ABAQUS software, CTOD is the displacement near the original crack tip, and CMOD is measured as the nodal distance between the two nodes on the upper faces, as depicted in **Figure 5-3** (b) [22].

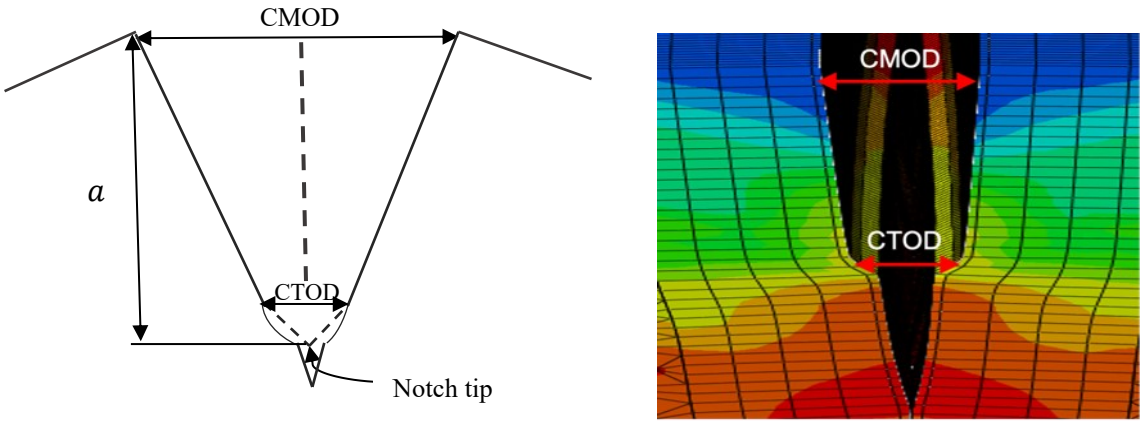

(a) (b)

Figure 5-3: Measurements of CTOD and CMOD: (a) Test (b) Simulation, adapted from [22]

5.3 Results and Discussion

5.3.1 Effect of XFEM Damage Parameters on Failure Pressure Predictions

As mentioned in **Section 5.1**, determining damage parameters often incur high computation costs in previous studies. In simpler terms, the two damage parameters are calibrated by keeping one constant (with the value chosen based on experience) and changing the other until a satisfactory agreement between the numerical predictions and the tests is achieved. Before attempting to establish the correlation between the XFEM damage parameters and the Charpy energy, it is essential to investigate how these two damage parameters affect the predicted failure pressures.

Prior work [22] explored the impact of the crack shape (rectangular-shaped sharp crack and blunted crack) on the ductile fracture response of pipelines with pre-existing cracks. The findings indicated minimal difference between a sharp crack and a blunted crack. However, a limitation in [22] is the exclusion of a semi-elliptical crack profile. In the absence of a detailed profile of a naturally-occurring crack (typically irregular in shape), most fracture mechanics models assume the surface crack has an idealized shape, such as a rectangle or semi-ellipse (as depicted in **Figure 5-4**). For example, the Log-Sec model uses the assumed rectangular shaped crack geometry, while the CorLAS^{TM} model treats the crack as having a semi-elliptical profile. Likewise, when conducting burst tests on pipe specimens, the machined (or artificially-induced) cracks are typically in semi-elliptical shape with varied depth or rectangular shape with uniform depth. Consequently, parametric studies are deemed necessary to examine the impact of the XFEM damage parameters on the ductile fracture response of cracked pipelines, considering different crack profiles so that the established correlations can account for differences in crack shape profiles.

The same pipe attributes as in previous parametric study [22] are adopted here. Specifically, the pipe outside diameter (D) is 508 mm, and the wall thickness (t) is 5.7 mm. The true stress-strain curve of the API X60 pipeline steel is retrieved from Hosseini et al. [25], where the true stress-strain data are obtained using the Ramberg-Osgood equation Eq. (5-5) [26].

$$\varepsilon = \frac{\sigma}{E} + \alpha \left(\frac{\sigma}{\sigma_{YS}}\right)^{n} \left(\frac{\sigma}{E}\right) \tag{5-5}$$

In the above equation, E is taken as 207 GPa, σ_{YS} is the yield strength with the value of 433 MPa, α and n are equal to 2.29 and 7.31, respectively, determined from curve-fitting to the tensile test data. The true stress-strain curve is illustrated in **Figure 5-5**. The defects are placed in the middle along the axial direction and modelled with a depth (a) of 0.3 mm (52% WT) and a length (L) of 200 mm.

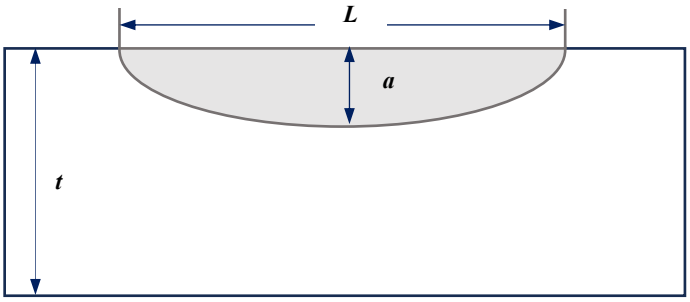

(a) Semi-elliptical crack

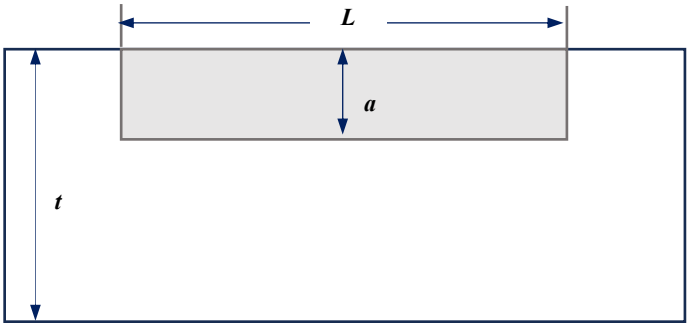

(b) Rectangular crack

Figure 5-4: The longitudinal profile of a surface crack

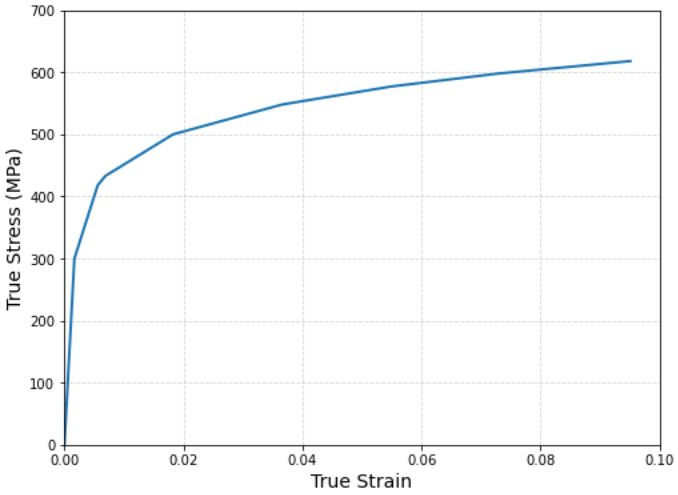

Figure 5-5: True stress-strain curve of X60 pipe [25]

The effect of G_c on the ductile fracture behavior of cracked pipes is first studied by considering different crack profiles (rectangular (R) and semi-elliptical (S)). **Figure 5-6** illustrates the impact of G_c on the load-Δa curve. As G_c increases from 50 N/mm to 400 N/mm while keeping the same maximum allowable principal strain value (MAXPE = 0.025), the load exhibits positive correlation to both Δa and G_c. This is reasonable considering the crack propagation criterion is governed by G_c; an increase in G_c results in an increase in the load, as discussed in [22]. Notably, significant increases in the load are observed for both crack profiles when G_c increases from 50 N/mm to 300 N/mm, while the increase in load becomes subtle as G_c increases from 300 N/m to 400 N/mm.

The load versus CMOD and CTOD curves using different G_c values with S and R-shaped cracks are presented in **Figure 5-7** and **Figure 5-8**, respectively. Similarly, the curves demonstrate higher sensitivity at lower fracture energy (below 300 N/mm). **Figure 5-9** shows the crack opening displacement (CTOD and CMOD) versus Δa for different crack profiles (R and S) and G_c values. It reveals that both factors, the crack profiles and G_c, pose insignificant effects on the relationship between displacement and crack extension.

Unsurprisingly, the semi-elliptical crack exhibits a higher failure pressure than the rectangular crack when using the same set of damage parameters, and this is attributed to the smaller crack area. This observation aligns with the findings from Bedairi et al. [27], who compared the predicted burst pressures of pipes with both semi-elliptical and rectangular cracks. The semi-elliptical crack yielded a higher burst pressure than the crack with a uniform depth profile. The authors reckoned that the reason is due to the fact that more material was removed from the crack shoulders. Similarly, Jaske et al. [28] and Yan et al. [29] compared the failure pressures associated with the semi-elliptical and rectangular crack profiles using finite element analysis (FEA) against the experimental test data. Both their results showed that the semi-elliptical idealization of natural cracking led to more accurate failure pressure predictions than the rectangular idealization of crack.

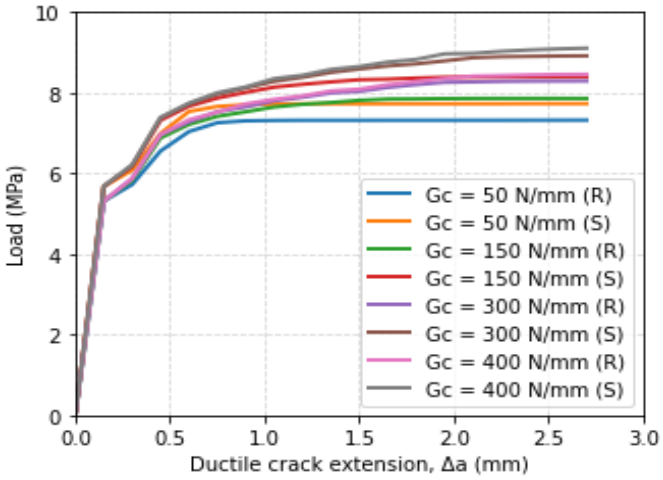

Figure 5-6: Effect of fracture energy on Load-Δa curve

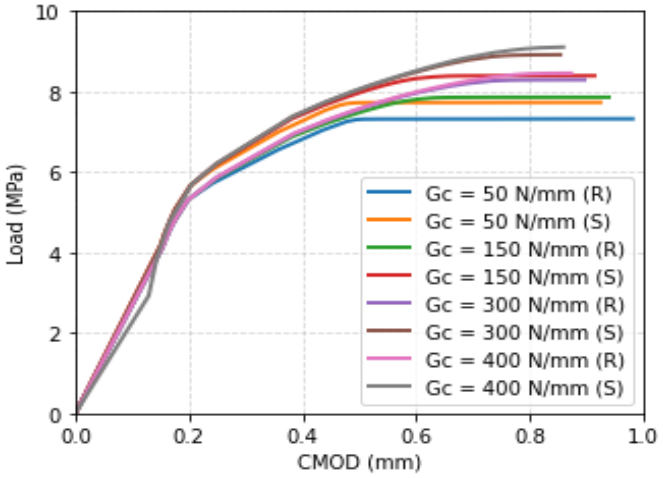

Figure 5-7: Effect of fracture energy on Load-CMOD curve

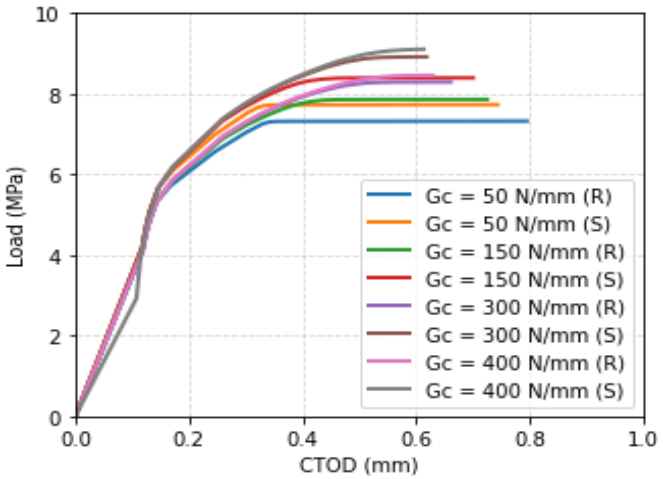

Figure 5-8: Effect of fracture energy on Load-CTOD curve

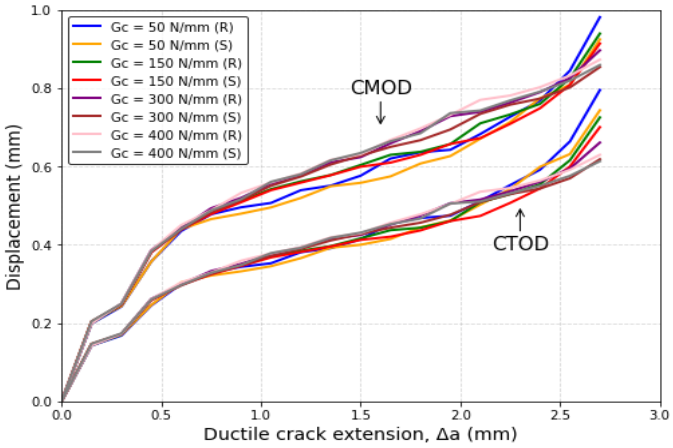

Figure 5-9: Effect of fracture energy on Displacement-Δa curve

Subsequently, the impact of the MAXPE is explored, considering two initial sharp crack profiles with a constant G_c of 300 N/mm. As depicted in **Figure 5-10**, the load increases as the crack grows and increases with the increase of the maximum allowable principal strain, consistent with the findings reported in prior work [22]. Once the ductile crack extension approaches approximately 30% of the remaining ligament (i.e., 0.9 mm), the further load increase with Δa becomes relatively insensitive to changing the maximum allowable principal strain.

The variations of the crack opening displacements (CTOD and CMOD) on the load, from the onset of crack initiation until complete fracture, are presented in **Figure 5-11** and **Figure 5-12**. As the crack opening displacements increase, the load continues to increase. At the beginning of crack opening (i.e., CMOD and CTOD $<$ 0.2 mm), the load-displacement curves for semi-elliptical and rectangular cracks are almost identical. Beyond this point, the crack opening displacements at a given load for the rectangular crack are larger than those for the semi-elliptical crack, as expected. Interestingly, when the MAXPE value increases from 0.015 to 0.03, the load-displacement curve for each crack profile seems to be identical up to a CMOD of 0.6 mm and a CTOD of 0.4 mm.

In comparison to the maximum allowable principal strain, it is noted that failure pressure is more sensitive to changing the value of G_c. This observation aligns with findings reported in [22], where different combinations of XFEM damage parameters were employed to predict the

ductile fracture response of pipes with two crack shapes (rectangular crack and notch). Generally speaking, G_c is a more influential factor in predicting the failure pressure.

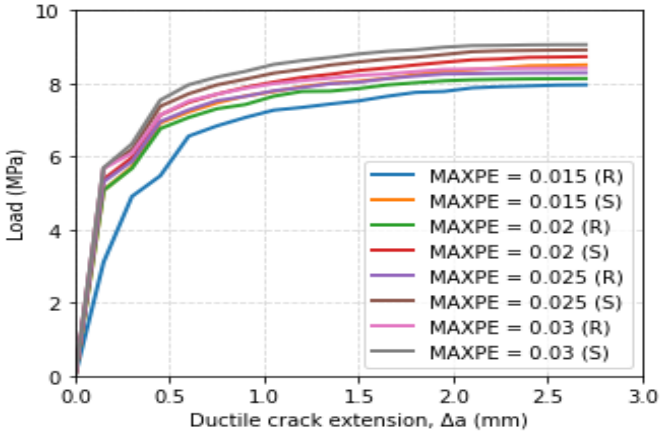

Figure 5-10: Effect of maximum allowable principal strain on Load-Δa curve

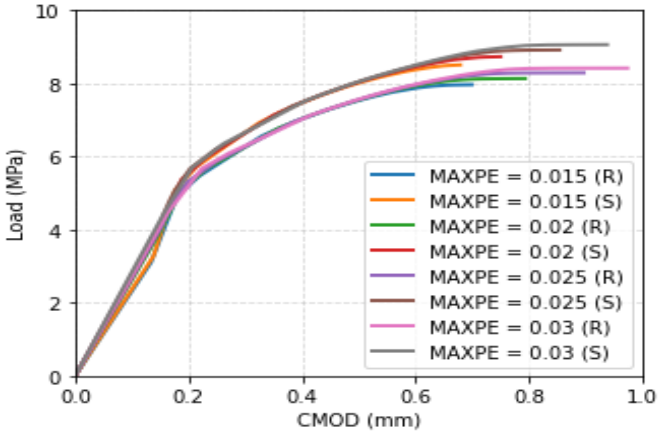

Figure 5-11: Effect of maximum allowable principal strain on Load-CMOD curve

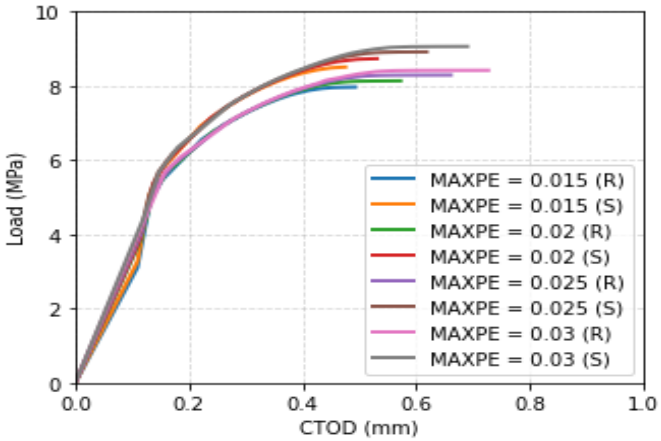

Figure 5-12: Effect of maximum allowable principal strain on Load-CTOD curve

5.3.2 Development of the Correlation

5.3.2.1 Full-scale Burst Test Data Collection

A large database containing full-scale burst test data of pipelines with surface cracks is collected from the open literature according to the following criteria:

(1) Thin-walled pipes: a pipe-outer-diameter to pipe-wall-thickness ratio ($\frac{D}{t}$) equal to or greater than 20 [30]. Thick-wall pipes ($\frac{D}{t} < 20$) are not considered.

(2) Crack orientation and location: only cracks oriented in the axial direction and located on the outer surface of the pipe specimens with idealized profiles are included.

(3) Sufficient material property information: tests with incomplete material property information, particularly Charpy energy data, are excluded from the database. For example, Kiefner et al. [8] reported 48 test data, but only 36 tests were reported with Charpy data. Similarly, *CVN* values were missing for two tests by Keller et al. [35]. Likewise, a total of 62 test data were reported by Rana et al. [36]; however, Charpy data of 15 tests are unavailable.

(4) Loading condition: the database contains data from burst tests conducted on the pipes only subjected to internal pressure.

The ranges of the pipe geometry (i.e., pipe diameter and pipe wall thickness), normalized crack depth (the crack depth-to-pipe wall thickness ratio), normalized crack length (the square of crack length over pipe diameter times wall thickness) as well as the material properties are summarized in **Table 5-1**. Details and references of all the test data are tabulated in **Appendix C** [8, 31-36].

Table 5-1: Ranges of characteristics of the test data

Parameters	Unit	Range	
		Min	Max
Diameter, D	mm	178	1422.4
Wall thickness, t	mm	4.93	21.8
Crack depth-to-wall thickness ratio, a/t	-	0.19	0.89
Squared of crack length-to-multiplication of diameter and wall thickness ratio, $L^2/(Dt)$	-	0.12	33.28
Yield strength, σ_{YS}	MPa	341.29	890
Ultimate tensile strength, σ_{UTS}	MPa	410.94	990
Charpy V-notch impact energy, CVN	J	10.8	261

5.3.2.2 Materials

When modelling elastic-plastic materials, a stress-strain relationship is required as part of the material property input in FEA using ABAQUS/CAE [20]. Ideally, data recorded from tensile testing should be used to describe the stress-strain curve where the stress-strain behavior of pipeline steel is expressed using a power-law equation. Since the stress-strain curve obtained from the tensile coupon test is usually reported in terms of engineering stress and engineering strain, the true stress (σ) and true strain (ε) are converted from the engineering values up to the onset of necking using the following equations:

$$\varepsilon = \ln(1 + \varepsilon_{eng}) \tag{5-5}$$

$$\sigma = \sigma_{eng}(1 + \varepsilon_{eng}) \tag{5-6}$$

The Ramberg-Osgood equation (Eq. (5-4)) is widely used to characterize the stress-strain behavior of pipeline steel. In Eq. (5-4), σ_{YS} is defined by the 0.2% offset method or as the stress corresponding to a total strain of 0.005. The two dimensionless parameters, α and n, are typically determined through non-linear curve-fitting to the stress-strain test data, as discussed in our previous paper [36].

However, stress-strain data are often unavailable for most pipeline steels [33]. In fact, all the literature collected in this study did not report actual stress-strain data; only the yield strength (σ_{YS}) and ultimate tensile strength (σ_{UTS}) were provided. In the absence of coupon test data, the following simplified approach via a modified Ramberg-Osgood equation, as suggested in API579-1/ASME FFS-1 [38], was employed to construct the stress-strain curve in the current FEA:

$$\varepsilon = \frac{\sigma}{\mathrm{E}} + \left(\frac{\sigma}{H_{\mathrm{RO}}}\right)^{\frac{1}{n_{\mathrm{RO}}}} \tag{5-7}$$

$$n_{\mathrm{RO}} = \frac{1+1.3495\left(\frac{\sigma_{YS}}{\sigma_{UTS}}\right)-5.3117\left(\frac{\sigma_{YS}}{\sigma_{UTS}}\right)^2+2.9643\left(\frac{\sigma_{YS}}{\sigma_{UTS}}\right)^3}{1.1249+11.0097\left(\frac{\sigma_{YS}}{\sigma_{UTS}}\right)-11.7464\left(\frac{\sigma_{YS}}{\sigma_{UTS}}\right)^2} \tag{5-8}$$

Given the value of n_{RO}, H_{RO} can be estimated using the following expression:

$$H_{\mathrm{RO}} = \frac{\sigma_{UTS}\exp(n_{RO})}{{n_{RO}}^{n_{RO}}} \tag{5-9}$$

5.3.2.3 XFEM Model in ABAQUS

As the first attempt, the initial crack is simulated with a rectangular profile in the current numerical analysis. As shown in **Figure 5-13** (a), a symmetric boundary condition is applied at the Z-axis with internal pressure (the only loading) being applied gradually at the inner surface of the pipe, while the remote end is fixed to a reference point (RP) using kinematic coupling. Because the mesh size can deeply impact the results of the analyses, it is selected based on a mesh convergency study conducted in [4]. Fine mesh is applied at the crack tip proximity and coarse mesh is applied away from the crack region. The pipe domain is meshed using 3D 8-noded reduced integration solid elements (Abaqus element "C3D8R"). An appropriate gradient is used in the transition area from coarse mesh to fine mesh (**Figure 5-13** (b)).

An attempt is made to establish a correlation between the Charpy energy and the two XFEM damage properties (MAXPE and G_c). The parametric study results in **Section 5.3** highlighted that G_c has a more pronounced impact on predicted failure pressures. As a result, MAXPE is initially set at a low value of 0.01 when modelling pipes with low toughness values, gradually increasing the value for modelling high toughness pipes. The G_c value is continuously adjusted until a satisfactory agreement is reached between predictions and test data. For instance, when reproducing the first eleven tests in [8], the initial values for MAXPE and G_c are chosen as 0.01 and 50 N/mm, respectively, considering that the Charpy energies for these tests fall within the range of 35 to 40 J.

Figure 5-14 illustrates the variation of MAXPE on the Charpy energy. A higher CVN value corresponds to a higher maximum principal strain – a higher MAXPE value is needed to match the test data with high CVN values. Specifically, MAXPE values ranging from 0.01 to 0.015 are recommended for low CVN values below 100 J and a value of 0.02 for high CVN values over 130 J. As anticipated, a noticeable variation is observed in the CVN versus fracture energy curve, particularly in the low toughness region (**Figure 5-15**). The suggested values of G_c are in the range of 10 to 100 N/mm for CVN values below 100 J. In the relatively high toughness regime (CVN above 130 J), adopting G_c as 150 N/mm is recommended.

Overall, while the Charpy energy is relatively insensitive to the MAXPE damage parameter since the MAXPE value only ranges from 0.01 to 0.02 corresponding to a large range of CVN

values (10 to 270 J), it appears to be highly sensitive to fracture energy, which will be further investigated.

In the current XFEM model, failure is defined when the crack penetrates the entire pipe wall (i.e., ligament). The failure pressures are predicted using the XFEM damage parameters based on the aforementioned selection criteria, and the comparison between the XFEM predictions and the reported test results is demonstrated in **Figure 5-16**. Satisfactory agreement can be achieved between the predicted failure pressures and the reported test pressures.

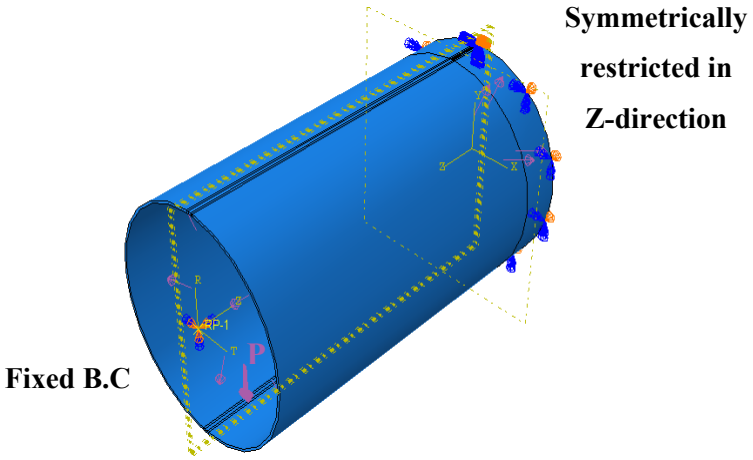

(a)

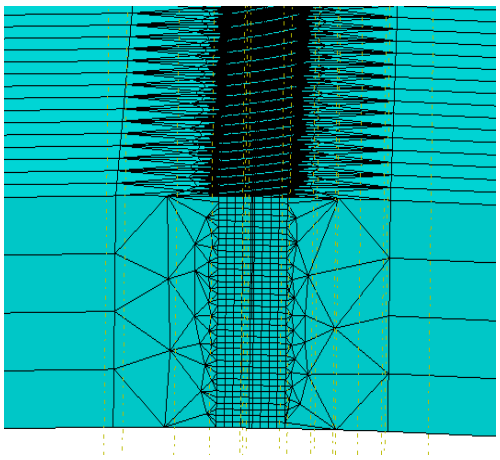

(b)

Figure 5-13: Half pipe model: (a) Boundary and loading conditions applied on the model (b) Meshed geometry at the crack region

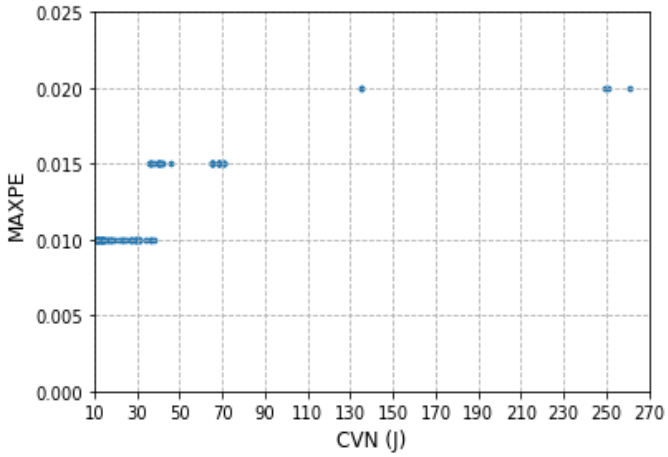

Figure 5-14: Variation of the maximum allowable principal strain with Charpy energy – XFEM using rectangular crack profile

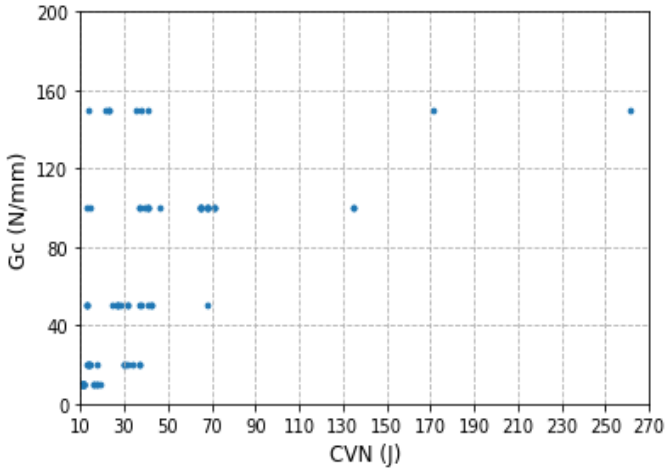

Figure 5-15: Variation of the fracture energy with Charpy energy – XFEM using rectangular crack profile

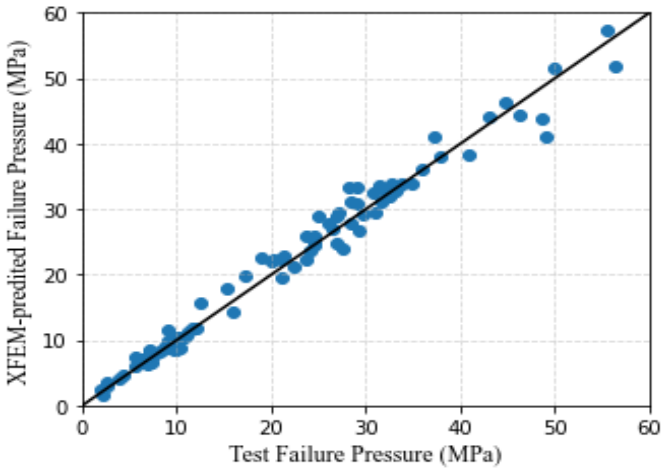

Figure 5-16: Comparison of the XFEM-predicted and test failure pressures – XFEM using rectangular crack profile

As expected, treating cracks as rectangular shapes for simplicity results in unsatisfactory correlations. While some success is achieved in establishing a relationship between the Charpy impact energy and the maximum allowable principal strain, the correlation between the Charpy energy and the fracture energy is unsatisfactory—no distinct trend could be identified. The reason could be attributed to the noticeable difference in the pressure at failure between a semi-elliptical crack and a rectangular crack. Therefore, it is important to select a crack profile that closely represents the actual tests. In the following section, a further attempt is made to establish a correlation between the Charpy energy and two XFEM damage properties. It is worth mentioning that a semi-elliptical crack profile is employed to replicate tests from references [33-36], while a rectangular crack profile is adopted to predict the failure pressures for tests in [8, 31-32].

Similar to the correlation development procedures described using the rectangular-shaped crack, MAXPE is initially set at a low value of 0.01 for modelling low toughness pipes, and G_c is kept changing until a good agreement between the predictions and tests is achieved. The variations of the maximum allowable principal strain and fracture energy with Charpy energy are shown in Figure 5-17 and Figure 5-18. As observed in **Figure 5-17**, an MAXPE value of 0.01 corresponds to the low toughness region with CVN values lower than 70 J, whereas an MAXPE value of 0.015 corresponds to the high toughness region (CVN > 70 J). **Figure 5-18** presents the relationship between the Charpy energy and G_c. Specifically, recommendations include:

$$G_c\,(\text{N/mm}) = \begin{cases} 10, & CVN < 20\ \text{J} \\ 20, & 20\ \text{J} \le CVN < 35\ \text{J} \\ 50, & 35\ \text{J} \le CVN < 70\ \text{J} \\ 100, & CVN \ge 70\ \text{J} \end{cases}$$

Overall, the Charpy energy is proportional to MAXPE and G_c but exhibits higher sensitivity to G_c. Consequently, higher values of MAXPE and G_c are recommended for pipes with high toughness values. The results of XFEM predictions based on the newly established guidelines are shown in **Figure 5-19**. The 45° solid line (i.e., 1:1 line) serves as a reference for a perfect correlation, with data points below the 1:1 line indicating conservative predictions (lower than test failure pressures) and data points above the 1:1 line representing over-predictions. As shown in Figure 5-19, XFEM-predicted and test failure pressures are in excellent agreement as most of the XFEM-predicted data align closely with the 1:1 line.

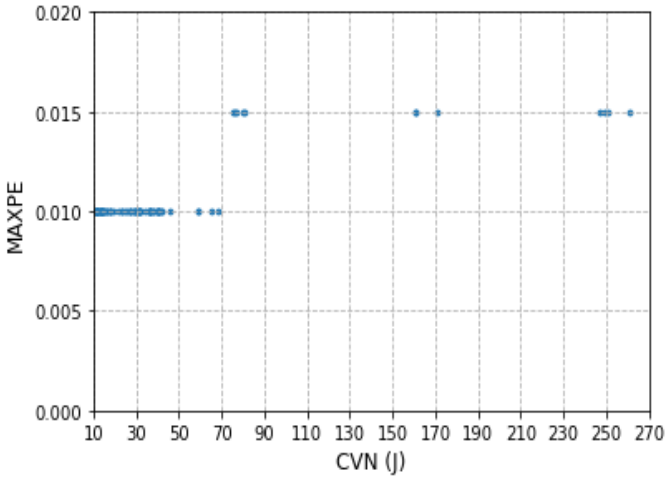

Figure 5-17: Variation of the maximum allowable principal strain with Charpy energy – XFEM using best matching crack profile

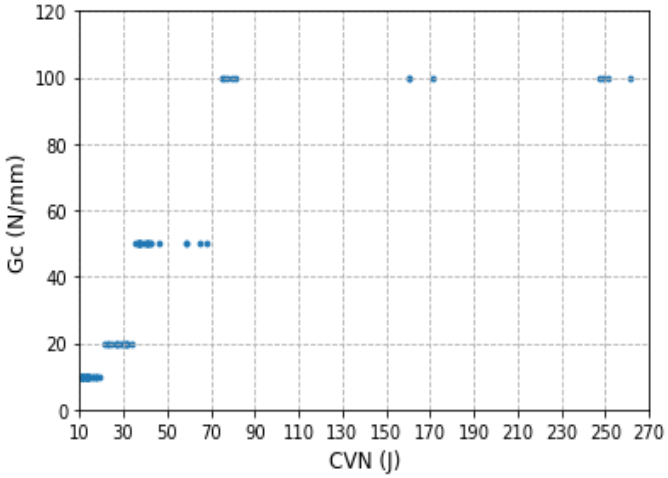

Figure 5-18: Variation of the fracture energy with Charpy energy – XFEM using best matching crack profile

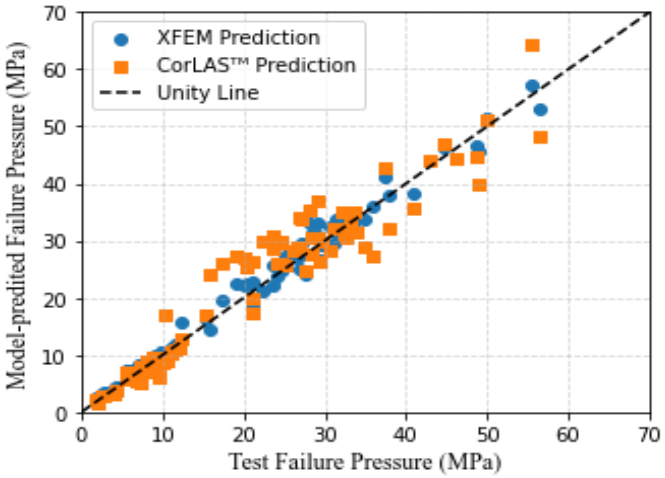

Figure 5-19: Comparison of the XFEM-predicted (using best matching crack profile), CorLAS-predicted and test failure pressures.

Additionally, **Figure 5-19** also compares the results obtained using the CorLAS^{TM} model against data collected from the full-scale burst tests. As described previously, CorLAS^{TM} is a widely used fracture mechanics model for evaluating the failure pressure of pipelines with axial cracks based on two criteria, as expressed in Eq. (5-10). This model assumes an S-shaped profile if a detailed crack profile is unknown. However, when evaluating an R-shaped crack, a conversion is needed based on the effective area method.

$$P_f = min\{\sigma_f, \sigma_t\}\frac{2t}{D}\left(\frac{1-\frac{A_{eff}}{A_o}}{1-\frac{A}{MA_o}}\right) \tag{5-10}$$

In the above equation, P_f represents the failure pressure, σ_f and σ_t are the corresponding failure stress in the flow stress criterion and fracture toughness criterion, D and t are the pipe outer diameter and wall thickness, M denotes Folias factor, which is a function of crack length (L) and pipe geometry (D and t), A_o is the reference area and A_{eff} is the effective area. Detailed equations for calculating the failure stress in each failure criterion are summarized in **Appendix D**.

Model error (ε_m) is introduced here to evaluate the prediction capability of the model, defined as the ratio of the test versus the predicted failure pressure (referred to as the test-to-prediction ratio), expressed as:

$$\varepsilon_m = \frac{P_{test}}{P_{predicted}} \tag{5-11}$$

Here, P_{test} and $P_{predicted}$ denote the test failure pressure and predicted failure pressure, respectively.

A ratio larger than 1 ($\varepsilon_m > 1$) indicates a conservative prediction and a ratio equal to 1 ($\varepsilon_m = 1$) represents a perfect prediction. The probabilistic characteristics of model error considered here are mean and coefficient of variation (CoV), which respectively reflect the degrees of bias and dispersion of the predictions. The CoV is the ratio of the standard deviation (SD) to the mean. An ideal prediction model should have the average value of the test-to-prediction ratios closest to 1 and a small CoV.

XFEM demonstrates superior accuracy in failure pressure predictions, with a mean test-to-prediction ratio of 1.001 and CoV of 8.8%. In contrast, the CorLAS^{TM} model tends to under-predict

the burst capacity, with a mean and CoV of the test-to-prediction ratio equal to 1.02 and 16.9%, respectively. Clearly, XFEM is more accurate than the CorLAS^{TM} model, with the average model error closer to unity and a smaller bias.

Notably, the mean and CoV values for the CorLAS^{TM} model error reported in this study are fairly close to those from **Section 2.2.3** where the derived mean and CoV values were 1.07 and 13.9%, respectively. In this study, the database comprises the same dataset as in [39], supplemented with additional test data collected from the open literature. Similarly, Yan et al. [29] investigated the accuracy of the CorLAS^{TM} model by employing different crack profiles (rectangular, semi-elliptical, and actual profiles) based on 75 in-service or hydrostatic ruptures. Using the actual crack profile provided the most accurate predictions, with the model error mean and CoV equal to 1.11 and 14%, respectively. In the absence of a detailed actual profile, failure pressure predictions based on the assumption of the semi-elliptical profile gave more accurate predictions than those using the rectangular profile. The corresponding model error follows a normal distribution with a mean equal to 1.27 and a CoV of 16%.

Overall, the results demonstrate the capability of XFEM to provide satisfactory predictions when the input XFEM damage parameters are determined from the Charpy data.

5.4 Conclusions

This chapter presents an investigation of the correlation between the CVN energy and the XFEM damage parameters. The main findings from this chapter are summarized as follows:

- The crack profile significantly impacts the failure pressure predictions as the semi-elliptical crack yields a higher failure pressure than the rectangular crack, attributed to the smaller defect area.
- Failure pressure increases with the increase of the XFEM damage properties (i.e., fracture strain and maximum allowable principal strain).
- Compared to the maximum allowable principal strain, the ductile failure behavior of cracked pipes is more sensitive to fracture energy.
- XFEM can provide accurate predictions when the input damage properties are selected based on the correlation between the CVN and XFEM damage properties established in

this work.

The outcome of this chapter is expected to provide guidelines for assigning the appropriate set of XFEM damage parameters to numerical simulations on the premise of the availability of CVN data from Charpy testing. Due to the limited test data, most of the collected tests are conducted on low-toughness pipes (CVN < 100 J); more tests are needed to validate the relationship between the Charpy energy and XFEM parameters in the high-toughness regime.

References

[1] CSA. Oil and gas pipeline systems. CSA Standard Z662:19, Canada Standards Association, Mississauga, Ontario, Canada, 2019

[2] ASME B31.8-2010, Gas Transmission and Distribution Piping Systems.

[3] API. Specification for Line Pipe. ANSI/SPI Specification 5L/ISO 3183:2007, 44th Edition, October 1, 2007.

[4] Zhang, X. Lin, M., Okodi, A., Tan, L., Leung, J.Y. and Adeeb, S. Numerical analysis of API X42 and X52 vintage pipes with cracks in corrosion defects using extended finite element method. Paper No. PVT-20-1218, *Journal of Pressure Vessel Technology*, 143(6):061302, 2021.

[5] Anderson, T. Assessing crack-like flaws in longitudinal seam welds: a state-of-the-art review. PRCI Catalogue No. PR-460-134506-R02. Pipeline Research Council International, Chantilly, 2017.

[6] Irwin, G.R. Analysis of stresses and strains near the end of a crack traversing a plate. *Journal of Applied Mechanics*, 24:361–364, 1957.

[7] Rice, J.R. a path independent integral and the approximate analysis of strain concentration by notches and cracks. *Journal of Applied Mechanics*, 35:379–386, 1968.

[8] Kiefner, J.F., Maxey, W.A., Eiber, R.J. and Duffy, A.R. Failure stress levels of flaws in pressurized cylinders. Progress in flaw growth and fracture toughness testing, STP 536, *ASTM International*, West Conshohocken, PA, pp. 461-481, 1973.

[9] Jaske, C. E. and Beavers, J. A. Integrity and remaining life of pipe with stress corrosion cracking. PRCI 186-9709, Catalog No. L51928. Pipeline Research Council International, Falls church, 2001.

[10] Jaske, C.E., Beavers, J.A. and Harle, B.A. Effect of stress corrosion cracking on integrity and remaining life of natural gas pipelines, Paper No. 255, Corrosion 96, NACE International, Houston, 1996.

[11] Maxey, W.A., Kiefner, J.F., Eiber, R.J., Duffy, A.R. in *The Fifth National Symposium on Fracture Mechanics*, University of Illinois, 1971.

[12] Abaqus 6.14. Abaqus Analysis User's Guide, Dassault Systèmes, 2014.

[13] Barsom, J.M. and Rolfe, S.T. Impact Testing of Metals, ASTM STP 466, *The American Society for Testing and Materials (ASTM)*, Philadelphia, PA, 1970, pp. 281-302.

[14] Rolfe, S.T. and Novak, S.R. Review of developments in plane-strain fracture toughness testing. ASTM STP 463, *The American Society for Testing and Materials (ASTM)*, Philadelphia, PA, pp. 124-159, 1970.

[15] Zhang, X., Okodi, A., Tan, L., Leung, J.Y. and Adeeb, S. Failure pressure prediction of crack in corrosion defects using XFEM. Paper No. IPC2020-9312, *Proceedings of the 2020 13th International Pipeline Conference, American Society of Mechanical Engineers*, Virtual, Online, 2020.

[16] Zhang, X., Okodi, A., Tan, L., Leung, J.Y. and Adeeb, S. Failure pressure prediction of crack in corrosion defects in 2D by using XFEM. Paper No. PVP2020-21046, *Proceedings of the Pressure Vessel and Piping Conference, American Society of Mechanical Engineers*, Virtual, Online, 2020.

[17] Belytschko T. and T. Black. Elastic crack growth in finite elements with minimal remeshing. *International Journal for Numerical Methods in Engineering*, 45, 601-620, 1999.

[18] Melenk, J.M. and Babuška, I. The partition of unity finite element method: basic theory and applications. *Computer Methods in Applied Mechanics and Engineering*, 139(1-4): 289–314, 1996.

[19] Gairola, S and Ren, J. XFEM simulation of tensile and fracture behavior of ultrafine-grained AI 6061 alloy. *Metals*, 11(11):1761, 2021.

[20] Dassault Systèmes, 2022. Abaqus documentation.

[21] Lin, M., Li, Y., Cheng, J.J.R., Koduru, S., Kainat, M., Zhang, X. and Adeeb, S. Novel XFEM variable strain damage model for predicting fracture in small-scale SENT and full-scale pipe tests. *Engineering Fracture Mechanics*, 271(2):108628, 2022.

[22] Zhang, X., Yoosef-Ghodsi, N., Kainat, M., Leung, J.Y. and Adeeb, S. Comparative study of crack shape on the ductile fracture response of cracked pipelines. Paper No. PVP2024-121892, Forthcoming, *Proceedings of the Pressure Vessel and Piping Conference American Society of Mechanical Engineers*, Washington, USA, 2024.

[23] Wells, A.A. Application of fracture mechanics at and beyond general yielding. British Welding Research Association Report M13/63, *British Welding Journal*, 10:563–570, 1963.

[24] Samadian, K., Hertele, S. and Waele, W.D. Using 3D digital image correlation (3D-DIC) to measure CTOD in a semi-elliptical surface crack. *The Eighteenth International Conference of Experimental Mechanics*, 2(8):5311, 2018.

[25] Hosseini, A., Cronin, D., Plumtree, A. and Kania, R. Experimental testing and evaluation of crack defects in line pipe. Paper No. IPC2010-31158, *Proceedings of the 8th International Pipeline Conference, American Society of Mechanical Engineers,* Calgary, Canada, 2010.

[26] Ramberg, W and Osgood, W.R. Description of Stress-Strain Curves by Three Parameters. Technical Note No.902, National Advisory Committee For Aeronautics, Washington DC, 1943.

[27] Bedairi, B., Cronin, D., Hosseini, A. and Plumtree, A. Failure prediction for crack-in-corrosion defects in natural gas transmission pipelines. *International Journal of Pressure Vessels and Piping*, 96-97:90-99, 2012.

[28] Jaske, C.E., Polasik, S.J. and Maier, C.J. Inelastic fracture mechanics model for assessment of crack-like flaws. Paper No. PVP2011-57099, *Proceedings of the Pressure Vessels & Piping Conference, American Society of Mechanical Engineers*. Baltimore, Maryland, USA, 2011.

[29] Yan, J., Zhang, S., Kariyawasam, S., Pino, M. and Liu, T. Validate crack assessment models with in-service and hydrotest failures. Paper No. IPC2018-78251, *Proceedings of the 2018 12th International Pipeline Conference, American Society of Mechanical Engineers,* Calgary, Canada, 2018.

[30] PD 8010-1:2015: Pipeline systems. Steel pipelines on land. Code of practice 2015.

[31] Kawaguchi, S., Hagiwara, N., Masuda, T., Toyoda, M. Evaluation of leak-before-break (LBB) behavior for axially notched X65 and X80 line pipes. *Journal of Offshore Mechanics and Arctic Engineering*, 126 (4), 350–357, 2004.

[32] Mannucci, G. and Harris, D. Fracture Properties of API X 100 Gas Pipeline Steels: final report, European Commission, Directorate-General for Research and Innovation, Publication Office, 2002.

[33] Tandon, S., Gao, M., Krishnamurthy, R., Kariyawasam, S. and Kania, R, Evaluation of existing fracture mechanics models for burst pressure predictions, Theoretical and Experimental Aspects. Paper No. IPC2014-33563, *Proceedings of the ASME 2014 10th International Pipeline Conference*, *American Society of Mechanical Engineers,* Calgary, Canada, 2014.

[34] Keller, H.P., Junker, G. and Merker, W. Fracture analysis of surface cracks in cylindrical pressure vessels applying the Two Parameter Fracture Criterion (TPFC). *International Journal Pressure Vessels and Piping*, 29(2), 113-153, 1987.

[35] Rana, M.D., Smith, J.H., Tribolet, R.O. Technical basis for flawed cylinder test specification to assure adequate fracture resistance of ISO high-strength steel cylinder. *Journal of Pressure Vessel Technology*, 119 (4), 475-480, 1997.

[36] Zhang, X., Lin, M., Kainat, M., Yoosef-Ghodsi, N., Leung, J.Y. and Adeeb, S. Influence of strain hardening model on the CorLAS^{TM} model for cracked pipelines. Paper No. IPC2022-868556, *Proceedings of the 2022 14th International Pipeline Conference*, *American Society of Mechanical Engineers,* Calgary, Canada, 2022.

[37] API 579-1/ASME FFS-1, Fitness-for-service, American Society of Mechanical Engineers, USA, 2019.

[38] Zhang, X., Zheng, Q., Leung, J.Y. and Adeeb, S. Reliability-based assessment of cracked pipelines using Monte Carlo Simulation technique with CorLAS^{TM}. Paper No. PVP2022-80412, *Proceedings of the Pressure Vessel and Piping Conference, American Society of Mechanical Engineers*, Las Vegas, USA, 2022.

CHAPTER 6: AN ANN MODEL TO PREDICT FAILURE PRESSURE OF PIPELINES CONTAINING AXIAL SURFACE CRACKS

This chapter is derived from a research paper submitted for publication in the International Journal of Pressure Vessel and Piping:

Zhang, X., Li, Y., Yoosef-Ghodsi, N., Leung, J.Y. and Adeeb, S. An ANN model to predict failure pressure of pipelines containing axial surface cracks.

Abstract

The CorLAS^{TM} model is widely used in the pipeline industry for predicting the failure pressure of pipelines with axial surface cracks, primarily due to its simplicity and relatively higher accuracy compared to other alternative models. Despite its popularity, recent studies have reported that the CorLAS^{TM} model is associated with a high coefficient of variation (CoV) of model error, which can undermine the confidence in reliability-based assessment of burst pressure of pipelines using CorLAS^{TM}. Recently, machine learning (ML) techniques, such as artificial neural networks (ANN) have been successfully used to develop predictive models based on large data sets. However, the experimental tests are costly, rendering the burst test data scarce in the open literature and making developing ANN models based on experimental data infeasible. To address this issue, a sufficiently large database is generated using the extended finite element method (XFEM), which has proven to be a powerful yet effective approach to simulating crack growth. Parametric XFEM analyses are carried out to predict the failure pressure of cracked pipelines by varying several geometric parameters, including pipe size (outer diameter-to-thickness ratio) and crack size (crack depth and crack length). Based on the data generated from XFEM, an ANN model for evaluating cracked pipelines subjected to internal pressure is developed. The developed ANN model is further validated by 10 full-scale burst tests and the ANN predictions are compared with those computed using the CorLAS^{TM} model. With a model error mean of 1.01 and a CoV smaller than the CorLAS^{TM} model, the proposed ANN model gave less biased predictions and could serve as an alternative approach for predicting the failure pressure of pipelines with axial cracks.

Keywords: pipeline; XFEM; ANN; cracks; failure pressure; machine learning; model error

Nomenclature

A_{eff}	Effective area
A_o	Reference area
a	Crack depth
a/t	Crack depth-to-thickness ratio
D	Pipe outer diameter

D/t	Outer diameter-to-thickness ratio
E	Young's modulus
F_{sf}	Free surface factor
G_C	Fracture energy
$f_3(n)$	Shih and Hutchinson factor
L	Crack length
M	Folias factor
P_f	The failure pressure of cracked pipe
Q_f	Elliptical shape factor
R^2	Coefficient of determination
t	Pipe wall thickness
H_{RO}, n_{RO}	Fitting parameters in Ramberg-Osgood equation
σ	True stress
σ_f	Flow stress
σ_t	Local failure stress
σ_{YS}	Yield strength
σ_{UTS}	Ultimate tensile strength
ε	True strain
ε_p	Plastic strain
x_{min}	Data minimum value
x_{max}	Data maximum value
y_i	Actual value
$\overline{y_i}$	Predicted value
$\overline{y_a}$	Average of the actual value

Abbreviations

ANN	Artificial neural network
CEPA	Canadian Energy Pipeline Association
CoV	Coefficient of variation
CSA	Canadian Standards Association
CVN	Charpy V-notch impact energy
DNN	Deep neural network
EDM	Electric discharge machining
FAD	Failure assessment diagram
FEM	Finite element method
ILI	In-line inspection
LEFM	Linear elastic fracture mechanics
MAE	Mean absolute error
MAPE	Mean absolute percentage error
MAXPE	Maximum principal strain
ML	Machine learning
MRE	Mean relative error
MSE	Mean squared error
PAFFC	Pipe axial flaw failure criteria
PoF	Probability of failure
PUM	Partition of unity method
SCC	Stress corrosion cracking
XFEM	Extended finite element method

6.1. Introduction

Cracks or crack-like anomalies are commonly identified in pre-service or in-service pipes through inspection tools like in-line inspection (ILI). If left untreated, pipeline anomalies could significantly compromise the pipeline's structural integrity. Assessing the severity of cracks plays a key role in pipeline integrity management. Cracks can appear on the pipe's external or internal surfaces and in various orientations (e.g., inclined, axial, or circumferential). Numerous attempts have been made to assess pipeline integrity in the presence of axially aligned cracks, with the development of fracture models for predicting the failure pressure of pipelines with cracks dating back to the 1970s. Cracks in pipelines can be evaluated using pipeline-specific or generic methods [2-3]. The 'specific' methods are developed by the pipeline industry including the Log-Secant (or Ln-Sec) model [1], modified Log-Secant model [4], as well as the software-based methods such as pipe axial flaw failure criteria (PAFFC) [5], CorLAS^{TM} model [6-7], and a more recent PRCI MAT-8 model [8-9]. Such failure models characterize the toughness of pipeline steels in terms of the Charpy V-Notch (CVN) impact energy based on empirical correlations [10]. The 'generic' methods are codified but are not developed specifically for the pipeline industry, such as the well-known American Petroleum Institute's Recommended Practice 579 (API 579) [11], British Standard 7910 (BS 7910) [12], and R6 defect assessment procedures [13] by means of the failure assessment diagram (FAD).

The performance of a failure pressure model is usually evaluated by the mean and coefficient of variation (CoV) of the ratio of test failure pressure to the predicted failure pressure, which is the error in the prediction when compared to the experimental result, often termed as model error. The CoV represents the ratio of standard deviation to the mean. A high CoV indicates a large degree of dispersion between predicted and test data. Therefore, an ideal model should have a mean model error (also referred to as “bias”) closet to one and the lowest CoV. Over the past two decades, scholars have extensively investigated the performance of the above-mentioned failure pressure prediction models using various test data sources [14-18]. In 2009, Rothwell and Coote [14] compared the predictions made using BS 7910, Log-Secant, PAFFC, and CorLAS^{TM} models using 22 field and hydrostatic test failures, including 14 failures reported by Canadian Energy Pipeline Association (CEPA) and 8 hydrotest failures reported by Pembina Pipeline Corporation. In 2010, Hosseini et al. [15] compared the performance of API 579, BS 7910, Log-Secant, and CorLAS^{TM} models based on 4 full-scale burst tests. In 2014, Tandon et al. [16]

evaluated the performance of three crack assessment models (i.e., API 579, Log-Secant, and CorLAS^{TM}) using 15 full-scale burst test data. In the same year, Yan et al. [17] examined the accuracy of API 579, BS 7910, R6, Log-Secant, and CorLAS^{TM} models in predicting the failure pressure of cracked pipelines based on a collection of 104 full-scale burst tests from the open literature. In 2018, Yan et al. [18] continued to compare the performance of crack assessment models, including the API 579, modified Log-Secant, CorLAS^{TM}, and PRCI MAT-8 models using 63 hydrostatic test failures and also 12 in-service failures due to stress corrosion cracking (SCC).

Although all these studies consistently concluded that the CorLAS^{TM} model could provide reasonably accurate failure pressure predictions, the prediction data points were widely scattered around the 45-degree line (i.e., high CoV values). A follow-up investigation regarding the CorLAS^{TM} model was conducted by Zhang et al. [19], who performed a reliability-based assessment on the cracked pipes to examine the effect of the CorLAS^{TM} model error CoV on the probability of failure (PoFs) with respect to the safety factor. The results showed a significant increase in PoFs as the CoV increased, indicating the high sensitivity of the failure probability of a cracked pipe to the model error. On the other hand, numerical techniques such as the extended finite element method (XFEM), which is implemented in commercial finite element codes such as ABAQUS [20], are gaining increasing attention in solving fracture mechanics problems. Lately, many researchers [21-27] have applied XFEM to predict the failure pressure of pipelines with axial cracks or the tensile strain capacity of pipelines with circumferential cracks. Our previous work [22] compared the failure pressures predicted using XFEM and the CorLAS^{TM} model against a collection of more than 100 full-scale burst test data gleaned from the open literature. The findings indicated that XFEM can provide more accurate predictions than the CorLAS^{TM} model.

While XFEM is a powerful tool for simulating crack propagation, this approach can be computationally expensive. In contrast, machine learning (ML) methods such as artificial neural networks (ANN) offer a promising alternative for rapid prediction of the failure pressure of defective pipelines. In recent years, ANN has been applied successfully to predict the failure pressure of pipes with or without defects [28-29, 32]. Oh et al. [28] developed a four-layer deep neural network (DNN) model to predict the failure pressure of line pipes with a single dent and the model predicted results were compared with FEA and experimental results. A good agreement between the results was observed, demonstrating the accuracy of the predictions using DNN. The applicability of ANN in predicting the failure pressure of pipe with corrosion was studied by Xu

et al. [29], and they concluded that the ANN-predicted results were more accurate than the results predicted using two popular corrosion assessment methods: ASME B31G [30] and DNV-RP-F101 [31]. The failure pressure of intact (defect-free) pipes using ANN was investigated by Zolfaghari and Izadi [32]. Despite the considerable effort dedicated to evaluating the failure pressure of pipelines with defects such as corrosion or dents using ANN, no published studies have focused on the failure pressure prediction of pipelines with cracks using ANN. To the best of the authors' knowledge, this work is the first rigorous attempt to develop a failure pressure prediction model for cracked pipes using ANN.

The reminder of this chapter is arranged as follows. The basic concept of XFEM is described in **Section 6.2** and a parametric study is performed in **Section 6.3**. **Section 6.4** presents the development of the ANN model including the model training and validation, followed by conclusions at the end of the chapter.

6.2. XFEM

XFEM, based on a local partition of unity method (PUM) [33], was proposed by Belytschko and Black [34] in 1999 and became a popular numerical tool in simulating strong discontinuities such as cracks. As shown in **Figure 6-1**, additional enrichment functions are added to the standard finite element approximation to ensure the presence of cracks. The Heaviside enrichment (or jump) function is used to enrich nodes whose shape functions are cut by the interior of the crack, while the asymptotic crack-tip function captures the singularity near the crack tip [35]. A notable advantage is that the mesh is no longer required to conform to the crack geometry, as compared to the conventional finite element method (FEM).

Two approaches within the XFEM framework are available in ABAQUS for modelling crack growth: the linear elastic fracture mechanics (LEFM)-based approach and the cohesive segment approach [35]. The LEFM-based approach is only recommended to model brittle fracture. In this work, the cohesive segment approach is adopted since it is suitable for modelling brittle or ductile fractures [35]. This approach is based on the traction-separation cohesive behavior and consists of a damage initiation criterion and damage evolution law. Three stress-based and three strain-based built-in damage initiation criteria are readily available in ABAQUS [35]. Aside from the options for choosing a built-in initiation criterion, ABAQUS offers a user-defined damage

initiation criterion that can be specified in the user subroutine UGMGINI, as discussed in Lin et al. [36]. The evolution of damage can be defined using either of these two parameters: the dissipated energy due to failure, known as fracture energy (G_c), or the plastic displacement at failure [35].

In the current study, damage initiates when the maximum principal strain (MAXPE) reaches the specified value, and damage evolution is described using an energy-based approach.

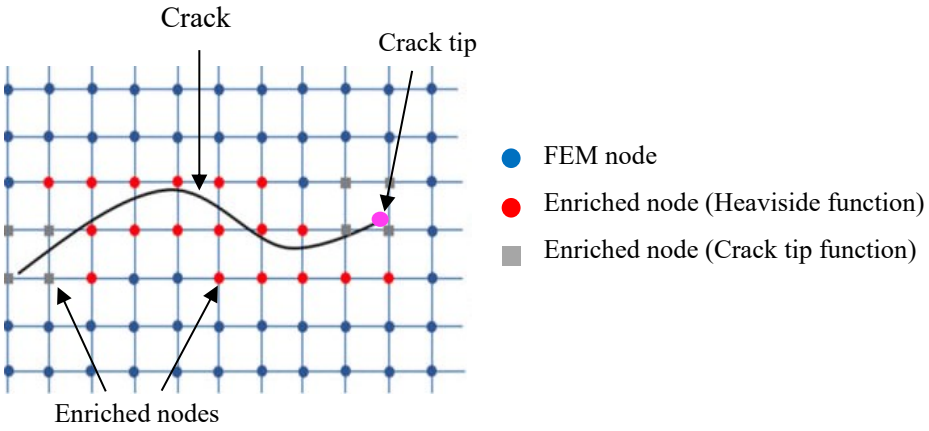

Figure 6-1: Schematic of the enriched nodes in XFEM, adapted from [37]

6.3. Simulated Data Generation via Parametric Analysis

6.3.1 Analysis Cases

To establish a large database for developing the ANN model, extensive parametric XFEM analyses are conducted, considering four different pipe grades, including low-strength (X52), mid-strength (X60 and X65), and high strength (X80). **Table 6-1** presents the pipe geometric information and material properties for the parametric study, adopted from references [1, 38]. The selected pipes are assumed to be made from line-pipe (API) steels which is the common practice in the industry. It should be noted that the reported Charpy V-notch (CVN) energies from the full-scale tests are used to select the XFEM damage properties (MAXPE and G_c) based on the correlation developed in **Section 5.3.2**. Specifically, for a given CVN energy, recommendations for the selection of the MAXPE and G_c are:

$$MAXPE = \begin{cases} 0.01, CVN < 70\ \text{J} \\ 0.015, CVN \geq 70\ \text{J} \end{cases} \qquad G_c(\text{N/mm}) = \begin{cases} 10, & CVN < 20\ \text{J} \\ 20, & 20\ \text{J} \leq CVN < 35\ \text{J} \\ 50, & 35\ \text{J} \leq CVN < 70\ \text{J} \\ 100, & CVN \geq 70\ \text{J} \end{cases}$$

For each pipe case, pipe size (or the diameter-to-thickness ratio), normalized crack depth and crack length are varied, while pipe material properties (σ_{YS} and σ_{UTS}) and two damage properties (MAXPE and G_c) remain unchanged. **Figure 6-2** presents a schematic view of an axial rectangular crack in a pipe with a given depth (a) and length (L).

Table 6-2 presents the values of geometric variables considered in Case 1, where a wide range of three variables is included to perform a comprehensive parametric study. For the remaining cases, the values of the variables are selected based on the parametric results from Case 1 to optimize computational efficiency, as tabulated in **Table 6-3**. Crack depth is normalized by the pipe wall thickness (t) with values in the 0.4, 0.5, 0.6, 0.7, or 0.8. The reason that the crack depth-to-thickness ratio in the analysis cases is set up to 0.8 is because cracks with a/t ratio over 0.8 are unacceptable, according to the Canadian Standards Association (CSA) [39]. It is noteworthy that $L^2/(Dt)$ is employed as a dimensionless parameter to distinguish between long and short defects in computing the Folias factor in the CorLAS^{TM} model. Hence, crack length is normalized here using pipe outer diameter (D) and pipe wall thickness (t). Considering the normalized crack length in the majority of collected test data [22] falls within the range (1, 18), the normalized crack length is therefore taken as 1, 2, 4, 6, 8, 10, 12, 14 or 18. Thin-walled pipes (i.e., $D/t \geq 20$) are the focus of this study, hence, the diameter-to-thickness ratio (D/t) is taken as 40, 50, 60, 70, 80, or 90. This is done to cover a wide range of practical geometry. These FEA simulations comprise a sufficient database for the pipe and crack geometries of interest and serve as a solid basis for the following ANN model development.

Table 6-1: Geometric information and material properties for the parametric study

Source	Pipe case	Steel grade	D (mm)	σ_{YS} (MPa)	σ_{UTS} (MPa)	CVN (J)	XFEM damage parameters	
							MAXPE	Gc
	1	X52	762	417	560	36.6	0.01	50
[1]	2	X60	762	423	587	27.1	0.01	20
	3	X65	914.4	474	604	18.9	0.01	10
[38]	4	X80	762	673	723	175	0.015	100

Table 6-2: Geometric variables considered for Case 1

Variables	Values
Diameter-to-thickness ratio, D/t	40, 50, 60, 70, 80, and 90
Normalized crack depth, a/t	0.4, 0.5, 0.6, 0.7, and 0.8
Normalized crack length, $L^2/(Dt)$	1, 2, 4, 6, 8, 10, 12, 14, 16, and 18

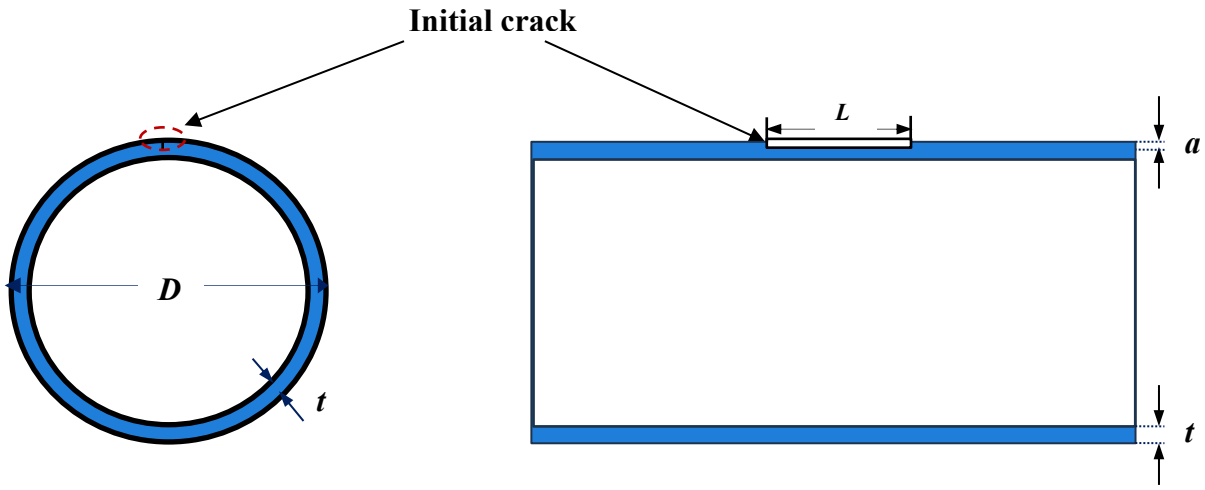

(a) Cross-section (b) Longitudinal section

Figure 6-2: Schematic view of an axial rectangular crack on pipe surface.

6.3.2 XFEM Model Development

Given that the performance of an ANN model is highly rely on the accuracy of the input (XFEM) data, it is of great importance to examine the accuracy of XFEM before using the generated datasets to train the ANN model. A preliminary work was performed in **Section 5.3** to validate the XFEM model based on a collection of more than 100 full-scale burst tests data of pipelines with axial surface cracks. Excellent agreement was observed between the XFEM predictions and test results with a mean test-to-prediction ratio of 1.001 and CoV of 8.8%, providing strong validation for the XFEM simulation datasets employed in the following analysis.

In this study, XFEM models are developed in the framework of ABAQUS/CAE [20]. Only half of the pipe with a length (L_{model}) of three times the pipe diameter is modelled by taking advantage of symmetry, as shown in **Figure 6-3**. The internal pressure load is applied to the inner

surface of the pipe with increasing magnitude. As discussed in [22], cracks in reality typically have irregular shapes, whereas idealized planar cracks are considered in numerical analyses with the assumption of regular shapes such as rectangles and semi-ellipsoids. The crack is positioned at the outer surface in axial orientation. Fine mesh is assigned at the proximity of the crack region while the mesh away from the defect area is coarser with an appropriate gradient in the transition area. The mesh size is selected after a sensitivity study [21]. A reference point (RP) is created at the center of the intact end of the pipe and the end surface is then coupled to this RP. Failure is determined when the crack penetrates the entire pipe wall, as illustrated in **Figure 6-4**.

True stress-strain data is required as part of the material property when modelling elastic-plastic materials using ABAQUS/CAE [20]. The stress-strain relationship can be characterized using several empirical equations defined by two fitting parameters, which should be determined by non-linear curve fitting to the tensile tests, detailed discussion can be found in [40]. However, if only the σ_{YS} and σ_{UTS} are reported from the literature, in the absence of true stress-strain data, the modified Ramberg-Osgood equation (ROE) below is recommended in API579-1/ASME FFS-1 [11] to compute the fitting coefficients.

$$\varepsilon = \frac{\sigma}{E} + \left(\frac{\sigma}{H_{RO}}\right)^{\frac{1}{n_{RO}}} \tag{6-1}$$

In the above equation, ε and σ are the true strain and true stress, E is the Young's modulus, H_{RO} and n_{RO} are the fitting coefficients in ROE. Given only the values of σ_{YS} and σ_{UTS}, n_{RO} can be calculated as follows:

$$n_{\mathrm{RO}} = \frac{1+1.3495\left(\frac{\sigma_{YS}}{\sigma_{UTS}}\right)-5.3117\left(\frac{\sigma_{YS}}{\sigma_{UTS}}\right)^2+2.9643\left(\frac{\sigma_{YS}}{\sigma_{UTS}}\right)^3}{1.1249+11.0097\left(\frac{\sigma_{YS}}{\sigma_{UTS}}\right)-11.7464\left(\frac{\sigma_{YS}}{\sigma_{UTS}}\right)^2} \tag{6-2}$$

H_{RO} can be estimated based on n_{RO} and σ_{UTS} using the following expression:

$$H_{\mathrm{RO}} = \frac{\sigma_{UTS}\exp(n_{RO})}{{n_{RO}}^{n_{RO}}} \tag{6-3}$$

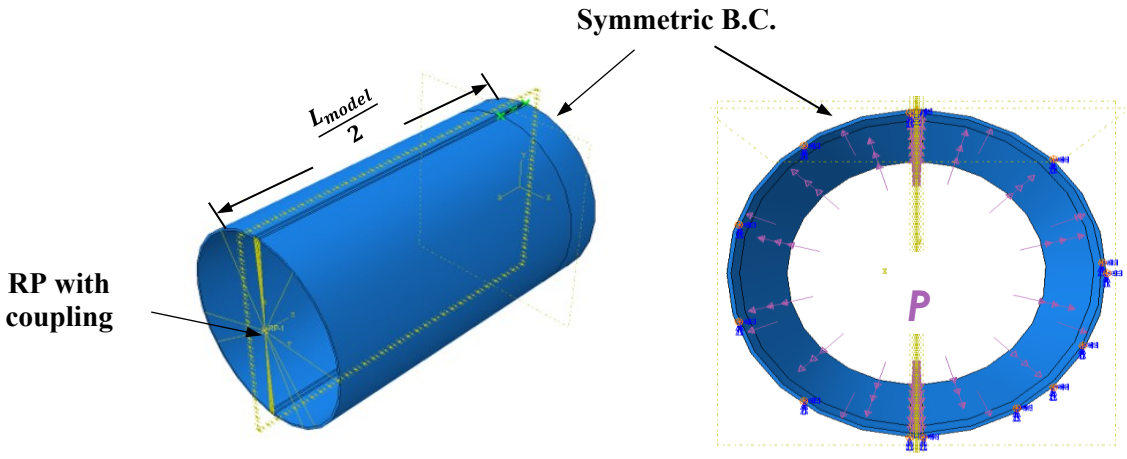

Figure 6-3: Half pipe model with boundary conditions and loading

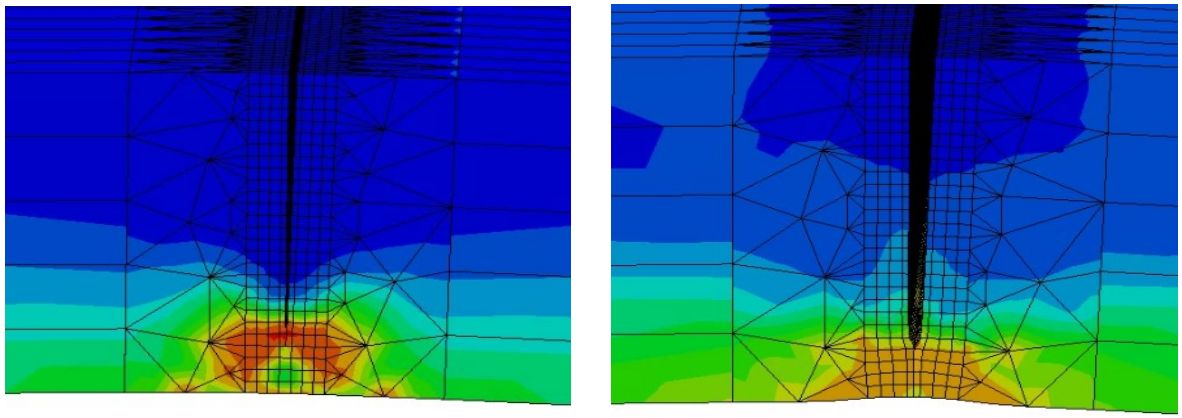

(a) Long and deep crack ($L^2/(Dt)$ = 18, a/t = 0.8)

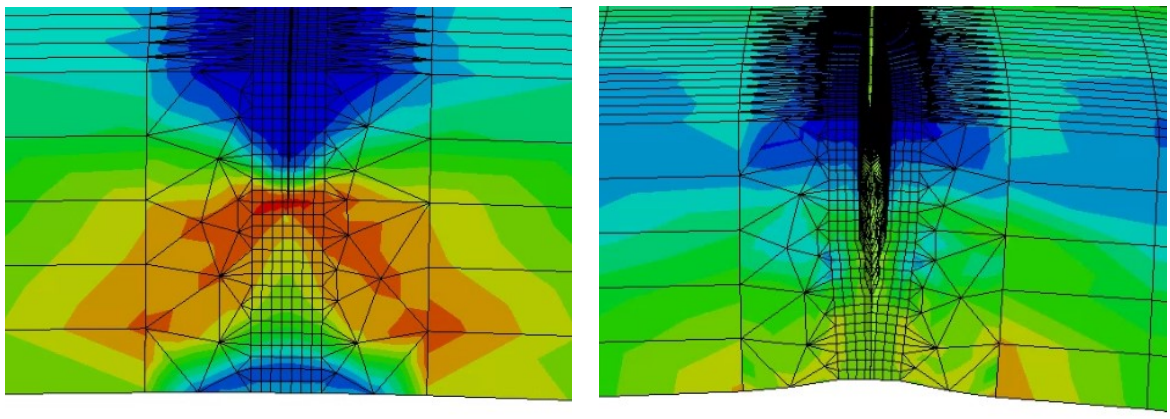

(b) Short and shallow crack ($L^2/(Dt)$ = 1, a/t = 0.4)

Figure 6-4: Stress distributions of the enriched region from crack initiation to complete failure: (a) long and deep crack; and (b) short and shallow crack

6.3.3 Analysis Results

For the sake of brevity, only part of the results for pipe case 1 are discussed here. As mentioned earlier, a wide range of three geometric variables (D/t, a/t, and $L^2/(Dt)$) are considered for Case 1 to investigate the effects of these variables on the failure pressure. Specifically, all the models in Case 1 are created with an outer diameter of 762 mm and varying t that provides D/t ratios equal to 40, 50, 60, 70, 80, and 90.

To examine the impact of pipe size (or D/t ratio) on the predicted failure pressure of pipes with axial cracks, numerous XFEM models are developed with various D/t ratios varying from 40 to 90 with different crack dimensions. **Figure 6-5** illustrates the variation of XFEM-predicted failure pressures with D/t ratios for different cracks. As the D/t ratio increases, the failure pressure drops rapidly. The results indicate thinner pipes (high D/t ratios) have a lower failure pressure.

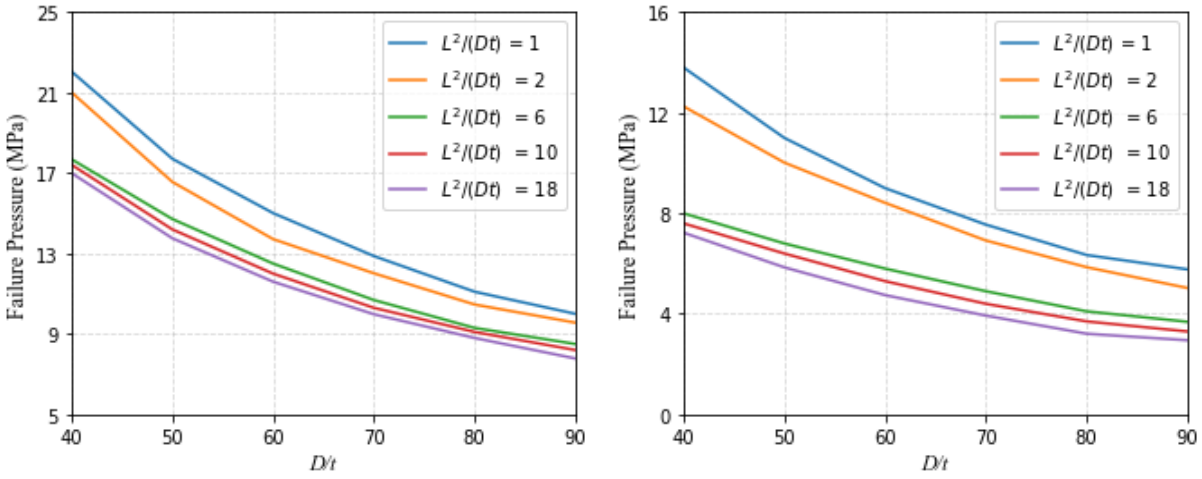

(a) $a/t = 0.4$ (b) $a/t = 0.8$

Figure 6-5: The variation of the failure pressure on the diameter-to-thickness ratio for different crack lengths (a) shallow crack: $a/t = 0.4$; (b) deep crack: $a/t = 0.8$ (Pipe case 1)

The impact of the normalized crack depth on the predicted failure pressure of pipe with the same crack length ($L^2/(Dt) = 1$ and 18) and various D/t ratios, is illustrated in **Figure 6-6**. As expected, the failure pressure decreases with the increase of crack depth. More than 50% reduction in the predicted failure pressure is observed for long cracks, while around a 30% reduction is

noticed for short cracks. This implies that the normalized crack depth has a more dominant influence on the failure pressure for long cracks ($L^2/(Dt) = 18$).

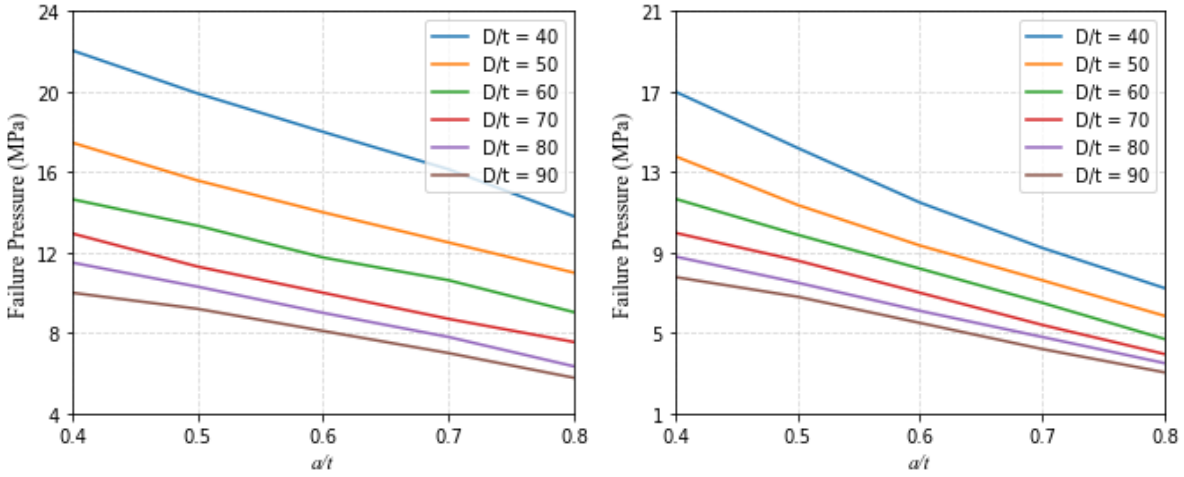

(a) $L^2/(Dt) = 1$ (b) $L^2/(Dt) = 18$

Figure 6-6: The variation of the failure pressure on the normalized crack depth for different diameter-to-thickness ratios (a) short crack: $L^2/(Dt) = 1$; (b) long crack: $L^2/(Dt) = 18$ (Pipe case 1)

Similar to the investigations of the effects of crack depth and pipe size, the effect of normalized crack length, $L^2/(Dt)$, with different D/t ratios (40, 50, 60, 70, 80, and 90) and normalized crack depths ($a/t = 0.4$ and 0.8) on the predicted failure pressure of cracked pipes is demonstrated in the figures below. As depicted in **Figure 6-7**, the failure pressure in general decreases nonlinearly as crack length increases. It is unsurprisingly that the longer the defect, the lower the failure pressure. Significant reductions are observed in the predicted failure pressure as the normalized crack length increases from 1 to 10, beyond which the failure pressure drops gradually.

It is worth mentioning that for varying pipe sizes, there is an approximately 50% reduction in the predicted failure pressure for the deep crack ($a/t = 0.8$). In the case of the shallow crack ($a/t = 0.4$), failure pressure decreases by around 30% when the normalized crack length increases from 1 to 18. This indicates that the influence of the normalized crack length on the failure pressure is more pronounced for the deep crack compared to the shallow crack. Additionally, it is observed

that the effect of crack length on the failure pressure of thicker pipes (D/t = 40 and 50) is insignificant for a normalized crack length beyond 10. Similarly, for thinner pipes (D/t = 60, 70, 80, and 90), the effect is insignificant when the normalized crack length exceeds 6.

Based on the parametric results from Case 1, six D/t ratios are considered for the remaining pipe cases with the optimized selection of crack depths and crack lengths, as tabulated in **Table 6-3**.

Table 6-3: Geometric variables considered for the remaining cases

Variables	Values
Diameter-to-thickness ratio, D/t	40, 50, 60, 70, 80, and 90
Normalized crack depth, a/t	0.4, 0.6, and 0.8
Normalized crack length, $L^2/(Dt)$	1, 2, 6, 10, and 18

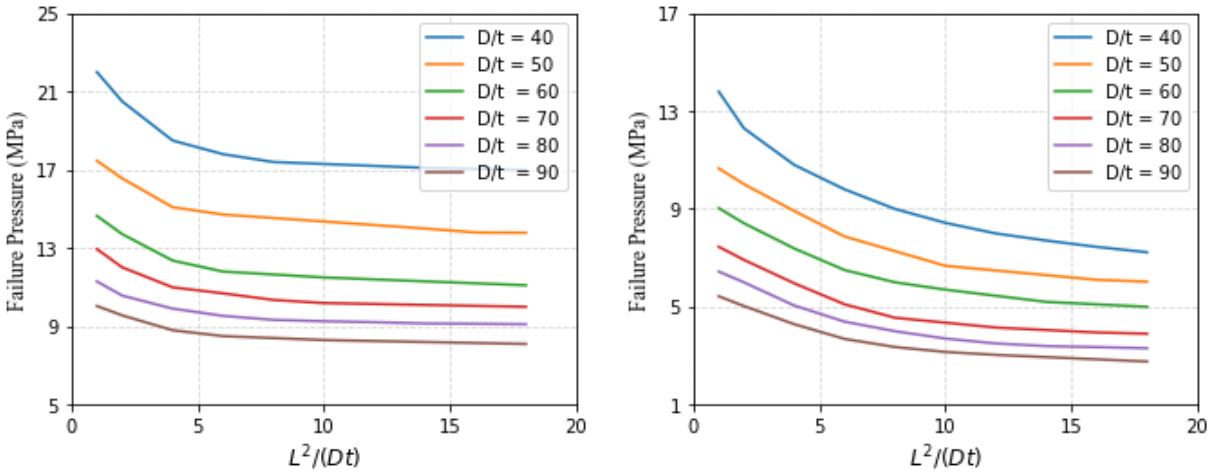

(a) a/t = 0.4 (b) a/t = 0.8

Figure 6-7: The variation of the failure pressure on the normalized crack length for different diameter-to-thickness ratios (a) shallow crack: a/t = 0.4; (b) deep crack: a/t = 0.8 (Pipe case 1)

6.4. Development of an ANN Model

6.4.1 Model Structure

Based on a total of 498 data obtained from the parametric study described in **Section 6.3**, an ANN model is constructed and trained using the open-source libraries Scikit-learn and TensorFlow implemented in PYTHON. The concept of ANN is inspired by neural networks in the human brain [41]. The ANN comprises of an input layer, one or more hidden layers, and an output layer. The neurons in the input (first) layer are the input variables and the neurons in the output (last) layer are the output variables. The hidden layer lies between the input and output layer, but the number of hidden neurons is unknown and normally determined using the trial-and-error approach. The input and output variables of the ANN model are summarized in **Table 6-4**. Considering the relatively small number of samples and most functions can be effectively approximated using a single hidden layer [42], the exploration for deeper ANN's deemed unnecessary; hence, the proposed ANN model in this work has three layers with a single hidden layer, as shown in **Figure 6-8**.

Table 6-4: Input and output parameters of the ANN model

Parameters	**Description**
Input	D/t: Diameter-to-wall thickness ratio
	a/t: Crack depth-to-wall thickness ratio
	$L^2/(Dt)$: Normalized crack length
	MAXPE: Maximum principal strain (XFEM damage parameter)
	G_c: Fracture energy (XFEM damage parameter)
Output	P_f: Failure pressure (MPa)

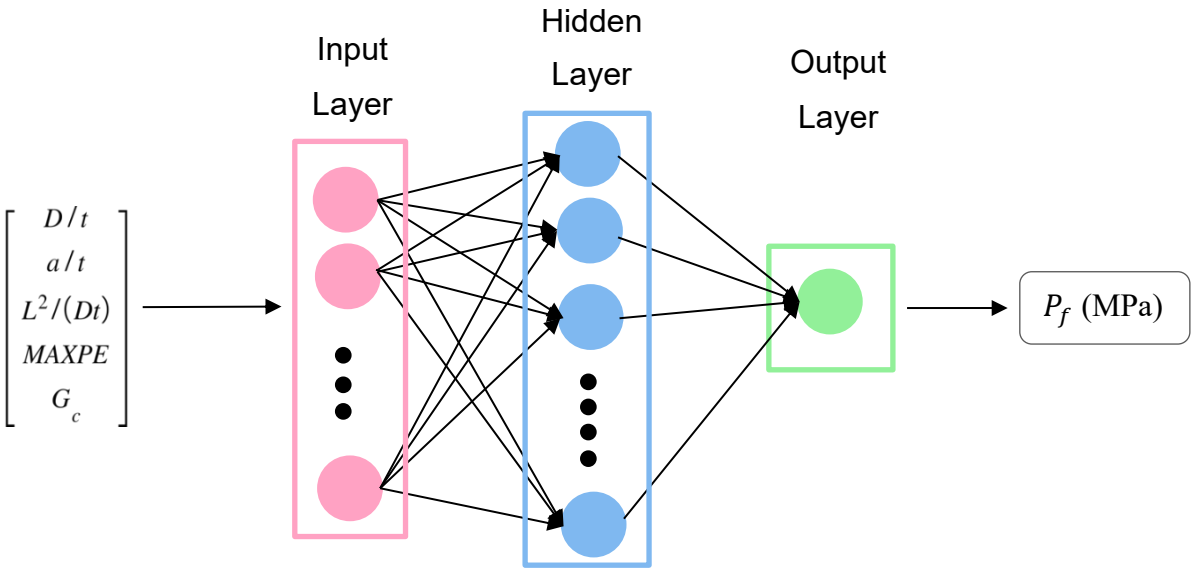

Figure 6-8: A three-layer ANN architecture

The rectified linear unit (ReLU) function is selected as the activation function for the hidden units and the linear function is used for the output unit. Due to the large magnitude differences for different input features, it is necessary to transform all the input features into the same scale before the training process. In this study, the data are normalized using MinMaxScaler, which would transform the minimum value into 0, the maximum value into 1, and other values to a range of 0 to 1, for a given data x, the normalization is calculated using the following formula:

$$x_{normalized} = \frac{x_o - x_{min}}{x_{max} - x_{min}} \tag{6-4}$$

Here, $x_{normalized}$ is the normalized value, x_o is the original value (before normalization), x_{max} and x_{min} are the maximum and minimum values of the data, respectively.

6.4.2 Training and Testing ANN Model

The datasets from XFEM simulations were used for training and validation. The Adam optimization algorithm [43] is selected for optimizing the ANN model. The performance of an ANN model can be evaluated using various metrics such as mean absolute error (MAE), mean absolute percentage error (MAPE), mean relative error (MRE), mean squared error (MSE), and

coefficient of determination (R^2). For this study, MSE and R^2 are adopted to analyze results for all data, expressed as follows:

$$MSE = \frac{1}{N}\sum_{i=1}^{N}(y_i - \hat{y}_i)^2 \tag{6-5}$$

$$R^2 = 1 - \frac{\sum_{i=1}^{N}(y_i - \hat{y}_i)^2}{\sum_{i=1}^{N}(y_i - \overline{y_a})^2} \tag{6-6}$$

In the above equations, N represents the total number of data, y_i is the actual (or target) value, $\hat{y}_i$ is the predicted (or output) value and y_a is the average of the actual values.

Generally, K-fold cross-validation is a more preferred approach over the hold-out test to prevent over-fitting. This method randomly splits the dataset into K subsets, allowing the model to be trained and evaluated K times. For each iteration, (K-1) subsets are selected as the training part, and the remaining 1 subset is assigned as the testing dataset.

In this study, 5-fold cross-validation is employed to identify the optimal ANN architecture, a typical flowchart of 5-fold cross-validation is shown in **Figure 6-9**. The number of neurons in the hidden layer varies between 8 and 48 and the optimal number of hidden units that gives the minimum MSE and the maximum R^2 is found to be 36. Early stopping is implemented to prevent overfitting the training data as training is stopped once the validation loss is not decreased. The performance of the optimal model during the training and testing process is shown in **Figure 6-10**. It can be observed that failure pressure predicted using the ANN model corresponded well with the XFEM-predicted data during both training and testing stages.

Furthermore, the performance of the well-known crack assessment model, the CorLAS^{TM} model, is evaluated using the XFEM datasets from the parametric study. As stated previously, the CorLAS^{TM} model is widely used and accepted by the pipeline industry to assess the failure pressure of pipelines with axial cracks, based on the elastic-plastic (or inelastic) fracture mechanics. In the CorLAS^{TM} model, the failure is evaluated based on two independent criteria, namely, flow strength and fracture toughness criteria. The failure pressure (P_f) is computed by Eq. (6-7):

$$P_f = min\{\sigma_f, \sigma_t\}\frac{2t}{D}\left(\frac{1-\frac{A_{eff}}{A_0}}{1-\frac{A}{MA_0}}\right) \tag{6-7}$$

$$M = \begin{cases} \sqrt{1 + 0.6275\frac{L^2}{Dt} - 0.00375\left(\frac{L^2}{Dt}\right)^2}, \frac{L^2}{Dt} \leq 50 \\ 3.3 + 0.032\frac{L^2}{Dt}, \frac{L^2}{Dt} > 50 \end{cases} \quad (6\text{-}8)$$

$$A_{eff} = \begin{cases} La, & Rectangular\ crack \\ \frac{\pi}{4}La, & semi - elliptical\ crack \end{cases} \quad (6\text{-}9)$$

Where P_f denotes the failure pressure, M is the Folias factor and can be calculated using Eq. (6-8), A_o is the reference area ($A_o = Lt$) and A_{eff} is the effective area (Eq. (6-9)). σ_f is referred to as the flow stress, typically defined as the average of the yield strength and ultimate tensile strength ($\sigma_f = \frac{\sigma_{YS}+\sigma_{UTS}}{2}$). σ_t is the local failure stress in the fracture toughness criterion. The value of σ_t is obtained by iteratively computing J-integral (Eq. (6-10)) until its value equals to the fracture toughness of the material (J_C) which is either determined from the laboratory testing or CVN energy, as discussed in [39].

$$J = Q_f F_{sf}[\frac{\sigma^2 \pi a}{E} + f_3(n) a \varepsilon_p\ \sigma_t] \quad (6\text{-}10)$$

Where Q_f and F_{sf} are geometrical factors and $f_3(n)$ is a dimensionless factor developed by Shih and Hutchinson [45]. Detailed computation of J-integral can be found in [20].

Figure 6-11 illustrates the comparisons of failure pressures predicted using the CorLAS^{TM} model against the XFEM simulation results. It can be observed that the CorLAS^{TM} model tends to provide conservative predictions as the majority of the data points fall below the solid line (i.e., 1:1 line).

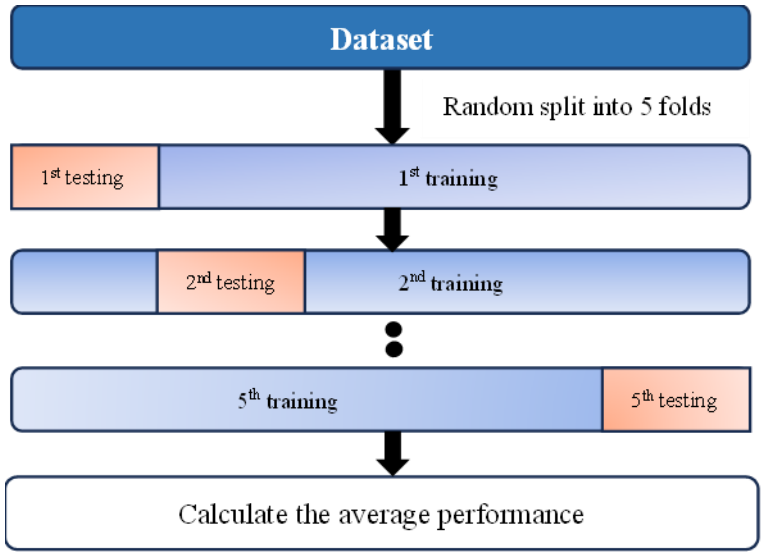

Figure 6-9: Flowchart for 5-fold cross-validation

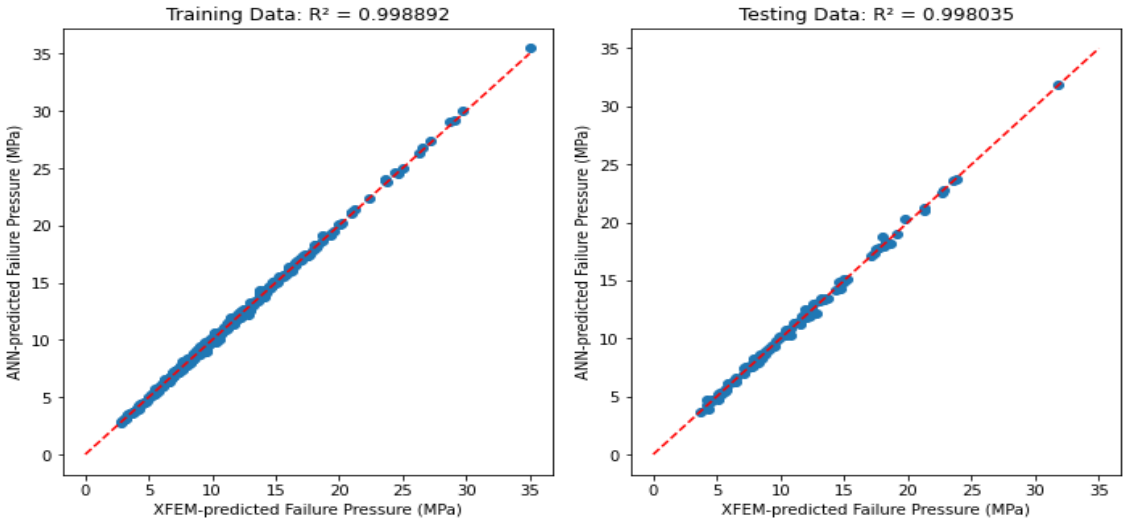

(a) (b)

Figure 6-10: ANN model predictions vs. true values for: (a) training datasets; (b) testing datasets

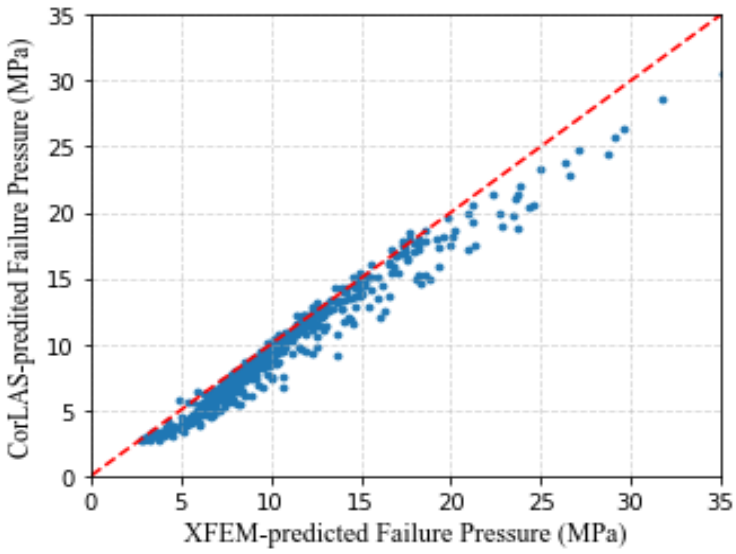

Figure 6-11: CorLAS^{TM} model predictions vs. true values for ANN datasets (XFEM data)

6.4.3 Validation with Experimental Results

The trained ANN model is further validated using full-scale burst tests collected from the open literature [1, 15, 38, 44-47]. Note that some tests with geometrical parameters outside the training scope are excluded. For example, in Hosseini et al. [15], 4 burst tests were conducted on a 508 mm diameter API X60 grade line pipe with a 5.7 mm wall thickness. The tensile properties were obtained from tensile coupon tests with the average values of yield strength and tensile strength equal to 433 MPa and 618 MPa, respectively. Sharp elliptical cracks were created in the pipe wall using a Jeweller's saw. Specimen CR1 is excluded here because its crack depth-to-thickness ratio is 0.38, which is out of the training range. Similarly, test specimens in Amano and Makino [44] were made of API X100 grade steel and had a 914.4 mm outer diameter with 19.1 mm wall thickness. The average yield strength and tensile strength were 776 MPa and 843 MPa, respectively. The artificial notch was induced using electric discharge machining (EDM). A total of 9 burst tests were reported in [44], but two tests (W1 and W9) are excluded here because the W1 pipe is defect-free and the crack depth-to-thickness ratio of the W9 pipe is 0.88, which is outside the range of parameters the ANN model is trained on. Overall, a total of 25 burst tests are selected with D/t in the range of 43.54 to 89.12, a/t between 0.41 and 0.8, and $L^2/(Dt)$ varied from 1.18 to 17.88. Details of the 25 burst test data are tabulated in **Appendix E**.

Figure 6-12 illustrates the comparisons of failure pressures predicted using the ANN model and CorLAS^{TM} model against the test results. It can be observed that the ANN-predicted data spread along the solid line (i.e., 1:1 line) and failure pressures predicted by the ANN model showed better correlation when compared to the ones computed by the CorLAS^{TM} model. The mean value and CoV of ANN-prediction error are 1.01 and 4.76%, respectively, while the mean and CoV of CorLAS^{TM} model error are 1.07 and 12.8%, respectively. The results indicate the higher accuracy of the developed ANN model.

The developed ANN model (see Ref. [48]) in this work is publicly available on the online platform, MecSimCalc [49]; a website that enables users to create and share python-based apps.

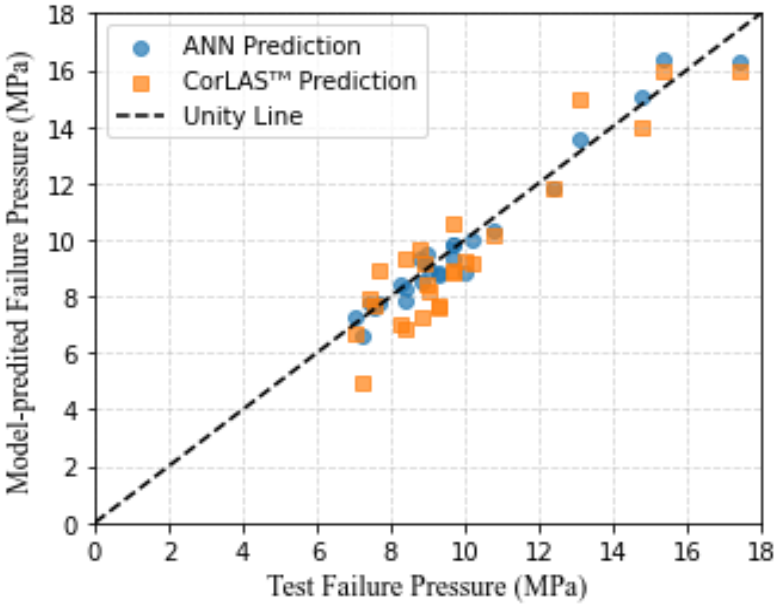

Figure 6-12: Comparison between the model-predicted failure pressures and experimental results

6.5. Conclusions

In this article, a parametric study is first performed to investigate the effects of several geometrical factors on the failure pressure of pipelines with axial cracks. The parametric analyses reveal that the failure pressure is strongly dependent on the crack size (crack depth and crack length) and pipe size, the failure pressure significantly decreases with the increase of the crack and

pipe sizes. The analysis results obtained from the XFEM-based parametric study are then used to develop an ANN model for predicting the failure pressure of cracked pipelines. The database covers a wide range of low-strength to high-strength pipeline steels with diameter-to-thickness ratio from 40 to 90, crack depth-to-thickness ratio from 0.4 to 0.8, normalized crack length from 1 to 18. The ANN is performed using the programming language PYTHON and the performance of the ANN model is evaluated using two metrics (MSE and R^2). The fact that R^2 values for both the training and validation cases are above 0.99, indicates the high accuracy of the ANN model.

The trained ANN model is validated by comparison with the parametric results. According to the validation results, the ANN-predicted failure pressures correspond well with the results generated from the XFEM parametric study. Furthermore, the failure pressures computed by ANN and the CorLAS^{TM} model are compared against 25 full-scale burst test data collected from the literature. The results indicate a good accuracy of the developed ANN model with a mean and CoV of the model error equal to 1.01 and 4.76%. Notably, the ANN model produces a smaller prediction error than the CorLAS^{TM} model.

Within the range of trained variables, the developed ANN model can be a reliable and alternative tool for predicting the failure pressure of pipelines with an axial crack, more accurate predictions in terms of mean (or bias) and more precise predictions in terms of CoV (or scatter), compared to the CorLAS^{TM} model.

References

[1] Kiefner, J.F., Maxey, W.A., Eiber, R.J. and Duffy, A.R. Failure stress levels of flaws in pressurized cylinders. Progress in flaw growth and fracture toughness testing, STP 536, *ASTM International*, West Conshohocken, PA, pp. 461-481, 1973.

[2] Cosham, A., Hopkins, P. and Leis, B. Crack-like defects in pipelines: the relevance of pipeline-specific methods and standards, *Proceedings of International Pipeline Conference*, IPC2012-90459. Calgary, Canada, 2012.

[3] Zhang, X., Zheng, Q., Leung, J.Y. and Adeeb, S. Reliability-based Assessment of Cracked Pipelines using Monte Carlo Simulation Technique with CorLAS^{TM}. Paper No. PVP2022-80412, *Proceedings of the Pressure Vessel and Piping Conference*, American Society of Mechanical Engineers, Las Vegas, USA, 2022.

[4] Kiefner, J.F. Modified equation aids integrity management. *Oil & Gas Journal*. 106 (37), 78–82, 2008a.

[5] Kiefner, J.F. Modified ln-secant equation improves failure prediction. *Oil & Gas Journal*. 106 (38), 64–66, 2008b.

[6] Leis, B. N., and Ghadiali, N. D., Pipe Axial Flaw Failure Criteria – PAFFC. Version 1.0 User's Manual and Software, Topical Report to the Line Pipe Research Supervisory Committee of the Pipeline Research Committee of the American Gas Association, NG-18, Catalog No. L51720, May 1994.

[7] Jaske, C. E. and Beavers, J. A. Integrity and Remaining Life of Pipe with Stress Corrosion Cracking. PRCI 186-9709, Catalog No. L51928. Pipeline Research Council International, Falls church, 2001.

[8] Jaske, C.E., Beavers, J.A. and Harle, B.A. Effect of Stress Corrosion Cracking on Integrity and Remaining Life of Natural Gas Pipelines, Paper No. 255, Corrosion 96, NACE International, Houston, 1996.

[9] Anderson, T. Development of a Modern Assessment Method for Longitudinal Seam Weld Cracks. PRCI Catalogue No. PR-460-134506-R0. Pipeline Research Council International, Chantilly, 2015.

[10] Anderson, T. Assessing Crack-like Flaws in Longitudinal Seam Welds: a State-Of-The-Art Review. PRCI Catalogue No. PR-460-134506-R02. Pipeline Research Council International, Chantilly, 2017.

[11] API 579-1/ASME FFS-1, Fitness-for-service, American Society of Mechanical Engineers, USA, 2019.

[12] British Standards Institution. BS 7910. Guide to Methods for Assessing the Acceptability of Flaws in Metallic Structures. London, UK, 2019.

[13] EDF Energy. R6: Assessment of the Integrity of the Structures Containing Defect. Gloucester, UK amendment 10 R6, revision 5, 2013.

[14] Rothwell, A.B. and Coote, R.I. A critical review of assessment methods for axial planar surface flaws in pipe. *In: International Conference on Pipeline Technology*, Ostend, Belgium, 2009.

[15] Hosseini, A., Cronin, D., Plumtree, A. and Kania, R. Experimental Testing and Evaluation of Crack Defects in Line Pipe. *Proceedings of the 8th International Pipeline Conference*, IPC2010-31158, Calgary, Canada, 2010.

[16] Tandon, S., Gao, M., Krishnamurthy, R., Kariyawasam, S. and Kania, R. Evaluation of Existing Fracture Mechanics Models for Burst Pressure Predictions, Theoretical and Experimental Aspects, Paper No. IPC2014-33563, *Proceedings of the ASME 2014 10th International Pipeline Conference*, Calgary, Canada, 2014.

[17] Yan, Z., Zhang, S. and Zhou, W. Model error assessment of burst capacity models for energy pipelines containing surface cracks, *International Journal of Pressure Vessels and Piping*, 120-121: pp. 80-92, 2014.

[18] Yan, J., Zhang, S., Kariyawasam, S., Pino, M. and Liu, T. Validate crack assessment models with in-service and hydrotest failures. Paper No. IPC2018-78251, *Proceedings of the 2018 12th International Pipeline Conference*, *American Society of Mechanical Engineers*, Calgary, Canada, 2018.

[19] Zhang, X., Zheng, Q., Leung, J.Y. and Adeeb, S. Reliability-based assessment of cracked pipelines using monte carlo simulation technique with CorLAS™. Paper No. PVP2022-80412, *Proceedings of the Pressure Vessel and Piping Conference, American Society of Mechanical Engineers*, Las Vegas, USA, 2022.

[20] Dassault Systèmes, 2022. Abaqus documentation.

[21] Zhang, X., Lin, M., Okodi, A., Tan, L., Leung, J.Y. and Adeeb, S. Numerical analysis of API X42 and X52 vintage pipes with cracks in corrosion defects using extended finite element method. Paper No. PVT-20-1218, *Journal of Pressure Vessel Technology*, 143(6):061302, 2021.

[22] Zhang, X., Yoosef-Ghodsi, N., Kainat, M., Leung, J.Y. and Adeeb, S. Comparative study of crack shape on the ductile fracture response of cracked pipelines. Paper No. PVP2024-121892, Forthcoming, *Proceedings of the Pressure Vessel and Piping Conference, American Society of Mechanical Engineers*, Washington, USA, 2024.

[23] Zhang, X., Okodi, A., Tan, L., Leung, J.Y. and Adeeb, S. Failure pressure prediction of crack in corrosion defects using XFEM. Paper No. IPC2020-9312, *Proceedings of the 2020 13th International Pipeline Conference, American Society of Mechanical Engineers*, Virtual, Online, 2020.

[24] Zhang, X., Okodi, A., Tan, L., Leung, J.Y. and Adeeb, S. Failure pressure prediction of crack in corrosion defects in 2D by using XFEM. Paper No. PVP2020-21046, *Proceedings of the Pressure Vessel and Piping Conference, American Society of Mechanical Engineers*, Virtual, Online, 2020.

[25] Okodi, A., Lin, M., Yoosef-Ghodsi, N., Kainat, M., Hassanien, S. and Adeeb, S. Crack propagation and burst pressure of longitudinally cracked pipelines using extended finite element method. *International Journal of Pressure Vessels and Piping*, 184(5): 104115, 2020.

[26] Lin, M., Agbo, S., Cheng, J.J.R., Yoosef-Ghodsi, N. and Adeeb, S. Application of the extended finite element (XFEM) to simulate crack propagation in pressurized steel pipes. Paper No. PVP2017-65575, *Proceedings of the Pressure Vessel and Piping Conference, American Society of Mechanical Engineers*, Hawaii, USA, 2017.

[27] Agbo, S., Lin, M., Amerli, I., Imanpour, A., Duan, D-M., Cheng, J.J.R. and Adeeb, S. Evaluation of the effect of internal pressure and flaw size on the tensile strain capacity of X42 vintage pipeline using damage plasticity model in extended finite element method (XFEM). Paper No. PVP2019-94005, *Proceedings of the Pressure Vessel and Piping Conference, American Society of Mechanical Engineers*, San Antonio, Texas, USA, 2019.

[28] Oh, D., Race,J., Oterkus, S. and Koo, B. Burst pressure prediction of API 5L X-grade dented pipelines using deep neural network. *Journal of Marine Science and Engineering*, vol. 8, no. 766, 2020.

[29] Xu, W., Li, C.B., Choung, J. and Lee, J. Corroded pipeline failure analysis using artificial neural network scheme. *Advances in Engineering Software*. 112(11-12): 255-266, 2017.

[30] ASME. Manual for determining the remaining strength of corroded pipelines. In ASME B31G, American Society Mechanical Engineers: New York, NY, USA, 2012.

[31] DNV. Corroded pipelines. In Recommended Practice DNV-RP-F101; Det Norske Veritas: Oslo, Norway, 2008.

[32] Zolfaghari., A. and Izadi, M. Burst pressure prediction of cylindrical vessels using artificial neural network, *Journal of Pressure Vessel Technology*, 142(3):031303-1, 2020.

[33] Melenk, J.M. and Babuška, I. The partition of unity finite element method: basic theory and applications. *Computer Methods in Applied Mechanics and Engineering*, 139(1-4): 289–314, 1996.

[34] Belytschko T. and T. Black. Elastic crack growth in finite elements with minimal remeshing. *International Journal for Numerical Methods in Engineering*, 45, 601-620, 1999.

[35] Abaqus 6.14. Abaqus Analysis User's Guide, Dassault Systèmes, 2014.

[36] Lin, M., Li, Y., Cheng, J.J.R., Koduru, S., Kainat, M., Zhang, X. and Adeeb, S. Novel XFEM variable strain damage model for predicting fracture in small-scale SENT and full-scale pipe tests. *Engineering Fracture Mechanics*, 271(2):108628, 2022.

[37] Gairola, S and Ren, J. XFEM simulation of tensile and fracture behavior of ultrafine-grained AI 6061 alloy. *Metals*, 11(11):1761, 2021.

[38] Kawaguchi, S., Hagiwara, N., Masuda, T., Toyoda, M. Evaluation of leak-before-break (LBB) behavior for axially notched X65 and X80 line pipes. *Journal of Offshore Mechanics and Arctic Engineering*, 126 (4), 350–357, 2004.

[39] Canadian Standards Association (CSA). Z662-15. Oil and gas pipeline systems. CSA Group, Toronto, Ontario, Canada, 2015.

[40] Zhang, X., Lin, M., Kainat, M., Yoosef-Ghodsi, N., Leung, J.Y. and Adeeb, S. Influence of strain hardening model on the CorLAS^{TM} model for cracked pipelines. Paper No. IPC2022-868556, *Proceedings of the 2022 14th International Pipeline Conference*, *American Society of Mechanical Engineers,* Calgary, Canada, 2022.

[41] Fukushima, K. Cognitron: a self-organizing multilayered neural network. *Biological Cybernetics*, vol. 20, 1975. 700407.

[42] Ripley, B.D. Pattern Recognition and Neural Networks, Cambridge University Press, Cambridge, 1996.

[43] Kingma, D.P. and Ba, J. Adam: A method for stochastic optimization. *In Proceedings of the 3rd International Conference for Learning Representations*, San Diego, CA, USA, 2015.

[44] Amano, T. and Makino, H. Evaluation of leak/rupture behavior for axially part through-wall

notched high-strength line pipes. IPC 2012-90216, Proceedings of the ASME 9th International Pipeline Conference, Calgary, Alberta, Canada, 2012.

[45] Mannucci, G. and Harris, D. Fracture Properties of API X 100 Gas Pipeline Steels: final report, European Commission, Directorate-General for Research and Innovation, Publication Office, 2002.

[46] Ma, J., Zhang, F., Tuggle, J. Assessment of Fitness-for-Service for crack-in-corrosion Anomalies, Pipeline Research Council International (PRCI) draft report, 2018.

[47] Shih, C. F. and Hutchinson, J. W. Fully plastic solutions and large scale yielding estimates for plane stress crack problems. Report No. DEAP S-14, Harvard University, Cambridge, MA, July, 1975.

[48] Adeeb, S. The simplest way to share computational tools. MecSimCalc. Accessed in 2022, https://mecsimcalc.com/.

[49] Zhang, X. Artificial neural network model, Accessed on Jan 22nd, 2024, https://mecsimcalc.com/app/9519943/artificial_neural_network_model.

CHAPTER 7: CONCLUSIONS

This chapter summarizes the work conducted in this research and provides some recommendations for future work.

7.1 Summary and Conclusions of Research Work

Pipelines are designed and constructed to transport crude oil, natural gas, and other refined petroleum products from refineries to customers. Often buried underground as per regulation, pipelines are highly exposed to the harsh environment, making them susceptible to cracking. Compared to circumferential cracking, axial cracking causes more concerns to the pipeline integrity assessment when internal pressure is the primary loading condition. Although several analytical models have been developed to evaluate the failure pressure of pipelines containing axial external cracks, a notable bias exists between the predicted and test failure pressure, even when using the CorLAS^{TM} model, which is conceived to be the most accurate, as reported in the literature. To better capture the non-linear relationship between the input variables and improve the predictions, machine learning models, or the so-called data-driven models, have been introduced as alternatives to analytical models. The primary objective of this research is to develop a predictive model capable of predicting the failure pressure of pipelines with axial cracks using artificial neural network (ANN). A large database is generated through numerous XFEM simulations as a basis for training the ANN model.

The performance of CorLAS^{TM} version 1 and version 2 is examined based on 103 experimental data collected from the literature. It is observed that CorLAS^{TM} model version 2 (model error mean: 0.94 and CoV: 20.8%) exhibits similar accuracy to version 1 (model error mean: 0.96 and CoV: 22.8%). After excluding the less reliable datasets, the model error CoV of CorLAS^{TM} model version 2 is reduced to 13.9%. A detailed sensitivity study is then conducted to investigate the impact of various factors including pipe grade, pipe dimension, and crack size, on the probability of failure (PoF) with respect to safety factors while incorporating the obtained model error of CorLAS^{TM} version 2. The results reveal that PoFs are independent of pipe grade, pipe dimension, and crack size. However, model error CoV has a pronounced effect on PoFs of cracked pipes; the PoF increases significantly as the CoV increases.

The accuracy of some frequently used stress-strain formulas, namely Ludwik, Hollomon, Ludwigson, Ramberg-Osgood, and Swift, including the one used in CorLAS^{TM} is investigated using experimental data obtained from tensile tests conducted by the pipeline research group at the University of Alberta. Furthermore, a parametric study is conducted to evaluate the effect of strain-hardening exponent (n) on the failure pressure predicted by CorLAS^{TM} with four different crack

sizes (short and shallow, short and deep, long and shallow, and long and deep). The conclusions are summarized as follows:

(1) Compared to linear regression technique, the approximated stress-strain curves using non-linear regression technique better match the actual curves.

(2) All the stress-strain models, except the one used in CorLAS^{TM}, satisfactorily approximate the actual stress-strain curves.

(3) The effect of n on the CorLAS^{TM}-predicted failure pressure of pipelines with deep cracks (i.e., a/t = 0.7) is negligible, while it has a significant impact on pipelines with shallow cracks (i.e., a/t = 0.3).

Sensitivity studies are also performed to evaluate the effect of crack shape, crack profile, and XFEM damage parameters (MAXPE and Gc) on the ductile fracture behavior of cracked pipes. The following conclusions can be drawn:

(1) The stress distributions of a rectangular-shaped sharp crack and a blunted crack at failure are essentially the same, and their difference in the failure pressure is generally found to be insignificant and negligible for higher Gc values.

(2) A sharp crack requires a slightly higher force to initiate propagation compared to a blunted crack caused by the initial cohesion at the crack tip vicinity.

(3) The semi-elliptical crack exhibits a much higher failure pressure than the rectangular crack due to the smaller defect region.

(4) Failure pressure increases with the increase of the XFEM damage properties and is more sensitive to Gc.

The accuracy of XFEM in predicting the failure pressure of cracked pipelines is examined and validated by comparing XFEM predictions with more than 100 full-scale burst tests results. A comparison is made between the failure pressure predicted by the validated XFEM model and CorLAS^{TM}. The results demonstrate that XFEM results in more accurate predictions than CorLAS^{TM}, which provides a strong validation of the input data employed in the ANN model development. Extensive parametric analyses are conducted to investigate the effects of pipe and crack sizes on the failure pressures. It is observed that the failure pressure markedly reduces with the increase of pipe and crack sizes. The datasets generated from XFEM parametric analysis are

used for the development of the novel ANN model and the model is validated against 25 full-scale burst tests. The best-performing ANN architecture is found to have 36 neurons in the hidden layer. The fact that the mean and CoV of test-to-prediction ratio are 1.01 and 4.76%, indicates that the ANN predictions and experimental data are in excellent agreement.

7.2 Research Contributions and Highlights

The primary scientific contributions of this research work are summarized as follows:

(1) This research contributes a study of the model error distribution associated with the CorLAS^{TM} model and successfully reconciles the noticeable discrepancy between the two published studies. The results can provide a guidance on how to incorporate the model error of CorLAS^{TM} into the reliability-based assessment.

(2) This research presents several parametric studies to investigate the crack shape (i.e., shape and blunt) and crack profile (i.e., rectangular and semi-elliptical) on the ductile fracture response of cracked pipelines. The results demonstrate the importance in choosing the crack profile that closely represents the actual tests.

(3) A correlation between Charpy V-notch (CVN) impact energy and XFEM damage parameters (MAXPE and Gc) is established, which enables the direct selection of damage parameters without re-calibration, offering significant computation cost savings compared to the traditional approach. The developed correlation account for differences in crack profiles and can provide pipeline operators with valuable guidance for choosing appropriate XFEM damage parameters based on known CVN values.

(4) This research shows that XFEM is a robust approach in evaluating the cracked pipes and can produce more accurate failure pressure predictions than CorLAS^{TM} based on more than 100 full-scale burst tests collected from the open literature.

(5) This research develops a novel failure pressure predictive model using artificial neural network (ANN). To the best of the author's knowledge, although several crack assessment models are proposed, none of them can perfectly predict the failure pressure. This work is the first attempt to propose a predictive model using ANN based on the results generated from numerous XFEM simulations. The accuracy of this model is examined and validated against experimental tests and

the results indicate that the developed ANN model is an appropriate alternative to predict the failure pressure of pipelines with axial surface cracks subjected to internal pressure.

7.3 Recommendations for Future Work

Although this research has made several significant contributions to the scope of the work, there are limitations that need to be addressed to expand the applicable range of the proposed model, making it a more robust tool in assessing cracked pipes. Based on the limitations of this work, the recommendations for the future study are listed as follows.

(1) The developed ANN model in this research should only apply to thin-walled pipes with diameter-to-thickness ratio between 40 and 90, crack depth-to-thickness ratio ranging from 0.4 to 0.8, and squared of crack length-to-the multiplication of diameter and thickness ratio within the range of 1 to 18. It may not be suitable for pipes falling outside the range of the training data. Additional simulation results are suggested to widen the model applicable range.

(2) The defective pipes only consider the scenario of a single crack with an idealized shape on the pipe. Interacting defects (e.g., cracks occur coincidently with corrosion or a dent) and multiple cracks are also common in the field. It is highly recommended to further propose a predictive model that accounts for the interacting effects of hybrid and multiple defects on the burst capacity of cracked pipes.

(3) The cracked pipes in the analysis are loaded solely by the internal pressure. In reality, a pipe with crack can also be subjected to a combination of internal pressure and axial tension. Therefore, it is essential to consider a more comprehensive loading condition.

BIBLIOGRAPHY

Abaqus 6.14. Abaqus Analysis User's Guide, Dassault Systèmes, 2014.

Abdulhameed, D., Cakiroglu, C., Lin, M., Cheng, J.J.R., Nychka, J., Sen, M. and Adeeb, S. The Effect of Internal Pressure on the Tensile Strain Capacity of X52 Pipelines with Circumferential Flaws. Paper No. PVT-15-1045, *Journal of Pressure Vessel Technology*, 138(6):061701, 2016.

Adeeb, S. The simplest way to share computational tools. MecSimCalc. Accessed in 2022. https://www.mecsimcalc.com/app/.

Agbo, S., Lin, M., Amerli, I., Imanpour, A., Duan, D-M., Cheng, J.J.R. and Adeeb, S. Evaluation of the effect of internal pressure and flaw size on the tensile strain capacity of X42 vintage pipeline using damage plasticity model in extended finite element method (XFEM). Paper No. PVP2019-94005, *Proceedings of the Pressure Vessel and Piping Conference, American Society of Mechanical Engineers*, San Antonio, Texas, USA, 2019.

Agbo, S., Lin, M., Ameli, I., Imanpour, A., Duan, D-M., Cheng, J.J.R. and Adeeb, S. Experimental Evaluation of the Effect of the Internal Pressure and Flaw Size on the Tensile Strain Capacity of Welded X42 Vintage Pipelines. International Journal of Pressure Vessels and Piping, Vol. 173, pp. 55-67, 2019.

Amano, T. and Makino, H. Evaluation of leak/rupture behavior for axially part through-wall notched high-strength line pipes. Paper No. IPC 2012-90216, Proceedings of the ASME 9th International Pipeline Conference, *American Society of Mechanical Engineers*, Calgary, Alberta, Canada, 2012.

Anderson, T. Development of a Modern Assessment Method for Longitudinal Seam Weld Cracks. PRCI Catalogue No. PR-460-134506-R0. Pipeline Research Council International, Chantilly, 2015.

Anderson, T. Assessing crack-like flaws in longitudinal seam welds: a State-Of-The-Art Review. PRCI Catalogue No. PR-460-134506-R02. Pipeline Research Council International, Chantilly, 2017.

API RP 1176. Recommended practice for assessment and management of cracking in pipelines. API Publishing, Errata 1, 2021.

API. Specification for Line Pipe. ANSI/SPI Specification 5L/ISO 3183:2007, 44th Edition, October 1, 2007.

API 579-1/ASME FFS-1, Fitness-for-service, American Society of Mechanical Engineers, USA, 2019.

ASME. Manual for determining the remaining strength of corroded pipelines. In ASME B31G, American Society Mechanical Engineers: New York, NY, USA, 2012.

ASME B31.8-2010, Gas Transmission and Distribution Piping Systems.

Barsom, J.M. and Rolfe, S.T. Impact Testing of Metals, ASTM STP 466, *The American Society for Testing and Materials (ASTM)*, Philadelphia, PA, 1970, pp. 281-302.

Bedairi, B., Cronin, D., Hosseini, A. and Plumtree, A. Failure prediction for crack-in-corrosion defects in natural gas transmission pipelines, *International Journal of Pressure Vessels and Piping*, 96-97:90-99, 2012.

Belytschko T., and T. Black. Elastic crack growth in finite elements with minimal remeshing, *International Journal for Numerical Methods in Engineering*, Vol. 45, pp. 601620, 1999.

British Standards Institution. BS 7910. Guide to Methods for Assessing the Acceptability of Flaws in Metallic Structures. London, UK, 2019.

British Steel, SINTAP: Final Procedure: Structural Integrity Assessment Procedures for European Industry. European Union Brite-Euram Programme, Project number BE-1426, Contract number BRPR-CT95-0024, Rotherham, British, 1999.

Broek, D. Elementary engineering fracture mechanics, 3rd edition. Martinus Nijhoff Publishers, The Hague, 1982.

Canadian Standards Association (CSA). Z662-15 Oil and gas pipeline systems. CSA Group, Toronto, Ontario, Canada, 2015.

Canadian Standards Association (CSA). Oil and gas pipeline systems. CSA Standard Z662:19, Mississauga, Ontario, Canada, 2019.

Cazenave, P., Gao, M., Moneta, A, Cruzado, J. and Hryciuk, P. An onshore pipeline failure due to hydrogen assisted cracking induced by cathodic protection operated at near -1200 mV CSE – a case study. Paper No. IPC2020-9396, *Proceedings of the 2020 13th International Pipeline Conference, American Society of Mechanical Engineers*, Virtual, Online, 2020.

CBC News. Pipelines and why they fail in Canada. https://www.cbc.ca/news/business/cepa-2016-safety-report-1.3654640, Accessed on May 1st, 2022.

Cosham, A., Hopkins, P. and Leis, B. Crack-like defects in pipelines: the relevance of pipeline-specific methods and standards, Paper No. IPC2012-90459, *Proceedings of International Pipeline Conference*, *American Society of Mechanical Engineers*, Calgary, Canada, 2012.

Cosham, B.J., Eldred, M.S., Swiler, L.P., Mahadevan, S. and McFarland, J.M. Multimodal reliability assessment for complex engineering applications using efficient global optimization, AIAA Paper No. AIAA-2007-1946, 2007.

Cravero, S. and Ruggieri, C. Structural integrity analysis of axially cracked pipelines using conventional and constraint-modified failure assessment diagrams, *International Journal of Pressure Vessel and Piping*, 83(8): pp. 607-17, 2006.

Crussard, C.H. and Jaoul, B. Contribution à l'étude de la forme des courbes de traction des me'taux et à son interprétation physique. *Materials Science Revue De Metallurgie*, 47(8): pp. 589-600, 1950.

Daily Telegraph. West Ryde water main bursts again. Accessed on April 6th, 2022. https://www.dailytelegraph.com.au/newslocal/news/burst-water-main-near-goodwin-st-in-west-ryde-causes-havoc-this-afternoon/news-story/5de15aadf548ed48bc9c07a761362134.

Dassault Systèmes, 2022. Abaqus documentation.

Demofonti, G., Mannucci, G., Barsanti, L., Spinelli, C.M. and Hillenbrand, H.G. Fracture behaviour and defect evaluation of large diameter, HSLA steels, very high pressure linepipes, Paper No. IPC2000-168, *Proceedings of the 3rd International Pipeline Conference, American Society of Mechanical Engineers*, Calgary, Canada, 2000.

Det Norske Veritas (DNV). Corroded pipelines. In Recommended Practice DNV-RP-F101; Det Norske Veritas: Oslo, Norway, 2008.

Det Norske Veritas (DNV). Submarine Pipeline Systems: Offshore standard DNV-OS-F101, 2012.

EDF Energy. R6: Assessment of the Integrity of the Structures Containing Defect. Gloucester, UK amendment 10 R6, revision 5, 2013.

Eiber, R.J. and Kiefner, J.F. Failures of pipelines, Failure Analysis and Prevention, Vol 11, Edited by Becker, W.T. and Shipley, R.J. *ASM International*, 2002.

Fathi, A. Effects of material anisotropy on the buckling resistance of high strength steel pipelines. PhD Thesis. University of Alberta, Edmonton, Canada. 2012.

Fukushima, K. Cognitron: a self-organizing multilayered neural network. *Biological Cybernetics*, vol. 20, 1975.

Gairola, S. and Jayaganthan, R. XFEM simulation of tensile and fracture behavior of ultrafine-grained AI 6061 alloy. *Metals*, 11(11):1761, 2021.

Garwood, S.J., Willoughby, A.A. and Rietjens, P. The application of CTOD methods for safety assessment in ductile pipeline steels. In: International Conference on Fitness for Purpose Validation of Welded Constructions, London, UK; 1981.

Haddad, M. Integration of XFEM and CZM to model 3D multiple-stage hydraulic fracturing in quasi-brittle shale formations: Solution-dependent propagation direction. *Proceedings of the 2015 AADE National Technical Conference and Exhibition*, San Antonio, Texas, USA, 2015.

Hart Energy. Accessed in 2024. Not every pipeline repair is equally urgent. How can pipeline operators tell the difference? https://www.hartenergy.com/exclusives/better-prediction-30439#:~:text=A%20small%2C%20shallow%20crack%20typically,to%20develop%20until%20failure%20occurs.

Hertelé, S., Waele, W.D. and Denys, R. A Generic Stress-strain Model for Metallic Materials with Two-stage Strain Hardening Behavior. *International Journal of Non-Linear Mechanics*, 46(3): pp. 519-531, 2011.

Hill, H.N. Determination of stress-strain relations from “offset” yield strength values. NACA Technical Note No. 927, Washington, D.C., 1944.

Hollomon, J.R. Tensile deformation. *Transaction of the Metallurgical Society of AIME*, Vol. 162, pp. 268-290, 1945.

Hosseini, A., Cronin, D., Plumtree, A. and Kania, R. Experimental testing and evaluation of crack defects in line pipe, Paper No. IPC2010-31158, *Proceedings of the 8th International Pipeline Conference*, *American Society of Mechanical Engineers*, Calgary, Canada, 2010.

Ibrahim, M., Doucette, K., Hassanien, S. and Langer, D. Effect of model error on reliability analysis of surface cracks, Paper No. IPC2018-78237, *Proceedings of the 12th International Pipeline Conference, American Society of Mechanical Engineers*, Calgary, Canada, 2018.

Irwin, G.R. Analysis of stresses and strains near the end of a crack traversing a plate. *Journal of Applied Mechanics*, 24:361–364, 1957.

Irwin, G.R. The crack extension force for a part-through crack in a plate, *Journal of Applied Mechanics*, 30(3): pp, 651-654, 1963.

Jaske, C.E., Beavers, J.A. and Harle, B.A. Effect of stress corrosion cracking on integrity and remaining life of natural gas pipelines, Paper No. 255, Corrosion 96, NACE International, Houston, 1996.

Jaske, C. E. and Beavers, J. A. Integrity and Remaining Life of Pipe with Stress Corrosion Cracking, PRCI 186-9709, Catalog No. L51928. Pipeline Research Council International, Falls church, 2001.

Jaske, C. E. and Beavers, J.A. Review and proposed improvement of a failure model for SCC of pipelines, Paper No. IPC1998-2051, *Proceedings of 2nd International Pipeline Conference, American Society of Mechanical Engineers,* Calgary, Canada, 1998.

Jaske, C. E. and Beavers, J.A. Development and evaluation of improved model for engineering critical assessment of pipelines, Paper No. IPC2002-27027, *Proceedings of 4th International Pipeline Conference*, *American Society of Mechanical Engineers,* Calgary, Canada, 2002.

Jaske, C.E., Polasik, S.J. and Maier, C.J. Inelastic fracture mechanics model for assessment of crack-like flaws, Paper No. PVP2011-57099, *Proceedings of the Pressure Vessels & Piping Conference*, *American Society of Mechanical Engineers,* Baltimore, Maryland, USA, 2011.

Kawaguchi, S., Hagiwara, N., Masuda, T., Toyoda, M. Evaluation of leak-before-break (LBB) behavior for axially notched X65 and X80 line pipes. *Journal of Offshore Mechanics and Arctic Engineering*, 126 (4), 350–357, 2004.

Keller, H.P., Junker, G. and Merker, W. Fracture analysis of surface cracks in cylindrical pressure vessels applying the two parameter fracture criterion (TPFC), *International Journal Pressure Vessels and Piping*, 29(2): pp. 113-153, 1987.

Kiefner, J.F., Maxey, W.A., Eiber, R.J. and Duffy, A.R. Failure stress levels of flaws in pressurized cylinders, Progress in flaw growth and fracture toughness testing, STP 536, *ASTM International*, West Conshohocken, PA, pp. 461-481, 1973.

Kiefner, J.F. Modified equation aids integrity management. *Oil & Gas Journal*. 106 (37), 78–82, 2008a.

Kiefner, J.F. Modified ln-secant equation improves failure prediction. *Oil & Gas Journal*. 106 (38), 64–66, 2008b.

Kingma, D.P. and Ba, J. Adam: A method for stochastic optimization. *In Proceedings of the 3rd International Conference for Learning Representations*, San Diego, CA, USA, 7–9 May, 2015.

Kobayashi, A. S., Ziv, M. and Hall, L. R. Approximate stress intensity factor for an embedded elliptical crack near to parallel free surfaces, *International Journal of Fracture Mechanics 1*, pp.81-95, 1965.

Kweon, H.D., Kim, J.W., Song, O. and Oh, D. Determination of true stress-strain curve of type 304 and 316 stainless steels using a typical tensile test and finite element analysis, *Nuclear Engineering and Technology*, 53(2): pp. 647-656, 2021.

Lavakumar, A., Sarangi, S.S., Chilla, V., Narsimhachary, D. and Ray, R.K. A “new” empirical equation to describe the strain hardening behavior of steels and other metallic materials. *Materials Science and Engineering A*, 802(2021)140641.

Leis, B. N., and Ghadiali, N. D., Pipe Axial Flaw Failure Criteria – PAFFC. Version 1.0 User’s Manual and Software, Topical Report to the Line Pipe Research Supervisory Committee of the Pipeline Research Committee of the American Gas Association, NG-18, Catalog No. L51720, May 1994.

Liessem, A. Strain based design-what the contribution of a pipe manufacturer can be. Paper No. ISPOE-I-07-500, *The Seventeenth International Offshore and Polar Engineering Conference*, Lisbon, Portugal, July 2007.

Lin, M. Characterization of tensile and fracture properties of X52 steel pipes and their girth welds. MSc Thesis, University of Alberta, Edmonton, Canada, 2015.

Lin, M., Agbo, S., Cheng, J.J.R., Yoosef-Ghodsi, N. and Adeeb, S. Application of the extended finite element (XFEM) to simulate crack propagation in pressurized steel pipes. Paper No. PVP2017-65575, *Proceedings of the Pressure Vessel and Piping Conference, American Society of Mechanical Engineers*, Hawaii, USA, 2017.

Lin, M., Li, Y., Cheng, J.J.R., Koduru, S., Kainat, M., Zhang, X. and Adeeb, S. Novel XFEM variable strain damage model for predicting fracture in small-scale SENT and Full-scale Pipe Tests. *Engineering Fracture Mechanics*, 271(2):108628, 2022.

Liu, X. Xia, M. Bolati, D. Liu, J. Zheng, Q. and Zhang, H. An ANN-based failure pressure prediction method for buried high-strength pipes with stray current corrosion effect. *Energy Science & Engineering*. 8(8), 248–259, 2020.

Ludwigson, D.C. Modified stress-strain relation for FCC metals and alloys. *Metallurgical and Materials Transactions B*, 2(10): pp. 2825-2828, 1971.

Ludwik, P. Elemente der Technologischen Mechanik. Verlag Von Julius Springer, Berlin, 1909.

Ma, J., Zhang, F., Tuggle, J. Assessment of fitness-for-service for crack-in-corrosion anomalies, Pipeline Research Council International (PRCI), draft report, 2018.

Malíková, L., Razavi, N. and Berto, F. Crack propagation in a brittle DCB specimen assessed by means of the Williams' power expansion. Frattura ed Integrità Strtturale, 13(48), 34-41, 2019.

Mannucci, G. and Harris, D. Fracture properties of API X100 gas pipeline steels: final report, European Commission, Directorate-General for Research and Innovation, Publication Office, 2002.

Maxey, W.A., Kiefner, J.F., Eiber, R.J., Duffy, A.R. in The Fifth National Symposium on Fracture Mechanics, University of Illinois, 1971.

MechaniCalc. Mechanical Properties of Materials. Accessed in March 2022. https://mechanicalc.com/reference/mechanical-properties-of-materials.

Melenk, J.M. and Babuška, I. The partition of unity finite element method: basic theory and applications, *Computer Methods in Applied Mechanics and Engineering*, 139(1-4): 289–314, 1996.

Moghaddam, H.N., Keyhani, A. and Aghayan, I. Modeling of Crack Propagation in Layered Structures Using Extended Finite Element Method. Civil Engineering Journal, 2(5):180-188, 2016.

Moon, D.H., Par, J.Y. and Kim, M.H. Effects of the crack tip constraint on the fracture assessment of an AI5083-O weldment for low temperature applications. *Materials*, 10(7), 815, 2017.

Natural Resources Canada (NRCan). Pipelines across Canada. https://www.nrcan.gc.ca/our-natural-resources/energy-sources-distribution/clean-fossil-fuels/pipelines/pipelines-across-canada/18856, Accessed on May 1st, 2022.

Nutor, R.K., Adomako, N.K. and Fang, Y.Z. Using the Hollomon model to predict strain-hardening in metals. *American Journal of Materials Synthesis and Processing*, 2(1): pp. 1-4, 2017.

Oh, D. Race, J., Oterkus, S. and Koo, B. Burst pressure prediction of API 5L X-grade dented pipelines using deep neural network, *Journal of Marine Science and Engineering*, 8(10), 766, 2020.

Okodi, A., Lin, M., Yoosef-Ghodsi, N., Kainat, M., Hassanien, S. and Adeeb, S. Crack propagation and burst pressure of longitudinally cracked pipelines using extended finite element method. *International Journal of Pressure Vessels and Piping*, 184(5): 104115, 2020.

Okodi, A., Li, Y., Cheng, J.J.R., Kainat, M., Yoosef-Ghodsi, N. and Adeeb, S. Effect of location of crack in dent on burst pressure of pipelines with combined dent and crack defects. Journal of Pipeline Science and Engineering, 1(2): 252-263, 2021.

Paris, P.C and Sih, G.C. Stress analysis of cracks, ASTM STP 381, pp, 30-81, 1965.

PD 8010-1:2015: Pipeline systems. Steel pipelines on land. Code of practice, 2015.

Pipeline and Hazardous Materials Safety Administration (PHMSA) of USA, 2019. Pipeline safety: safety of gas transmission pipelines. Docket No. PHMSA-2011-0023.

Polasik, S.J., Jaske, C.E. and Bubenik, T.A. Review of engineering fracture mechanics model for pipeline applications. Paper No. IPC2016-64605, *Proceedings of the 11th International Pipeline Conference, American Society of Mechanical Engineers*, Calgary, Canada, 2016.

Ramberg, W and Osgood, W.R. Description of stress-strain curves by three parameters. Technical Note No.902, National Advisory Committee For Aeronautics, Washington DC, 1943.

Rana, M.D., Smith, J.H., Tribolet, R.O. Technical basis for flawed cylinder test specification to assure adequate fracture resistance of ISO high-strength steel cylinder. *Journal of Pressure Vessel Technology*, 119 (4), 475–480, 1997.

Rasmussen, K.J.R. Full-range stress-strain curves for stainless steel alloys. *Journal of Constructional Steel Research*, 59(1): pp. 47-61, 2003.

Reed-Hill, R.E., Cribb, W.R. and Monteiro, S.N. Concerning the analysis of tensile stress-strain data using Log (dσ/dεp) versus Log σ diagrams. *Metallurgical Transaction,* Vol. 4: pp. 2665-2667, 1973.

Rice, J.R. A path independent integral and the approximate analysis of strain concentration by notches and cracks. *Journal of Applied Mechanics*, 35:379–386, 1968.

Ripley, B.D. Pattern recognition and neural networks, Cambridge University Press, Cambridge, 1996.

Rolfe, S.T. and Novak, S.R. Review of developments in plane-strain fracture toughness testing, ASTM STP 463, *The American Society for Testing and Materials (ASTM)*, Philadelphia, PA, pp. 124-159, 1970.

Rothwell, A.B. and Coote, R.I. A critical review of assessment methods for axial planar surface flaws in pipe, *Proceedings of the International Conference on Pipeline Technology*, Ostend, Belgium, 2009.

Samadian, K., Hertele, S. and Waele, W.D. Using 3D digital image correlation (3D-DIC) to measure CTOD in a semi-elliptical surface crack. *The Eighteenth International Conference of Experimental Mechanics*, 2(8):5311, 2018.

Samuel, K.G. Limitations of Hollomon and Ludwigson stress-strain relations in assessing the strain hardening parameters. *Journal of Physics D: Applied Physics*, 39(1): pp. 203-212, 2005.

Selin, M. Comparing three equations used for modeling the tensile flow behavior of compacted graphite cast irons at elevated temperatures. *Metallurgical and Materials Transactions A*, 41(11): pp. 2805-2815, 2010.

Shih, C. F. and Hutchinson, J. W. Fully plastic solutions and large scale yielding estimates for plane stress crack problems, Report No. DEAP S-14, Harvard University, Cambridge, MA, July, 1975.

Smart, L.J. Review of materials property data for nondestructive characterization of pipeline materials, MSc Thesis, Iowa State University, 2015.

Staat, M. Plastic collapse analysis of longitudinally flawed pipes and vessels, *Nuclear Engineering and Design*, 234(1-3): pp. 25-43, 2004.

Swift, H.W. Plastic instability under plane stress. *Journal of the Mechanical and Physics of Solids*, 1(1): pp. 1-18, 1952.

Tandon, S., Gao, M., Krishnamurthy, R., Kariyawasam, S. and Kania, R. Evaluation of existing fracture mechanics models for burst pressure predictions, Theoretical and Experimental Aspects, Paper No. IPC2014-33563, *Proceedings of the 2014 10th International Pipeline Conference*, *American Society of Mechanical Engineers,* Calgary, Canada, 2014.

Tosun, E. and Calik, A. Failure load prediction of single lap adhesive joints using artificial neural networks. Alexandria Engineering Journal, 55(2), 1341-1346, 2016.

Tu, X.Y., Ren, Y., Shi, X.B., Li, C.S., Yan, W., Shan, Y.Y. and Yang, K. Enhancing strain capacity by the introduction of pearlite in bainite and polygonal ferrite dual-phase pipeline steel. *Materials*, 14(18):5358, 2021.

Tu, S.W., Ren, X.B., He, J.Y. and Zhang, Z.L. Stress-Strain curves of metallic materials and post-necking strain hardening characterization: A Review. *Fatigue and Fracture of Engineering Materials and Structures*, 43(3), 1-17, 2019.

Utilities Kingston. Water main breaks. https://utilitieskingston.com/Water/mainbreaks, Accessed on December 10th, 2022.

Wang, K.C. and Smith, E.D. The effect of mechanical damage on fracture initiation in linepipe: part II e gouges. Canadian Centre for Mineral and Energy Technology (CANMET); 1988. Report ERP/PMRL 88e16 (TR), Canada.

Wells, A.A. Application of fracture mechanics at and beyond general yielding. British Welding Research Association Report M13/63, *British Welding Journal*, 10:563–570, 1963.

Wilkowski, G.M., Ahmad, J., et al. Degraded piping program: Phase II, Semiannual report, April 1986 – September 1986, NUREG/CR-4082, Volume 5, 1987.

Willems, H. and Hennig, T. Recent improvements regarding ultrasonic crack inspection of pipelines, Pigging Products & Services Association, NDT Global, 2017.

Xu, W., Li, C.B., Choung, J. and Lee, J. Corroded pipeline failure analysis using artificial neural network scheme. *Advances in Engineering Software*. 112(11-12): 255-266, 2017.

Yan, Z., Zhang, S. and Zhou, W. Model error assessment of burst capacity models for energy pipelines containing surface cracks, *International Journal of Pressure Vessels and Piping*, 120-121: pp. 80-92, 2014.

Yan, J., Zhang, S., Kariyawasam, S., Pino, M. and Liu, T. Validate crack assessment models with in-service and hydrotest failures, Paper No. IPC2018-78251, *Proceedings of the 2018 12th International Pipeline Conference*, *American Society of Mechanical Engineers*, Calgary, Canada, 2018.

Zhang, X., Okodi, A., Tan, L., Leung, J.Y. and Adeeb, S. Failure pressure prediction of crack in corrosion defects in 2D by using XFEM. Paper No. PVP2020-21046, *Proceedings of the Pressure Vessel and Piping Conference, American Society of Mechanical Engineers*, Virtual, Online, 2020.

Zhang, X., Okodi, A., Tan, L., Leung, J.Y. and Adeeb, S. Failure pressure prediction of crack in corrosion defects using XFEM. Paper No. IPC2020-9312, *Proceedings of the 13th International Pipeline Conference, American Society of Mechanical Engineers*, Virtual, Online, 2020.

Zhang, X., Lin, M., Okodi, A., Tan, L., Leung, J.Y. and Adeeb, S. Numerical analysis of API X42 and X52 vintage pipes with cracks in corrosion defects using extended finite element method. *Journal of Pressure Vessel Technology*, 143(6):061302, 2021.

Zhang, X., Zheng, Q., Leung, J.Y. and Adeeb, S. Reliability-based Assessment of Cracked Pipelines using Monte Carlo Simulation Technique with CorLAS^{TM}. Paper No. PVP2022-80412, *Proceedings of the Pressure Vessel and Piping Conference, American Society of Mechanical Engineers*, Las Vegas, USA, 2022.

Zhang, X., Yoosef-Ghodsi, N., Kainat, M., Leung, J.Y. and Adeeb, S. Influence of Strain Hardening Model on the CorLAS^{TM} Model for Cracked Pipelines. Paper No. PVP2024-121892, Forthcoming, *Proceedings of the Pressure Vessel and Piping Conference American Society of Mechanical Engineers*, Washington, USA, 2024.

Zhang, X. Artificial neural network model. Accessed on Jan 22nd, 2024, https://mecsimcalc.com/app/9519943/artificial_neural_network_model.

Zheng, Q., Abdelmoety, A.K., Li, Y., Kainat, M., Yoosef-Ghodsi, N. and Adeeb, S. Reliability analysis of intact and defected pipes for internal pressure related limit states specified in CSA Z622:19, *International Journal of Pressure Vessels and Piping*, 192(2021) 104411.

Zolfaghari., A. and Izadi, M. Burst pressure prediction of cylindrical vessels using artificial neural network, *Journal of Pressure Vessel Technology*, vol. 142, 2020.

APPENDIX A: DETAILS OF 103 FULL-SCALE BURST TESTS

No.	D (mm)	t (mm)	a (mm)	L (mm)	σ_{YS} (MPa)	σ_{UTS} (MPa)	A_c (mm^2)	CVN (J)	Shape	Reference
1	762	9.8	5.99	219.2	420.595	563.322	53.33	40.67	R	[9]
2	762	9.73	5.92	369.82	420.595	563.322	53.33	40.67	R	
3	762	9.96	9.17	224.03	420.595	563.322	53.33	40.67	R	
4	762	9.58	7.75	224.03	417.837	560.564	53.33	36.61	R	
5	762	9.65	5.84	83.82	394.394	530.915	53.33	39.32	R	
6	762	9.65	5.84	83.82	394.394	530.915	53.33	39.32	R	
7	762	9.27	3.56	370.84	440.591	575.043	53.33	36.61	R	
8	762	9.63	3.91	222.25	440.591	575.043	53.33	36.61	R	
9	762	9.63	3.91	83.82	440.591	575.043	53.33	36.61	R	
10	762	9.88	8.1	370.84	439.901	553.669	53.33	40.67	R	
11	762	9.88	8.05	86.36	439.901	553.669	53.33	40.67	R	
12	914.4	10.03	5.13	84.58	509.541	632.961	53.33	29.83	R	
13	914.4	10.12	5.13	153.16	504.025	633.651	53.33	28.47	R	
14	914.4	11.15	6.83	139.7	379.225	536.431	53.33	37.96	R	
15	914.4	11.3	8.66	139.7	379.225	536.431	53.33	37.96	R	
16	914.4	9.73	4.95	190.5	475.755	618.482	53.33	29.83	R	
17	762	9.14	4.67	152.4	448.175	583.317	53.33	27.12	R	
18	762	9.32	4.57	152.4	448.175	583.317	53.33	27.12	R	
19	762	9.47	4.52	152.4	448.175	583.317	53.33	27.12	R	
20	914.4	9.79	5.08	228.6	474.376	601.002	53.33	18.98	R	
21	914.4	9.98	7.62	213.36	449.554	609.518	53.33	31.18	R	
22	914.4	9.98	7.54	121.92	449.554	609.518	53.33	31.18	R	
23	762	15.49	10.89	406.4	456.449	627.445	53.33	42.03	R	
24	762	15.65	10.87	406.4	456.449	627.445	53.33	42.03	R	
25	863.6	12.8	3.22	406.4	465.413	613.655	53.33	17.63	R	
26	863.6	12.93	11.22	609.6	465.413	613.655	53.33	17.63	R	
27	863.6	12.93	10.69	609.6	465.413	613.655	53.33	17.63	R	
28	914.4	10.57	4.32	165.1	456.449	609.518	53.33	33.9	R	
29	914.4	10.26	5.21	111.76	449.554	609.518	53.33	31.18	R	
30	1066.8	10.26	6.5	165.1	435.075	586.075	53.33	29.83	R	
31	914.4	9.83	6.85	152.4	484.719	610.208	53.33	16.27	R	
32	914.4	10.67	7.49	63.5	423.353	587.454	53.33	36.61	R	
33	914.4	11.12	7.57	127	397.842	562.632	53.33	46.1	R	
34	88.9	4	1.1	66	336	486	80	76	S	[18]
35	88.9	4	1	116	336	486	80	76	S	
36	88.9	4	2	20	336	486	80	76	S	
37	88.9	4	2.3	27	336	486	80	76	S	
38	88.9	4	2	72	336	486	80	76	S	
39	88.9	4	2	122	336	486	80	76	S	
40	88.9	4	2	222	336	486	80	76	S	
41	88.9	4	2.1	220	336	486	80	76	S	
42	88.9	4	2.8	75	336	486	80	76	S	
43	88.9	4	3	125	336	486	80	76	S	
44	88.9	4	3.1	85	336	486	80	76	S	
45	88.9	4	3.6	40	336	486	80	76	S	
46	88.9	4	3.6	30	336	486	80	76	S	
47	88.9	4	8.2	200	324	457	80	33	S	
48	711.2	8.2	7.8	205	543	695	80	50	S	
49	711.2	8.2	7.5	210	543	695	80	50	S	
50	711.2	8.2	7.14	200	543	695	80	50	S	
51	711.2	8.2	6.2	250	543	695	80	50	S	
52	914.4	10.6	9.2	200	529	670	80	115	S	
53	914.4	10.6	7.2	250	529	670	80	115	S	
54	88.9	4	3.7	20	246	570	80	84	S	
55	88.9	4	3.8	20	246	570	80	84	S	
56	88.9	4	3.1	90	246	570	80	84	S	

(*continued on next page*)

(*Continued*)

No.	D (mm)	t (mm)	a (mm)	L (mm)	σ_{YS} (MPa)	σ_{UTS} (MPa)	A_c (mm^2)	CVN (J)	Shape	Reference
57	88.9	4	3.7	30	246	570	80	84	S	
58	88.9	4	3.7	40	246	570	80	84	S	
59	88.9	4	3.5	50	246	570	80	84	S	
60	88.9	4	3.6	60	246	570	80	84	S	
61	88.9	4	3.5	80	246	570	80	84	S	
62	88.9	4	3.5	80	246	570	80	84	S	
63	508	15.8	3	60	483	597	80	135	S	[19]
64	508	15.8	7	140	483	597	80	135	S	
65	508	15.8	10	200	483	597	80	135	S	
66	1422.5	19.1	10.4	180	740	774	80	261	R	[20]
67	1422.5	19.1	3.8	385	795	840	80	171	R	
68	508	5.7	2.2	200	433	618	80	65	S	[21]
69	508	5.7	2.7	200	433	618	80	81	S	
70	508	5.7	2.7	200	433	618	80	76	S	
71	508	5.7	2.9	200	433	618	80	68	S	
72	564.8	18.4	16.8	218	798	922	80	78	S	[22]
73	564	18	9.3	144	778	925	80	59	S	
74	566	18	11.6	215	703	847	80	80	S	
75	565.6	17.8	15.8	150	751	886	80	79	S	
76	564.8	20.4	16.1	96	878	990	80	64	S	
77	565.4	21.7	14.5	65	866	979	80	65	S	
78	565.2	17.6	14.6	64.6	813	944	80	59	S	
79	565	17.5	13	94	859	982	80	77	S	
80	564.8	18.4	14.7	155	853	973	80	75	S	
81	567	18.5	10.7	143	842	985	80	63	S	
82	565.4	17.7	9	215	830	984	80	65	S	
83	565.6	17.8	10	142	726	879	80	81	S	
84	565.4	18.7	13.5	93	843	976	80	76	S	
85	571.4	17.7	13.1	160	831	947	80	68	S	
86	565.2	17.6	11.6	205	832	951	80	68	S	
87	323.9	5.8	5.3	850	431	512	80	50.8	IR	[23]
88	323.9	5.7	4.5	120	409	488	80	28.6	IR	
89	323.9	5.6	4.1	130	390	463	80	15.2	IR	
90	323.9	5.8	4.4	210	403	521	80	47.2	IR	
91	323.9	5.8	3.5	380	416	520	80	45.3	IR	
92	323.9	5.6	3.5	120	391	482	80	27.5	IR	
93	323.9	5.1	1.5	612	443	499	80	51.1	IR	
94	323.9	5.3	5.0	140	421	500	80	35	IR	
95	508	9.65	2.39	162	418	567	60	25	S	[24]
96	508	9.88	1.8	190	418	567	60	25	S	
97	508	9.88	2.01	200	418	567	60	25	S	
98	508	9.88	2.13	200	418	567	60	25	S	
99	508	5.56	2.54	179	415	520	40	21	S	
100	508	5.56	1.98	180	415	520	40	21	S	
101	508	5.56	2.21	185	415	520	40	21	S	
102	900	13	5.4	234	438	584	80	40	S	[25]
103	900	13	4.54	87	438	584	80	40	S	

Note:

1. In the shape column, S denotes semi-elliptical, R denotes rectangular, and IR denotes irregular crack profiles, respectively.
2. Young's modulus is assumed to be 210 GPa.

APPENDIX B: CODE OF RELIABILITY CALCULATION USING MONTE CARLO SIMULATION

The following MATLAB code is used to calculate the reliability of pipes with the inclusion of CorLAS^{TM} model error in Chapter 2.

```
%% Import data: basic variables & Parameter definition
nS = 1e4; % number of CMC for one time
% Loop = 100; % number of loop time of CMC
SF = 1.00: 0.1: 1.4; % range of concerned safety factor
Fd = 1; % Parameters in failure pressure calculation based on the flow stress criterion
Ft = 1;
Ratio_dt = 0.3;
Ratio_Ld = 20;
for num = 1:1
% for num = 1:1
    count = 1;
    choose = sheet(num);

    %% Parameter definition
    % Pipe geometry
    D = {UniquePDT(:,2), 'Normal', UniquePDT(:,2)*1, 0.0006};
    WT = {UniquePDT(:,3), 'Normal', UniquePDT(:,3)*1.01, 0.01};
    % Pipe material
    SMYS = UniquePDT(:,1); % psi
    E = {30457926, 'Normal', 30457926, 0.04}; % Youngs' modulus, psi
```

```
CVN = {37, 'Normal', 30.24, 0.14};
flaw_location = 'E'; % Flaw location can be 'I'(internal) or 'E'(external)
shape = 'E'; % Shape can be 'R'(rectangular) or 'E'(elliptical)
% Operation parameter
Rp = {1.03, 'Gumbel', 1.03, 0.01}; % nominal, distribution, mean, COV
% CorLAS™ Model error
Rtp = {1.07, 'Normal', 1.07, 0.14};
%% Definition of each data sample
for num1 = 1: size (UniquePDT,1)
    if SMYS (num1) == 80000
        flow_definition = 'Other'; % Flow_definition can be '1e4'(for pipe grade lower than X70) or 'Other'(for pipe grade equal or higher than X70)
        Sy = {SMYS (num1), 'Normal', SMYS (num1)*1.07, 0.036*SMYS(num1)*1.07};% unit:psi, nominal, distribution, mean, sigma
        sigmaU = 90000; % SMTS, psi
        Su = {sigmaU, 'Normal', 1.12*sigmaU, 0.035*1.12*sigmaU}; % unit:psi, nominal, distribution, mean, sigma
    elseif SMYS (num1) == 70000
        flow_definition = 'Other'; % Flow_definition can be '1e4'(for pipe grade lower than X70) or 'Other'(for pipe grade equal or higher than X70)
        Sy = {SMYS (num1), 'Normal', SMYS (num1)*1.11, 0.035*SMYS(num1)*1.1};% unit:psi, nominal, distribution, mean, sigma
        sigmaU = 82000; % SMTS, psi
        Su = {sigmaU, 'Normal', 1.12*sigmaU, 0.035*1.12*sigmaU}; % unit:psi, nominal, distribution, mean, sigma
    elseif SMYS (num1) == 65000
        flow_definition = '1e4';
```

```
    Sy = {SMYS (num1), 'Normal', SMYS (num1)*1.08, 0.033*SMYS (num1)*1.08};
    sigmaU = 77000;
    Su = {sigmaU, 'Normal', 1.12*sigmaU, 0.035*1.12*sigmaU};
elseif SMYS (num1) == 60000
    flow_definition = '1e4';
    Sy = {SMYS (num1), 'Normal', SMYS (num1)*1.11, 0.034*SMYS (num1)*1.11};
    sigmaU = 75000;
    Su = {sigmaU, 'Normal', 1.12*sigmaU, 0.035*1.12*sigmaU};
elseif SMYS (num1) == 52000
    flow_definition = '1e4';
    Sy = {SMYS (num1), 'Normal', SMYS(num1)*1.1, 0.035*SMYS(num1)*1.1};
    sigmaU = 66000;
    Su = {sigmaU, 'Normal', 1.12*sigmaU, 0.03*1.12*sigmaU};
elseif SMYS (num1) == 42000
    flow_definition = '1e4';
    Sy = {SMYS (num1), 'Normal', SMYS(num1)*1.1, 0.035*SMYS(num1)*1.1};
    sigmaU = 60000;
    Su = {sigmaU, 'Normal', 1.12*sigmaU, 0.03*1.12*sigmaU};
end

%% Generate data by Crude Monte Carlo
time1 = clock; % starting time of Pf calculation
data_CVN = normrnd(CVN{3},CVN{3}*CVN{4},nS,1); %CVN is normal
data_D = normrnd(D{3}(num1),D{3}(num1)*D{4},nS,1); % D is normal
data_WT = normrnd(WT{3}(num1),WT{3}(num1)*WT{4},nS,1); %WT is normal
```

```
data_Sy = normrnd(Sy{3},Sy{4},nS,1); %SigmaY is normal

data_Su = normrnd(Su{3},Su{4},nS,1); %SigmaY is normal

data_E = normrnd(E{3}, E{3}*E{4}, nS, 1); %E is normal

flaw_depth = Ratio_dt.*data_WT;

flaw_length = Ratio_Ld.* flaw_depth;

%% Calculate the failure pressure based on the flow stress criterion

% Calculate flow strength

sigmaFL=(data_Sy+10000).*(strcmp(flow_definition,'1e4'))+((data_Sy+data_Su)/2.)*(strcmp(fl
ow_definition,'Other'));

% Calculate effective flaw area depending on rectangular or elliptical

A_Eff = (flaw_length.*flaw_depth).*(strcmp(shape,'R')
)+(pi*flaw_length.*flaw_depth./4.)*(strcmp(shape,'E'));

A = (flaw_depth).*(strcmp(shape,'R') )+(4*A_Eff./(pi*flaw_length)).*(strcmp(shape,'E'));

% Calculate Folias factor

M = ((1+0.6275*flaw_length.^2./(data_D.*data_WT)-
0.003375*flaw_length.^4./(data_D.*data_WT).^2).^0.5).*(flaw_length.^
2./(data_D.*data_WT)<= 50)...

+(3.3+0.032*flaw_length.^2./(data_D.*data_WT)).*(flaw_length.^2./(data_D.*data_WT)>50);

% Calculate y factor

y = 0.4.*(data_D./(2*data_WT)<=10)+0.*(data_D./(2*data_WT)> 10);

% Calculate reference area

A0 = flaw_length.*data_WT;

Pressure_f1 = Fd*Ft*sigmaFL.*((1-A_Eff./A0)./(1-
A_Eff./(M.*A0))).(data_D./(2*data_WT)-y); % Calculate failure pressure


%% Calculate the failure pressure based on the fracture toughness criterion
```

```
n = -0.00546+0.556*(data_Sy./data_Su)-0.547*(data_Sy./data_Su).^2; % Calculate strain hardening exponent

F3 = (3.85*(1./n).^0.5.*(1-n)+pi*n).*(1+n); % Calculate F3 Factor

k = (0.005-data_Sy./data_E)./data_Sy.^(1./n); % Calculate K Coefficient

Jc = round(12*data_CVN./0.124); % Calculate critical value of J

% Calculate effective flaw area depending on rectangular or elliptical

z = 0.5.*(A./flaw_length>0.5)+A./flaw_length.*(A./flaw_length<=0.5);

% Calculate shape factor

Qf = 1.2581-0.20589*(z)-11.493*(z).^2+29.586*(z).^3-23.584*(z).^4;

% Calculate free surface factor

Fsf = ((2*data_WT./(pi*A)).*tan(pi*A./(2*data_WT)).*(1-2*z)+2*z).*(A./data_WT<=0.95)+((8.515+(A./data_WT-0.95).*(162./data_WT)).*(1-2*z)+2*z).*(A./data_WT>0.95);

% Iteration to calculate signma_normal via Newton Raphson method

maxstep = 1000;

ini_step = ones(nS,1);

ini_sigma = data_Sy;

ini_Ji = Qf.*Fsf.*A.*(ini_sigma.^2.*pi./data_E+F3.*k.*ini_sigma.^(1./n).*ini_sigma)-Jc;

ini_dJi = Qf.*Fsf.*A.*(2*pi*ini_sigma./data_E+(1+1./n).*F3.*k.*ini_sigma.^(1./n));

ini_Qf = Qf;

ini_Fsf = Fsf;

ini_A = A;

ini_Jc = Jc;


for m = 1:nS

   step = ini_step(m);

   Ji = ini_Ji(m);
```

```
        dJi = ini_dJi(m);
        Qf = ini_Qf(m);
        Fsf = ini_Fsf(m);
        A = ini_A(m);
        sigma = ini_sigma(m);
        Jc = ini_Jc(m);
        while abs(Ji)>1e-3 && step<=maxstep
            dJi = Qf*Fsf*A*(2*pi*sigma/data_E(m)+(1+1/n(m))*F3(m)*k(m)*sigma^(1/n(m)));
            delta_sigma = -Ji/dJi;
            sigma =  sigma+delta_sigma;
            Ji = Qf*Fsf*A*(sigma^2*pi/data_E(m)+F3(m)*k(m)*sigma^(1/n(m))*sigma)-Jc;
            step = step+1;
        end
        final_sigma(m,1) = sigma;
    end

    % Compute normal stress and failure pressure
    sigmaN = final_sigma.*(1-A_Eff./A0)./(1-A_Eff./(A0.*M));
    Pressure_f2 =
(sigmaN.*data_WT./((pi/4)*A+0.5*data_D)).*(strcmp(flaw_location,'I')||strcmp(flaw_location,'
ND'))...
        +(2*sigmaN.*data_WT./data_D).*(strcmp(flaw_location,'E'));
    % The lower one will be the failure pressure
    Pressure_f = min(Pressure_f1,Pressure_f2);
    duration1 = etime(clock,time1); % time usage for computing Pf
    %% CMC to calculate POF
```

```
    for num2 = 1:length(SF)
        time2 = clock; % starting time of POF calculation
        safetyFactor = SF(num1.4);
        %% Determination on sample size
        if safetyFactor <1.4
            Loop = 100;
        elseif safetyFactor >=1.40 && safetyFactor <1.46
            Loop = 1000;
        elseif safetyFactor >=1.46
            Loop = 10000;
        end

        flawLength = Ratio_Ld*Ratio_dt*WT{1}(num1);
        flawDepth = Ratio_dt*WT{1}(num1);
        [Pressure_CorLAS, MOP] = CorLAS(safetyFactor, Sy{3}, Su{3}, E{3}, CVN{3},
flow_definition, D{1}(num1), WT{1}(num1),...
            flawLength, flawDepth, shape, flaw_location, Fd, Ft);
        beta = sqrt(6)*Rp{3}*Rp{4}/pi; % Scale parameter
        mu = -psi(1)*beta-Rp{3}; % Location parameter

        for loop = 1:Loop
            data_MOP = MOP*(-evrnd(mu,beta,nS,1)); % Rp is gumbel
            % Limit state function & Calculate POF
            LSF = Pressure_f.*normrnd(Rtp{3}, Rtp{3}*Rtp{4}, nS, 1)-data_MOP;%considering
model error
            ig = ones(nS,1);
```

```
            nF = sum(ig(LSF<=0));

            POF (loop) = nF/nS;


        end

        fprintf('Case %d\n',count)

        fprintf('POF=%d , SF=%1.2f, Time=%d seconds\n',mean(POF), safetyFactor)

        dataSet(count,:) = {count, Sy{1}, Sy{2}, Sy{3}, Sy{4}, Su{1}, Su{2}, Su{3}, Su{4},
E{3}, CVN{1},  CVN{2},  CVN{3},  CVN{4}, ...

            D{1}(num1), D{2}, D{3}(num1), D{4}, WT{1}(num1), WT{2}, WT{3}(num1),
WT{4},...

            MOP, Rp{2}, Rp{3}, Rp{4},...

            flow_definition, flaw_location, shape, Ratio_dt, Ratio_Ld, ...

            Pressure_CorLAS, mean (POF), safetyFactor};

        count = count+1;

        POF = [];


    end

  end
```

APPENDIX C: DETAILS OF THE BURST TEST DATA

No.	D (mm)	t (mm)	a (mm)	L (mm)	σ_{YS} (MPa)	σ_{UTS} (MPa)	A_c (mm^2)	CVN (J)	Shape	Material	Ref
1	762	9.8	5.99	219.2	420.595	563.322	53.33	40.67	R	X52	[8]
2	762	9.73	5.92	369.82	420.595	563.322	53.33	40.67	R	X52	
3	762	9.96	9.17	224.03	420.595	563.322	53.33	40.67	R	X52	
4	762	9.58	7.75	224.03	417.837	560.564	53.33	36.61	R	X52	
5	762	9.65	5.84	83.82	394.394	530.915	53.33	39.32	R	X52	
6	762	9.65	5.84	83.82	394.394	530.915	53.33	39.32	R	X52	
7	762	9.27	3.56	370.84	440.591	575.043	53.33	36.61	R	X52	
8	762	9.63	3.91	222.25	440.591	575.043	53.33	36.61	R	X52	
9	762	9.63	3.91	83.82	440.591	575.043	53.33	36.61	R	X52	
10	762	9.88	8.1	370.84	439.901	553.669	53.33	40.67	R	X52	
11	762	9.88	8.05	86.36	439.901	553.669	53.33	40.67	R	X52	
12	914.4	10.03	5.13	84.58	509.541	632.961	53.33	29.83	R	X60C	
13	914.4	10.12	5.13	153.16	504.025	633.651	53.33	28.47	R	X60C	
14	914.4	11.15	6.83	139.7	379.225	536.431	53.33	37.96	R	X60V	
15	914.4	11.3	8.66	139.7	379.225	536.431	53.33	37.96	R	X60V	
16	914.4	9.73	4.95	190.5	475.755	618.482	53.33	29.83	R	X60V	
17	762	9.14	4.67	152.4	448.175	583.317	53.33	27.12	R	X60C	
18	762	9.32	4.57	152.4	448.175	583.317	53.33	27.12	R	X60C	
19	762	9.47	4.52	152.4	448.175	583.317	53.33	27.12	R	X60C	
20	914.4	9.79	5.08	228.6	474.376	601.002	53.33	18.98	R	X65C	
21	914.4	9.98	7.62	213.36	449.554	609.518	53.33	31.18	R	X60V	
22	914.4	9.98	7.54	121.92	449.554	609.518	53.33	31.18	R	X60V	
23	762	15.49	10.89	406.4	456.449	627.445	53.33	42.03	R	X52	
24	762	15.65	10.87	406.4	456.449	627.445	53.33	42.03	R	X52	
25	863.6	12.8	3.22	406.4	465.413	613.655	53.33	17.63	R	X65	
26	863.6	12.93	11.22	609.6	465.413	613.655	53.33	17.63	R	X65	
27	863.6	12.93	10.69	609.6	465.413	613.655	53.33	17.63	R	X65	
28	914.4	10.57	4.32	165.1	456.449	609.518	53.33	33.9	R	X60V	
29	914.4	10.26	5.21	111.76	449.554	609.518	53.33	31.18	R	X60V	
30	1066.8	10.26	6.5	165.1	435.075	586.075	53.33	29.83	R	X60	
31	914.4	9.83	6.85	152.4	484.719	610.208	53.33	16.27	R	X65	
32	914.4	10.67	7.49	63.5	423.353	587.454	53.33	36.61	R	X60	
33	914.4	11.12	7.57	127	397.842	562.632	53.33	46.1	R	X60	
34	762	17.5	13.6	350	673	723	80	175	R	X80	[31]
35	762	17.5	14.4	350	673	723	80	175	R	X80	
36	914.4	16.4	9	150	739	813	80	253	R	X100	[32]
37	914.4	16.4	6	450	739	813	80	253	R	X100	
38	1422.4	19.25	10.4	180	740	774	80	261	R	X100	
39	1422.4	20.1	3.8	385	795	840	80	171	R	X100	
40	863.6	9.5	3.1	41	415.064	537.1	60	24.48	S	X52	[33]
41	863.6	9.5	3.1	32	362.66	500.56	60	35.36	S	X52	
42	508	6.5	2.7	57	341.29	486.77	40	23.12	S	X52	
43	508	6.52	3.8	30	349.56	497.112	40	23.12	S	X52	
44	508	6.37	4.2	58	357.83	521.93	40	21.76	S	X52	
45	914.4	9.58	5.1	71.5	480.56	613.63	60	109.8	S	X65	
46	508	6.9	2.2	99	362.66	525.38	40	28.47	S	X52	
47	564.8	18.4	16.8	218	798	922	80	78	S	34CrMO4	[34]
48	564	18	9.3	144	778	925	80	59	S	34CrMO4	
49	566	18	11.6	215	703	847	80	80	S	34CrMO4	
50	565.6	17.8	15.8	150	751	886	80	79	S	34CrMO4	
51	564.8	20.4	16.1	96	878	990	80	64	S	34CrMO4	
52	565.4	21.7	14.5	65	866	979	80	65	S	34CrMO4	
53	565.2	17.6	14.6	64.6	813	944	80	59	S	34CrMO4	
54	565	17.5	13	94	859	982	80	77	S	34CrMO4	
55	564.8	18.4	14.7	155	853	973	80	75	S	34CrMO4	

(*continued on next page*)

(*Continued*)

No.	D (mm)	t (mm)	a (mm)	L (mm)	σ_{YS} (MPa)	σ_{UTS} (MPa)	A_c (mm^2)	CVN (J)	Shape	Material	Ref
56	567	18.5	10.7	143	842	985	80	63	S	34CrMO4	
57	565.4	17.7	9	215	830	984	80	65	S	34CrMO4	
58	565.6	17.8	10	142	726	879	80	81	S	34CrMO4	
59	565.4	18.7	13.5	93	843	976	80	76	S	34CrMO4	
60	571.4	17.7	13.1	160	831	947	80	68	S	34CrMO4	
61	565.2	17.6	11.6	205	832	951	80	68	S	34CrMO4	
62	230	7.3	5.84	94.9	683	847	50	32	S	Ni-Cr-Mo	[35]
63	230	6.8	4.76	88.4	683	847	50	32	S	Ni-Cr-Mo	
64	230	7.2	4.32	93.6	683	847	50	32	S	Ni-Cr-Mo	
65	230	7.3	5.47	94.9	683	847	50	32	S	CrMO4	
66	230	6.9	4.9	89.7	890	949	50	66	S	CrMO4	
67	230	7.6	5.47	98.8	890	949	50	66	S	CrMO4	
68	230	7.6	5.7	98.8	890	949	50	66	S	CrMO4	
69	230	7.3	5.69	94.9	890	949	50	66	S	CrMO4	
70	230	7.7	6.08	100.1	890	949	50	66	S	CrMO4	
71	230	7.8	6.47	101.4	890	949	50	66	S	CrMO4	
72	236	9.2	7.36	92	648	786	50	32	S	CrMO4	
73	236	9.7	7.27	97	648	786	50	32	S	CrMO4	
74	236	9.9	7.92	99	648	786	50	32	S	CrMO4	
75	178	5.35	2.71	40.66	570	776	45	12.6	S	CrMO4	
76	178	5.48	3.22	40.55	577	774	45	14.4	S	CrMO4	
77	178	5.58	3.96	42.41	584	817	45	14.4	S	CrMO4	
78	178	5.08	4.01	37.59	625	783	45	14.4	S	CrMO4	
79	178	5.15	4.69	39.14	623	797	45	14.4	S	CrMO4	
80	178	5.1	2.61	44.37	587	762	45	13.05	S	CrMO4	
81	178	5.35	3.19	44.94	563	808	45	13.05	S	CrMO4	
82	178	5.51	3.88	47.39	577	800	45	13.05	S	CrMO4	
83	178	5.33	4.24	45.3	635	811	45	13.05	S	CrMO4	
84	178	5.2	4.66	44.2	604	825	45	13.05	S	CrMO4	
85	178	5.53	2.78	55.85	541	826	45	13.95	S	CrMO4	
86	178	5.43	3.14	52.67	536	736	45	13.95	S	CrMO4	
87	178	5.33	3.78	54.37	582	802	45	13.95	S	CrMO4	
88	178	5.33	4.16	52.23	560	811	45	13.95	S	CrMO4	
89	178	5.33	4.84	53.3	630	832	45	13.95	S	CrMO4	
90	178	5.25	2.58	65.1	670	815	45	13.95	S	CrMO4	
91	178	5.02	3.14	65.76	599	808	45	11.25	S	CrMO4	
92	178	4.93	3.43	61.13	595	796	45	11.25	S	CrMO4	
93	178	5.41	4.21	66	643	829	45	11.25	S	CrMO4	
94	178	5.36	4.85	67.53	557	838	45	11.25	S	CrMO4	
95	178	5.41	4.33	81.15	615	823	45	11.25	S	CrMO4	
96	178	4.95	3.04	76.23	619	831	45	11.25	S	CrMO4	
97	178	5.1	3.37	74.46	603	787	45	10.8	S	CrMO4	
98	178	5.2	408	76.44	665	843	45	10.8	S	CrMO4	
99	178	5.53	4.92	82.4	623	811	45	10.8	S	CrMO4	
100	232	6.58	5.48	65.14	748	875	40	16	S	CrMO4	
101	232	6.2	5.19	62	713	824	40	15.6	S	CrMO4	
102	232	6.4	5.5	65.92	763	872	40	25.6	S	CrMO4	

Note:

1. In the shape column, S denotes semi-elliptical crack profile and R denotes rectangular crack profile.
2. Young's modulus is assumed to be 210 GPa.

APPENDIX D: CALCULATION OF THE FAILURE STRESS IN CORLAS™ MODEL

- Flow-strength criterion:

The failure stress (σ_f) is calculated as:

$$\sigma_f = \sigma_{flow}\left(\frac{1-\frac{A_{eff}}{A_o}}{1-\frac{A_{eff}}{MA_o}}\right) \tag{B.1}$$

Where σ_{flow} is the flow strength, A_{eff} is the effective area, A_o is the reference area (the product of crack length and pipe wall thickness), and M is the Folias factor representing the stress increase due to the local bulging of a defected pipe subjected to internal pressure. σ_{flow} is calculated based on the yield strength (σ_{YS}) and the ultimate tensile strength (σ_{UTS}) using either of the following equations:

$$\sigma_{flow} = \sigma_{YS} + 68.75 \text{ MPa } (10000 \text{ psi}) \tag{B.2}$$

$$\sigma_{flow} = \sigma_{YS} + C(\sigma_{UTS} - \sigma_{YS}) \tag{B.3}$$

C is a constant parameter with a value between 0 and 1. Generally, C is taken as 0.5, meaning that σ_{flow} is equal to the average of σ_{YS} and σ_{UTS}. Eq. (B.3) is more frequently used as it applies to a wide range of pipeline steels [41].

Depends on the crack profile, A_{eff} is expressed as:

$$A_{eff} = \begin{cases} La, & Rectangular\ crack \\ \frac{\pi}{4}La, & semi-elliptical\ crack \end{cases} \tag{B.4}$$

M is computed differently for long cracks and short cracks as follows:

$$M = \begin{cases} \sqrt{1 + 0.6275\frac{L^2}{Dt} - 0.00375\left(\frac{L^2}{Dt}\right)^2}, \frac{L^2}{Dt} \leq 50 \\ 3.3 + 0.032\frac{L^2}{Dt}, \frac{L^2}{Dt} > 50 \end{cases} \tag{B.5}$$

- Fracture-toughness criterion:

The J-integral (J_t) can be computed by:

$$J_t = J_e + J_p = \frac{K_I^2}{E} + J_p \tag{B.6}$$

J_e and J_p are the elastic and plastic component of J_t, E is the Young's modulus, and K_I is the stress intensity factor.

(1) For surface crack:

$$K_I = \sqrt{Q_f F_{sf} a \sigma^2 \pi} \tag{B.7}$$

$$J_p = Q_f F_{sf} a f_3(n) \varepsilon_p \, \sigma_t \tag{B.8}$$

(2) For through-wall crack:

$$K_I = \sigma \sqrt{\pi c} \sqrt{\sec\left(\frac{L}{6D}\right)} \tag{B.9}$$

$$J_p = L f_3(n) \varepsilon_p \, \sigma_t \sqrt{\frac{6\pi D}{6\pi D - L}} \tag{B.10}$$

where Q_f and F_{sf} are geometrical factors, a is the crack depth, L is the crack length, ϵ_p is the equivalent plastic strain, $f_3(n)$ is a function of the strain hardening exponent (n). Q_f is computed using the following expression:

$$Q_f = 1.2581 - 0.20589\left(\frac{a}{L}\right) - 11.493\left(\frac{a}{L}\right)^2 + 29.586\left(\frac{a}{L}\right)^3 - 23.584\left(\frac{a}{L}\right)^4 \tag{B.11}$$

The values of F_{sf} is calculated using the following relation:

$$F_{sf} = \begin{cases} 1.0, \ \frac{a}{t} \leq 0.01 \\ \frac{2t}{\pi a}\tan\left(\frac{\pi a}{2t}\right)\left(1 - \frac{2a}{L}\right) + \frac{2a}{L}, 0.01 < \frac{a}{t} \leq 0.95 \\ \left[8.515 + \left(\frac{a}{t} - 0.95\right)\frac{162}{t}\right]\left(1 - \frac{2a}{L}\right) + \frac{2a}{L}, \frac{a}{t} > 0.95 \end{cases} \tag{B.12}$$

ε_p is computed using a power-law stress-strain relationship:

$$\varepsilon_p = K\sigma^n \tag{B.13}$$

K is the strength coefficient and is calculated based on n:

$$K = \frac{\sigma_{YS}}{(0.005-\frac{\sigma_{YS}}{E})^n} \tag{B.14}$$

$$n = -0.00546 + 0.556\frac{\sigma_{YS}}{\sigma_{UTS}} - 0.547(\frac{\sigma_{YS}}{\sigma_{UTS}})^2 \tag{B.15}$$

The strain-hardening factor $f_3(n)$ can be expressed as follows:

$$f_3(n) = \left[3.85\sqrt{\frac{1}{n}}(1-n) + \pi n\right](1+n) \tag{B.16}$$

APPENDIX E: DETAILS OF 25 BURST TEST DATA

No.	D (mm)	t (mm)	a (mm)	L (mm)	σ_{YS} (MPa)	σ_{UTS} (MPa)	CVN (J)	Shape	Reference
1	762	9.8	5.99	219.2	420.595	563.322	40.67	R	[1]
2	762	9.58	7.75	224.03	417.837	560.564	36.61	R	
3	762	9.27	3.56	370.84	440.591	575.043	36.61	R	
4	914.4	11.3	8.66	139.7	379.225	536.431	37.96	R	
5	762	9.14	4.67	152.4	448.175	583.317	27.12	R	
6	762	9.32	4.57	152.4	448.175	583.317	27.12	R	
7	762	9.47	4.52	152.4	448.175	583.317	27.12	R	
8	762	15.49	10.89	406.4	456.449	627.445	42.03	R	
9	762	15.65	10.87	406.4	456.449	627.445	42.03	R	
10	914.4	10.57	4.32	165.1	456.449	609.518	33.9	R	
11	914.4	10.26	5.21	111.76	449.554	609.518	31.18	R	
12	508	5.7	2.7	200	433	618	81	S	[15]
13	508	5.7	2.7	200	433	618	76	S	
14	508	5.7	2.9	200	433	618	68	S	
15	914.4	19.4	12.6	560	779	843	249	R	[44]
16	914.4	19.2	14.6	560	775	847	251	R	
17	914.4	19.2	15.2	560	775	840	247	R	
18	914.4	19.2	15.4	560	775	840	247	R	
19	914.4	19.3	13.3	280	771	834	249	R	
20	914.4	19.2	14.2	280	770	841	249	R	
21	914.4	19.3	15.3	280	779	846	249	R	
22	1422.5	19.25	10.4	180	740	774	261	R	[45]
23	914.4	16.4	9	150	739	813	253	R	
24	762	17.5	13.6	350	673	723	175	R	[38]
25	762	9.525	5.238	139.7	363.69	484.35	70.36	S	[46]

Note:

1. In the shape column, S denotes semi-elliptical crack profile and R denotes rectangular crack profile.
2. Young's modulus is assumed to be 210 GPa.